University of Alberta

The Influence of Dust Devils on Martian Water Vapour Transport

by

Kuan-Chih Chen

A thesis submitted to the Faculty of Graduate Studies and Research
in partial fulfillment of the requirements for the degree of

Master of Science
in
Thermo Fluids

Department of Mechanical Engineering

Spring 2011
Edmonton, Alberta

To my mother and brother

Abstract

A laboratory vortex generator was designed and fabricated to reproduce the behavior of this complex swirling flow. The vortex generator design was based on the results of computational fluid dynamics to optimize the performance, to reduce the cost, and to ensure kinematic similarity with atmospheric vortices. Stereo particle image velocimetry was used to investigate the flow velocity field generated by the instrument. In addition, laboratory scaled water vapour transport experiments were conducted, using a series of 128 solid-state humidity/temperature sensors. The results were used for successful validation of the numerical simulations. The study confirmed the expected effect that dust devils did indeed enhance mass transport. It was concluded that the radial Reynolds number was the most relevant scaling factor for this phenomenon. A numerical model with Martian conditions was then calculated to estimate the local water vapour transport rate from the Martian regolith with the presence of dust devil-like flows.

Acknowledgements

I would like to offer my utmost gratitude towards my supervisor Dr. Carlos F. Lange. His valuable suggestions, encouragement, and kindness helped me to complete this study.

I would like to extend my sincerest thank to my colleagues from the Department of Mechanical Engineering at the University of Alberta, who have helped make this project possible. Also I would like to thank Dr. John D. Wilson, Dr. Morris Flynn, and Mr. Mark Ackerman for their valuable suggestions and corrections to my thesis.

The financial support from the Canadian Space Agency is gratefully acknowledged.

Contents

List of Tables

List of Figures

List of Symbols

a = Refinement rate
a_{core} = Aspect ratio of vortex core
a_o = Aspect ratio of far field
A = Surface area, m^2
C = Non-dimensional constant
C_p = Thermal heat capacity, J m^{-3} K^{-1}
d_p = Effective pore size
D_{eff} = The effective mass transfer diffusion coefficient, m^2 s^{-2}
D_K = Knudsen diffusion coefficient, m^2 s^{-2}
D_{wc} = The binary diffusive coefficient of water vapour, m^2 s^{-2}
D' = A binary species transition diffusion coefficient, m^2 s^{-2}
f = Intensity value
f_l = Lens focal length, m
$F_{\Delta x}$ = Approximation of Taylor series
g = Intensity value
h = Depth of the inflow, m
h_{core} = Depth of inflow at r_{core} region, m
h_i = Height of the internal domain, m
L = Length scale
L_c = Characteristic length
J_{conv} = Advection flux, kg s^{-1}
J_{diff} = Diffusive flux, kg s^{-1}
J_{tot} = Total flux, kg s^{-1}
k = Thermal conductivity, W m^2 K^{-1}
K = Intrinsic permeability
m_{pm} = Mass of material
M_0 = Nominal magnification factor
$\mathbf{n}$ = Vector normal to the surface
n_{air} = Refractive index of air
n_{window} = Refractive index of polycarbonate
p = Pressure of the fluid, Pa
Q = Volume flow rate per unit length, m^2 s^{-1}
Q^* = Inflow volume flow rate, m^3 s^{-1}
$Q^*_{updraft}$ = Updraft volume flow rate, m^3 s^{-1}
r = Radial distance, m

r_{core} = Core radius, m
r_i = Radius of the internal domain
r_o = Radius of updraft, m
Re_{core} = Core Reynolds number in the radial direction
Re_r = Radial Reynolds number
Re_v = Vortex Reynolds number
s = Displacement, m
S_{gallus} = Gallus swirl ratio
S_{core} = Core swirl ratio
S_i = Additional momentum sources in the i direction
S_I = Internal swirl ratio
S_o = Swirl ratio of far field
S_ϕ = Source term
t = Time, s
u_i = Velocity component in the index notation, m s^{-1}
$\overrightarrow{u'}$ = Time-varying fluctuating velocity vector, m s^{-1}
U_r = Radial velocity in a cylindrical coordinate system, m s^{-1}
$U_{r_{core}}$ = Average radial velocity at r_{core} region, m s^{-1}
$U_{t_{core}}$ = Average maximum tangential velocity, m s^{-1}
U_z = Vertical velocity in a cylindrical coordinate system, m s^{-1}
$U_{z_{core}}$ = Average vertical velocity, m s^{-1}
U_θ = Tangential velocity in a cylindrical coordinate system, m s^{-1}
$\overrightarrow{U}$ = Velocity field (vector) of the fluid, m s^{-1}
V = Volume, m^3
V_{air} = Volume of air, m^3
V_{pm} = Volume of material, m^3
V_{total} = Total volume of porous medium, m^3

Greek
α = Angle within the YZ plane
β = Angle within the YZ plane
δ = Total offset distance
ϵ_h^d = Truncation error of Taylor series
Γ = Circulation, m^2 s^{-1}
Γ_ϕ = Diffusivity coefficient
μ = Dynamic viscosity, Pa s
ν = Kinematic viscosity of air, m^2 s^{-1}
Ω = Angular velocity
ϕ = Angle of image plane
ϕ_c = Intensive transport quantity
ϕ_{fg} = Discrete cross-correlation function
ρ = Total density of the fluid, kg m^{-3}
ρ_{CO_2} = CO_2 density, kg m^{-3}
ρ_{pm} = Density of material
ρ_w = Water vapour density, kg m^{-3}

φ = Porosity
τ = Tortuosity
θ = Angle of object plane

System of coordinates
x, y, z = Cartesian coordinate system
X, Y, Z = Cartesian coordinate system
r, θ, z = Cylindrical coordinate system
i, j, k = Index notation
u, v, w = Velocity component in Cartesian coordinate system

Over-bar
- = average conditions; time mean

Over-arrow
$\rightarrow$ = vector

Operator
$\bigtriangledown$ = Nabla
$\bigtriangleup$ = Delta, difference
log = Logarithm to the base of 10

Chapter 1

Introduction

This thesis work focuses on two main goals: 1) the modification of an existing Open-type vortex generator and 2) the investigation of water vapour transport through porous media with application to the dust devil's effects on Martian water vapour transport.

The recent Mars exploration mission, Phoenix Mars Lander, was successfully completed [Smith et al., 2008, Arvidson et al., 2008]. The objectives of the Phoenix mission were 1) to explore water ice, which helps to determine the possibility of life on Mars, 2) to study climate, 3) to obtain surface information of the north polar region, and 4) to prepare for human missions [Smith et al., 2008]. For example, the lander has confirmed the existing water ice below the Martian surface [Smith et al., 2009], collected pressure and temperature data from atmospheric measurement by the meteorological station (MET) [Zent et al., 2010, Taylor et al., 2010], and captured images of dust devils with the Surface Stereo Imager (SSI) [Ellehoj et al., 2010].

Observational evidence of existing H_2O [Smith et al., 2009] gave strong motivation to the search for life on Mars for the future missions. On Earth, water can be named as the mother of life, because it is required by all forms of life. When Phoenix found water ice on Mars, it brought the hope of possible life existing on this red planet. Furthermore, Mars could also be a potential habitable planet for humans in the future.

Martian atmospheric temperature measured from the Phoenix thermocouple, T1 (1 m above the lander deck), varied from -40°C to -95°C over a typical diurnal cycle [Taylor et al., 2010]. Both temperature fluctuations and its values were higher around noon than the evening [Taylor et al., 2010]. This might be caused by the increasing amount of thermal plumes around noon. Moreover, the daily average pressure of the Martian atmosphere was measured to be between 720 Pa and 860 Pa [Zent et al., 2010, Taylor et al., 2010]. This agreed with the seasonal variations of pressure drop from summer to fall.

A significant temperature increase due to the solar radiation would influence the amount of thermal plumes and would result in convective vortices and dust devils. It has been reported that 502 vortices with pressure drop larger than 0.3 Pa were observed during the Phoenix mission [Ellehoj et al., 2010]. High occurrence of convective vortices and dust devils on Mars were also reported by Thomas and Gierasch [1985] and Metzger et al. [1999]. A dust devil has high convective strength of vertical wind that is able to lift the loose dust. It may potentially enhance the rate of water vapour transport from the Martian regolith. However, the Phoenix data was limited during the 151 sol mission. To better understand the Martian water cycle, a numerical modelling technique based on mass transport with these atmospheric vortices is needed. It may improve and help study the effects of dust devil on water vapour transport from the Martian regolith. In addition, it is believed that these natural vortices may play an important role that affects and enhances the rate of mass transport.

The goal of this research is to study the relationship between dust devils and water vapour transport on Mars. By following Prieto's work [Prieto, 2006], the existing Open-type vortex generator had to be modified to produce better controllable dust devil-like flows. For this modification, the work started with investigating the non-dimensional characteristic parameters and the structures of dust devils. An extended sensitivity study was performed (based on Altimas [2007] results) in order to modify the existing vortex generator. A numerical model of the new vortex generator was used to optimize the apparatus dimensions, such as outflow radius and inflow height,

etc. When a laboratory scale vortex generator was constructed, the flow velocity field was measured by stereo particle image velocimetry (SPIV) technique. SPIV measurements provided the two dimensional flow information of three velocity components. A computational model of vortex generator with the porous media domain was used to validate the experimental flow field. The same numerical model was also used to simulate mass transport of water vapour from porous media in the laboratory conditions. Porous media were often used to study the water vapour transport mechanism under Earth or Martian conditions [Gu et al., 1998, Travis et al., 2003, Prieto, 2006, Farahaninia, 2008]. These studies demonstrated that the foam could be a suitable material to represent the regolith for both the experimental and numerical models. Finally, a numerical simulation with Martian conditions was calculated to estimate the water vapour transport mechanism between dust devils and the regolith on Mars. The results may help estimate the amount of water evaporation rate enhanced by dust devils from the regolith.

Chapter 2

Literature Review

2.1 Mars

The universe is relatively huge comparing to the solar system. Life from the another world is always a question. Scientists believe that water may be one of the essential resources for life because it is so on Earth. However, no human spacecraft can travel through the whole universe in a reasonable time using current technology. Because of this, Mars, which is the closest planet from Earth in the solar system, has been one of the popular planets to investigate. Many successful missions, such as the Viking I and II, Spirit, Opportunity, and Phoenix, provided humanity with much useful knowledge on Mars exploration.

From previous successful missions, the details about water/hydrogen abundance at the surface or at the near-surface atmosphere on Mars were obtained from the measurements using High Energy Neutron Detector (HEND), Thermal Emission Spectrometer (TES), Mars Orbiter Laser Altimeter (MOLA), and Gamma Ray Spectrometer (GRS), among others. [Mellon and Jakosky, 2000, Fisher et al., 2002, Fouchet et al., 2007, Haberle et al., 2007]. The first observation of existence of water was presented by Kieffer et al. [1976]. Further, the Martian north pole has been reported to have up to 70% mass concentration of water [Mitrofanov et al., 2002, Boynton

et al., 2002, Mitrofanov et al., 2003]. This information was among the reasons for the Phoenix Mars Lander, which was the most recent Martian mission, to land at the high latitudes close to the north pole.

The Phoenix lander landed on 25 May, 2008, at 68.22^o north latitude and 234.25^o east longitude [Smith et al., 2009]. During the mission, the Phoenix Lander verified the existence of water ice underneath a layer of dry regolith at the landing site on Mars [Smith et al., 2009]. In addition, the SSI instrument captured several occurrences of dust devils during the mission [Ellehoj et al., 2010]. The main goal of the mission was achieved by the confirmation of water ice. The existence of water ice may play a very important role for the potential life on Mars. Additional physical measurement data about the Martian polar region, such as temperature, pressure, wind speed, and wind direction, were also collected by the MET and SSI instruments.

In this project, a dust devil will be studied with respect to its effect on the water vapour transport mechanism. Shapiro [1969] and Doswell [1991] have summarized the atmospheric vortices. In general, at the axis of a dust devil pressure is lower and temperature higher than in the environment at the same level. Prieto [2006] initiated the study of the effect of dust devils on the water vapour transport from the porous regolith using three-dimensional numerical modeling. One-dimensional water vapour transport phenomenon on Mars has been studied by Mellon and Jakosky [1993] and Savijarvi [1995]. An idea of numerical simulation of water cycle was proposed by Jakosky et al. [1997]. To study the water vapour transport the following processes should be considered [de Groot and Mazur, 1984, Do, 1998] : advective flux, molecular diffusive flux, Knudsen diffusive flux, thermal diffusive flux, and surface diffusive flux. In practice, porous medium can be used to represent the Martian regolith [Kieffer et al., 1976, Sullivan et al., 2005], as the dusty basaltic material is the main component of the regolith. Because of dusty basaltic material, the pore structure can be defined as anisotropic. When the flow goes through anisotropic material, it results in irregular physical flow quantities such as pressure, velocity, etc. However, in simulations the regolith is assumed as an isotropic porous medium, because of lack of more detailed

information. Previous analytical studies of the mass transport of water in a porous medium on Earth [Gu et al., 1998] and Martian [Travis et al., 2003] conditions were based on the thermal diffusion and Knudsen diffusion. Both studies provided good model formulations in both Earth and Martian regolith. Other studies of dust devils on Mars [Thomas and Gierasch, 1985, Metzger et al., 1999, Ellehoj et al., 2010] also indicated the water vapour transport could be affected by this atmospheric convective vortices. The only previous attempt to quantify this effect was developed previously at the University of Alberta [Prieto, 2006], but the vortex model used was found to be not kinematically similar to a real atmospheric vortex. More details about dust devils will be introduced in Section 2.4.

2.2 Mass Transport

It is believed that dust devils may play an important role on enhancing the Martian water vapour transport rate [Thomas and Gierasch, 1985, Metzger et al., 1999, Prieto, 2006, Ellehoj et al., 2010]. Experimental and numerical models were used to prove their relationship. To study how the fluid flow moves through the porous media, we consider the five main mass transport mechanisms [de Groot and Mazur, 1984, Do, 1998]:

- Advective Flux

  Darcy's law [Darcy, 1856] has indicated that the flow velocity field obeys a linear relationship with the pressure gradients, when transported through a porous medium. In general, it is applied to water transport in soils. Buckingham [1907] has expanded Darcy's law to the unsaturated flow applications since most soils are unsaturated. Other researchers, such as Hubbert [1956] and Joseph et al. [1982], indicated that Darcy's law may not be applied to the high velocity flow regimes or should include the inertial terms, respectively. Bird et al. [2001] explained and detailed the hydraulic conductivity break-down between the proper-

ties of the fluids and the properties of the porous medium. From the diffusivity processes [Alzaydi and Moore, 1978, Thorstenson and Pollock, 1989, Massmann and Farrier, 1992, Massmann, 1998], the term of advective fluxes may be greater than other mass transport mechanisms with relatively small pressure gradients, when Darcy's law is applied.

- Molecular Diffusive Flux

  Fick's law [Fick, 1855] has similar characteristics as Darcy's law. It proposes a linear relationship between the diffusive flux and the concentration gradient in the fluid mixture cases. In general transport applications, the molecular diffusive flux from one fluid to another may be described using Fick's law [Jaynes and Rogowski, 1983, Bird et al., 2001]. Do [1998] has demonstrated Fick's law is also applicable to the study of porous medium. However, a diffusive coefficient of the material may be taken into account as a extra term.

- Knudsen Diffusive Flux

  Knudsen diffusive flux [Knudsen, 1909] is similar to Fick's law. The difference between these two diffusions is that the Knudsen's coefficient is related to temperature and pressure and Fick's coefficient to pressure gradients and velocity. Knudsen diffusion has been considered as relevant factor for flow through the regolith on Mars [Clifford and Hillel, 1986] due to low permeability, which may increase the diffusivity rate, when the low atmospheric pressure is applied [Sleep, 1998]. Nevertheless, Knudsen diffusion may be neglected for both the experiments and numerical simulations under Earth conditions in which the atmospheric pressure and permeability are much higher than in Martian conditions.

- Thermal Diffusive Flux

  Thermal diffusion or Ludwig-Soret effect [Ludwig, 1856] can be used in either liquid or gas mixture [Mason et al., 1967] when the temperature gradient is presented. Thermal diffusive coefficient can be then added into Fick's law [de Groot

and Mazur, 1984]. However, the current study was considered to be an isothermal condition and the temperature gradient was neglected. It should be noted that the assumption made is based on the temperature variation to be less than 3^oC in the experiments. Hence, the mechanism of thermal diffusion was excluded from this study.

- Surface Diffusive Flux

  Another commonly independent transport mechanism, surface diffusion, is addressed in a manner similar to molecular diffusion [Do, 1998, Gilliland et al., 1974]. It shows that molecular movement would drive a local concentration gradient in the adsorbed surface. We ignored this mechanism in this study due to the surface diffusion being usually neglected in the soil-related applications [Thorstenson and Pollock, 1989].

2.3 The Martian Regolith

The properties of Martian regolith have been estimated using numerical, theoretical, and experimental studies. The majority of the compositional materials on the Martian regolith are dusty basaltic [Kieffer et al., 1976, Sullivan et al., 2005]. From this information, a porous medium can be used to represent the Martian regolith.

In the north polar region, where the Phoenix Mars Lander landed, the density was estimated to be 1.0 ± 0.5 g cm^{-3} [Malin, 1986]. However, the local densities vary with the locations. For example, it is estimated to be between 1.15 ± 0.15 g cm^{-3} and 1.6 ± 0.4 g cm^{-3} at the Viking I site [Moore and Jakosky, 1989] and 3 g cm^{-3} at the Opportunity site [Jerolmack et al., 2006]. Generally, mean density of Martian regolith was estimated to be 3.9335 ± 0.0004 g cm^{-3} [Lodders and B. Fegley, 1998].

Some properties of the Martian surface were measured by the thermal and electrical conductivity probe (TECP) of Phoenix. The average thermal conductivity (κ) was 0.085 W m^{-1} K^{-1} and average volumetric heat capacity (C_p) 1.05×10^6 J m^{-3} K^{-1}

[Zent et al., 2010]. Further, the exchange rate of H_2O sustained a partial pressure difference of 1.8 Pa between the regolith and atmosphere within most of daytime. Atmospheric relative humidities increased very significantly from day to night, because of cool down on the atmosphere and the regolith. The soil temperature range measured by the TECP was between -92^{o}C and -20^{o}C.

2.4 Atmospheric Vortices: Dust Devils

There are many types of atmospheric vortices that exist on Earth. For example, tornadoes, hurricanes, and dust devils to name a few. Tornadoes are generated over the land and are associated with strong winds and thunderstorms. It is known to be a powerful vortex flow, which can cause a lot of economic damage. A hurricane is much more complex than a single tornado, and involves spiral rings of thunderstorms. It develops over the warm ocean, which eventually dissipates as it moves over the land. A dust devil is defined as tornado-like vortices. It typically carries a load of loose dust with vertical convective vortices, which usually harmless and very small compared to tornadoes and hurricanes in strength. These three types of vortices are the weather phenomena of rotating columns of air in vertical direction. However, dust devils are the only type of atmospheric vortices that naturally occur on Mars.

In general, the Martian dusty atmosphere is composed by 95% of CO_2 [Johnson, 1965] and less 0.5% of water vapour [Leovy, 2001] in averages for the while Martian surface and over a full Martian year. The temperature measured at 2 m height at the Phoenix landing site was between -40^{o}C and -95^{o}C [Taylor et al., 2010]. The pressure range was between 720 Pa and 860 Pa [Zent et al., 2010, Taylor et al., 2010]. The values of pressure and temperature were close to those at the triple point of water, which are 611.73 Pa and 273.16 K, respectively. As a result, water is mostly in vapour condition during transport.

In the day time, the sun radiation causes the occurrence of convective thermal plumes

because of thermal buoyancy. When convective plumes are getting active, natural events such as turbulent winds and convective vortices may occur [Murphy and Nelli, 2002]. This explanation agrees with the Phoenix data , which shows that a peak of convective vortex activities, in addition to dust devils, happened around noon [Ellehoj et al., 2010]. Moreover, a total of 502 convective vortices. which were identified by a pressure drop larger than 0.3 Pa, were detected during the Phoenix mission. Although dust devils on Mars are typically associated with core pressure drops of 1 to 5Pa, the mission team considered smaller pressure drops, since most dust devils will not pass exactly over the lander. To ensure the pressure drop measurement was not caused by, e.g. small-scale turbulence, the conditions of sufficient amplitude (¿0.3Pa) and duration (10-20 s) were selected. This identification procedure would also exclude the pressure drops, which occurred by the thermal plumes and wind gusts, etc [Ellehoj et al., 2010].

2.4.1 Structure of Dust Devils

Dust devils are known as tornado-like vortex flows due to the similar structure. Physical mechanisms of tornado-like flows, such as its characteristics were reviewed by Davies-Jones and Kessler [1974], Davies-Jones [1976], Davies-Jones [1982], and Lewellen [1993]. Tornado-like flows can be characterized by Navier-Stokes equation [Rankine, 1858, Burgers, 1948, Rott, 1958]. Rankine [1858] and Burgers-Rott [Burgers, 1948, Rott, 1958] vortex models, shown in Figure 2.1, and tangential velocity profiles are most commonly used to describe this type of flow.

The velocity profiles of Rankine vortex in a cylindrical coordinate system (r, θ, z) are

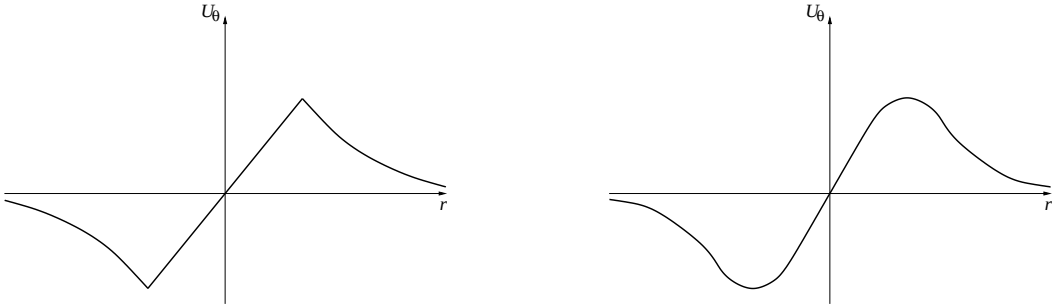

a) Rankine vortex b) Burgers-Rott vortex

Figure 2.1: Tangential velocity profiles of tornado-like vortex flows, U_θ.

defined as follows:

$$U_r = 0 \tag{2.1}$$

$$U_\theta = \begin{cases} U_{\theta_{max}} \dfrac{r}{r_{core}} & \text{if } 0 \leq r < r_{core} \\ U_{\theta_{max}} \dfrac{r_{core}}{r} & \text{if } r_{core} \leq r \end{cases} \tag{2.2}$$

$$U_z = 0 \tag{2.3}$$

where U_r is radial velocity, $U_{\theta_{max}}$ maximum tangential velocity, and U_z vertical velocity. It indicated that the tangential velocity is proportional to the radius within the vortex core. In other words, this relationship is named to be a solid body rotation for this ideal vortex core. In addition, the tangential velocity profile outside the vortex core is irrotational.

Burgers-Rott vortex has a better description on the tornado-like flow which was also obtained using an axisymmetric Navier-Stokes equation. The difference between these two vortex models is that the Burgers-Rott vortex includes the radial velocity which smoothes down the tangential velocity profile. The common point for both vortex cores is the axisymmetric assumption on the tangential velocity profile.

A fully developed tornado-like vortex flow can be divided into five regions [Snow, 1982, Lewellen, 1993], as illustrated in Figure 2.2.

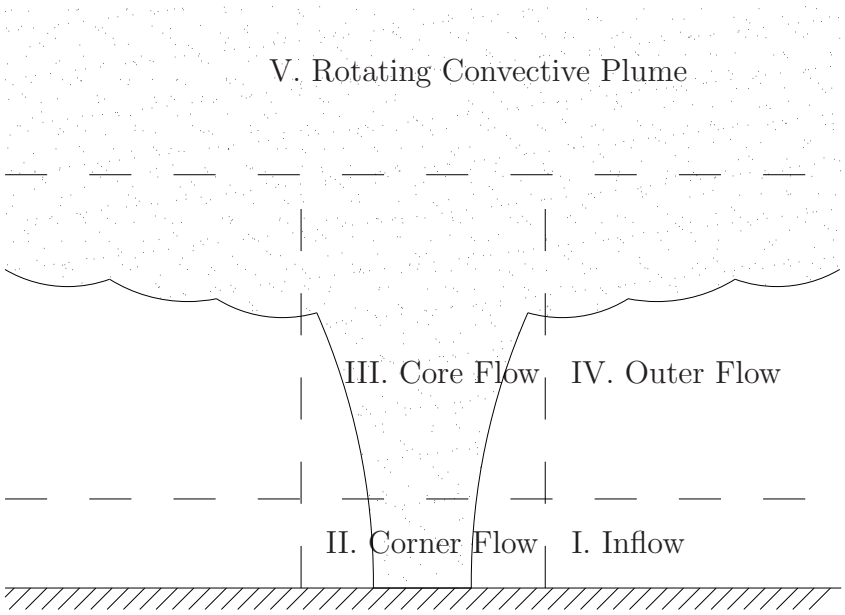

Figure 2.2: A Schematic of an atmospheric tornado-like vortex flow, according to Snow [1982].

- Region I: Surface boundary layer (Inflow)

  A radial inflow within surface boundary is induced by the circulation at the surface, which is perpendicular to the axis of rotation [Lewellen, 1993]. In addition, the radial velocity is relatively large compared to the axial velocity component [Rotunno, 1980, Morton, 1981, Wilson and Rottuno, 1982], because of the large radius of this region. The flow feeds into the corner region horizontally [Snow, 1982]. The rate of inflow is limited by the turbulent shear stress, i.e. transfer of momentum by the turbulence to the ground. When the flow is approaching the central axis in the vertical direction, the viscous effects would make the upper sub-layer thinner.

- Region II: Corner flow

  In this region, it is known that the horizontal vortex line can be induced to a vertical one [Lewellen, 1993]. It can also be named as turning region, due to the motion of tilting of the vortex lines. Vorticity and convergence are significant in

the corner flow region [Lewellen and Sheng, 1980], which result in the occurrence of maximum speed of wind [Wilson and Rottuno, 1982].

- Region III: Core flow

  A variety of different dynamics structure have been observed in this region [Snow, 1982]. The shape of condensation funnel depends not only on the vortex structure and intensity but also on the water vapor content of the air. The positive buoyant plumes or updraft induces the horizontal convergence in natural tornado-like vortices [Lewellen, 1993]. Further, the core radius is defined at the location where the maximum tangential velocity is.

- Region IV: Outer flow

  The concentrated vorticity in the region of the core flow and the positive buoyancy force in the region of the rotating convective plume affect the moving tendency of the flow in this region [Snow, 1982]. The flow spirals inward and upward. In other words, there are radial and vertical velocities that are present in this region. Hence, it is not irrotational flow. However, continuous inward advection of angular momentum is conservative. The tangential velocity profiles within this region and core region can be described using the definition of Rankine or/and Burgers-Rott vortex.

- Region V: The rotating convective plume

  This region must be sufficiently strong to maintain the updraft forces [Snow, 1982]. It is essential to include the top boundary conditions when determining the strength of this region [Lewellen, 1993].

The present study is aimed at the mass transport through the regolith. It is believed that the corner flow and inflow regions will play the relevant roles and have more influence than the other regions on the mass water vapour transport, since they are in contact with the regolith directly. Therefore, the analysis and characterization of dust devils for the present study are focused on these two regions. Three characteristic

parameters, such as swirl ratio, aspect ratio, and Reynolds number [Lewellen, 1962, Davies-Jones, 1976, Church and Snow, 1993, Lewellen, 1993], are the most important scaling factors for the tornado-like vortex flow. The details of these studies will be described in Section 3.3.

2.4.2 Death of Dust Devils

A sudden enlargement of natural dust devils is observed in the vortex funnels at this dispassion stage [Ward, 1972]. Vortex breakdown occurs when the flow transits from laminar to turbulence. The Reynolds number increases significantly and the vertical velocity of the wind, outside the core, increases, but inside the core, the upward speed decreases. Cold air and negative buoyant forces are the main reason for causing the vortex breakdown [Lee and Wilhelmson, 1997]. A downdraft of air near the rear flank of the dust devils increases, which cuts off the inflow, resulting in decrease of the vertical vorticity. When the vorticity of a dust devil descends and decreases, the vortex lines dissipate into the environment within a low strength, but do not end in the atmosphere. The vortex lines or vortices will remain in the atmosphere with a very low vortex strength. Occasionally, these vortex lines may merge with another vortex line or wind and create another dust devil.

2.5 Relevant Dimensionless Parameters of Dust Devils

Different strength of dust devils may result in different amount of water vapour transport. For example, the stronger and bigger dust devils may enhance water vapour transport from the regolith more than weaker dust devils. As a result, it is essential to characterize the dust devils with non-dimensional parameters. The non-dimensional parameters also allow for comparison between dust devils on Earth and on Mars. Finally, if a proper scaling function based on non-dimensional parameters can be found,

enhancement results from a few cases can be used to estimate water vapour transport for all cases. In the previous section, it was shown that a dust devil is a tornado-like flow. In other words, a dust devil can be defined using the scaling factors which are applied to tornadoes.

Lewellen [1962] simplified the Navier-Stokes equations for a three-dimensional steady state, viscous, incompressible, axisymmetric vortex flow in closed cylinder. This type of vortex flow could be governed by three non-dimensional parameters; the ratio of volume flow per unit axial length (the depth of the inflow) to circulation (at the far field), Q/Γ; the radial Reynolds number,

$$Re_r = \frac{Q}{\nu} \ ; \tag{2.4}$$

and the ratio of characteristic lengths,

$$L_c = \frac{r_o}{h} \ ; \tag{2.5}$$

where r_o is the radius of updraft, h the depth of the inflow, ν the kinematic viscosity of air, Q the volume flow rate per unit axial length, and Γ the circulation. It should be noted that the depth of the inflow of vortex flows in nature means the last streamline before the circulation. Some limitations, such as boundary conditions, might be applied on these three non-dimensional parameters. Later Davies-Jones [1973] applied the Buckingham π-theorem, based on the Ward type of a three-dimensional vortex simulator [Ward, 1972]. He redefined two of these three non-dimensional parameters as the aspect ratio

$$a_o = \frac{h}{r_o} \tag{2.6}$$

and the swirl ratio

$$S_o = \frac{r_o \Gamma}{2Q^*} \ . \tag{2.7}$$

where Q^* is the inflow volume flow rate. Note that Q^* has the usual units of $\mathrm{m}^3\ \mathrm{s}^{-1}$, while the above-defined Q has the units of $\mathrm{m}^2\ \mathrm{s}^{-1}$. From the experimental results, Ward's model not only had better agreement with natural vortices than other models

at that time, but also performed the characteristics of natural vortices [Davies-Jones, 1973, 1976]. Rotunno [1977] later rewrote the swirl ratio as

$$S_o = \frac{r_o U_\theta}{2hU_r} \tag{2.8}$$

where U_θ is the average azimuthal velocity at r_o,

$$U_\theta = \frac{1}{2\pi}\int_0^{2\pi} U_{(\theta,local)} d\theta \tag{2.9}$$

and U_r is the average radial velocity at the inflow area at r_o,

$$U_r = \frac{1}{2\pi h}\int_0^{h}\int_0^{2\pi} U_{(r,local)} d\theta dz \ . \tag{2.10}$$

This swirl ratio was defined under two parameters, the configuration ratio and the inflow angle, which related to the core size. When the updraft radius was two times the inflow depth, the swirl ratio then depended on the inflow angle.

In general, these dimensionless parameters were suitable for the Ward type of vortex simulator, as shown in Figure 2.5. But, they were not well defined for the Open-type of vortex generator, as shown in Figure 2.6. There was no precise definition of the characteristics of r_o and h for the open model and natural vortex flows in the literature. Some researchers, e.g. Wilson and Rottuno [1982] and Prieto [2006], suggested that the location of r_o is at the radial location of the maximum radial velocity, based on their numerical and laboratory studies of laminar vortex flows.

Basically, the swirl ratio was defined as the ratio of angular momentum to axial momentum from the above information. However, there were arguments on this definition of swirl ratio. For example, Church et al. [1979] found that the internal vortex structure exhibits less correlation on the aspect ratio and on the radial/convective Reynolds number. Because of this, Nolan and Farrell [1999] and Nolan [2005] argued on the definition of the swirl ratio. They defined an internal swirl ratio as,

$$S_I = \frac{r_i}{2h_i}\frac{\int_0^{h_i} 2\pi r_i U_r(r_i, z) dz}{\int_0^{r_i} U_z(r, h_i) 2\pi r dr} \ . \tag{2.11}$$

where r_i is the radius of the internal domain, h_i the height of the internal domain, and $U_r(r_i, h_i)$ the radial velocity at the radius of r_i. From the Equation (2.11), the internal swirl ratio was defined as the ratio of the inflow azimuthal velocity to the maximum possible updraft speed. Both maximum azimuthal and maximum radial velocities are easy to locate in the natural vortex flows, as Barcilon [1967] found. Thus, these were correlated into a vortex Reynolds number, the ratio of inflow circulation to the viscosity, which can be written as

$$Re_v = \frac{\Omega h_i}{\nu} \tag{2.12}$$

where Ω is the angular velocity. It should be noted that the internal swirl ratio was varied with the size of the domain choice and not designed for either Ward or Open type simulators. Further, Nolan [2005] developed this dimensionless parameter to predict both the shape and the strength of the vortex flow. As a result, this was not the best swirl ratio to study water transport mechanism.

From the above description, dust devils can be characterized by the swirl ratio, the internal swirl ratio, vortex Reynolds number, and aspect ratio. However, they may not suitable for analyzing all natural, numerical, and laboratory vortex flows. Other studies such as Lewellen and Lewellen [2000], Haan et al. [2008], and Kuai et al. [2008] suggested using a more precise location of the core radius, r_{core}, the location of maximum tangential velocity, to characterize the vortex structure. The previous three non-dimensional parameters were rewritten as:

$$Re_{core} = \frac{2\pi r_{core} U_{\theta_{max}}}{\nu} \tag{2.13}$$

$$a = \frac{h}{r_{core}} \tag{2.14}$$

$$S_{gallus} = \frac{\pi r_{core}^2 U_{\theta_{max}}}{Q^*_{updraft}} \ . \tag{2.15}$$

where $U_{\theta_{max}}$ is the maximum average tangential velocity at r_{core} and $Q^*_{updraft}$ the updraft volume flow rate through the system, which is the volume flow rate through the fan in the experiments and numerical models. For the vortex flows in nature, it

was assumed to be equivalent to previous definition and can be expressed as

$$Q^*_{updraft} = Qh = Q^* \tag{2.16}$$

The swirl ratio of vortex core here is always smaller than previous researchers' equations by a ratio of r_{core}/r_o [Kuai et al., 2008]. These definitions are illustrated in Figure 2.3 and Figure 2.4.

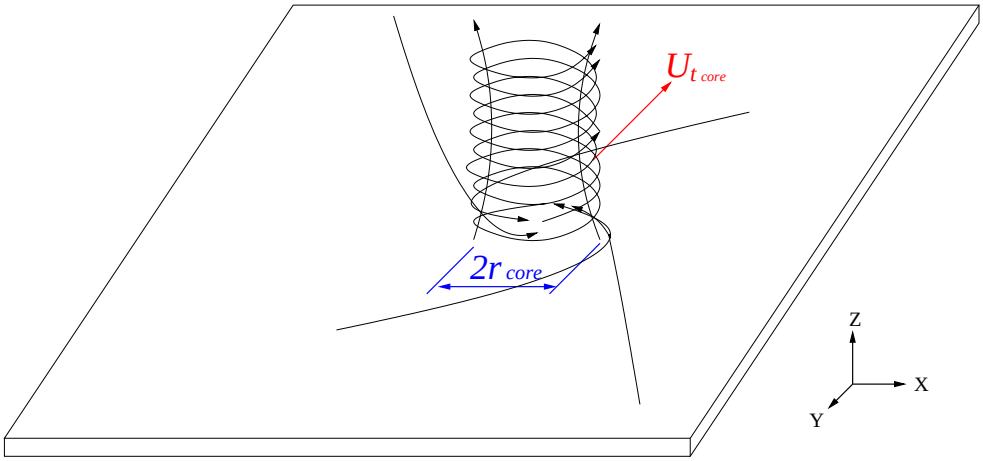

Figure 2.3: A three-dimensional schematic of vortex flow.

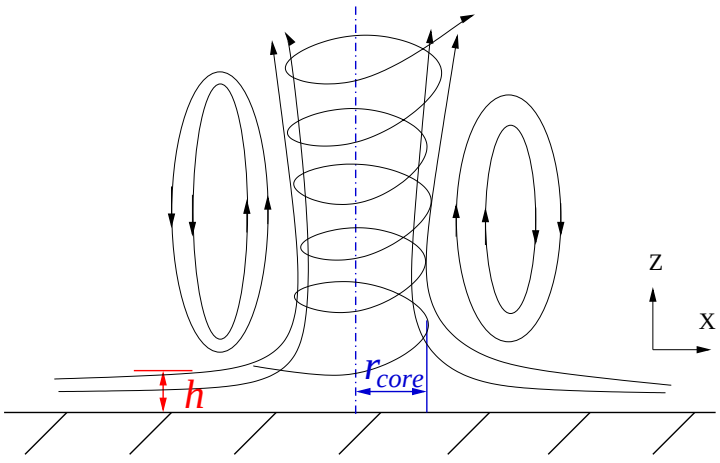

Figure 2.4: A two-dimensional schematic of vortex flow.

2.6 Study of Vortex Generators

Natural events of dust devil are unpredictable and difficult to measure on both Earth and Mars. On Earth, the researchers have studied dust devils in the sub-arctic regions [Grant, 1949] and hot desert areas [Sinclair, 1969, Hess and Spillane, 1990]. On Mars, the images of dust devils have been taken by Viking Orbiter [Thomas and Gierasch, 1985], Pathfinder [Edgett and Malin, 2000, Balme et al., 2003, Metzger et al., 1999], Spirit lander, and Phoenix Mars Lander [Ellehoj et al., 2010]. However, the measured data from Mars missions are limited. Hence, laboratory vortex generating apparatus was considered to allow for a better physical study of dust devils. An ideal apparatus was also designed to generate a simple, controllable, and reproducible vortex flow in this study.

A Ward-type generator could produce similar characteristics of natural vortex flows, such as kinematics (swirl ratio) and geometry (aspect ratio) [Davies-Jones, 1976, Church and Snow, 1993], in laboratory conditions. It was developed by Ward [1972], shown in Figure 2.5. Air flow enters the convergence region through the rotating screens which redirect the flow. It then goes through the updraft hole and enters the convection region. At this stage, the internal vortex structure of this swirling flow is created. A fine mesh honeycomb baffle will reduce the vorticity and flow rotation at the fan. Finally, the non-rotating flow exits from the exhaust zone, same as the natural vortex flow in the atmosphere [Davies-Jones, 1976]. It should be noted that the convergence region, the flow through the updraft hole, and the convection region are regarded as inflow, corner flow, and core flow in vortex structure, respectively.

The use of Ward-type model is not appropriate for present study, although the Ward-type generator can produce the good characteristics of vortex flows. The reason is that we would like to measure the vortex flow around a miniatured lander, which located at a fixed position. However, the vortex flow is not allowed to move along the surface in the inflow region in Ward-type model. Prieto [2006] has studied mass transport through the regolith using an "Open" type tornado generator, developed

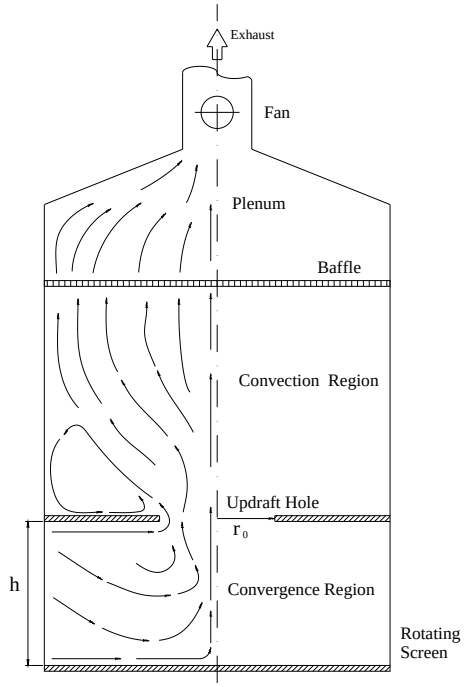

Figure 2.5: A schematic of the Ward-type vortex generator.

by Hsu [1973] (Figure 2.6). It consists of a fixed cylinder and an electrical motor with a vertical fan blade. The shape of bell curve is designed at the lower-end of the cylinder. It alleviates the boundary effects and turbulence generation. When the fan blades are vertically oriented, the upward angular momentum is induced to simulate the dust devils. It should be noted that the updraft axial momentum is very small. However, this "Open" type vortex generator produces relatively weak vorticities and widening vortex corner flow region [Prieto, 2006]. In other words, it did not create the desired kinematic characteristics similar to atmospheric vortices. The reason maybe that the vortex flow in this case is driven purely by viscous forces.

Altimas [2007] has studied an idealized vortex generator based on the relevant geometric parameters illustrated in Figure 2.7. The simulations were performed using computational fluid dynamics with a commercial software package, ANSYS/CFX. The idea of his design was based on a Gallus type vortex generator [Gallus et al., 2006], developed at Iowa State University. Figure 2.8 is the schematic of the Gallus model. The difference between these two models of design are the locations of the

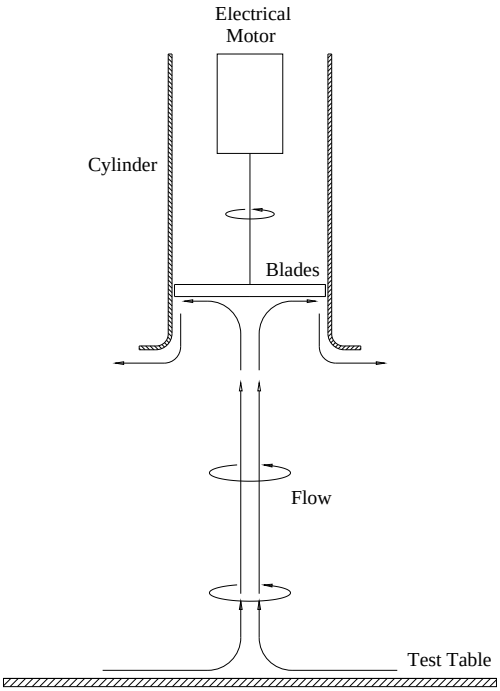

Figure 2.6: A schematic of the "Open" model vortex generator.

vanes and bell mouth shape outflow section. Both models are able to achieve/produce the two essential conditions of the natural atmospheric vortices. One is the presence of an initial vorticity and the other one is updraft flow [Howells et al., 1988]. They are similar to Ward-type design. However, the internal structure of vortex flow is not fixed by the structure of the vortex generator and this design allows for the arbitrary placement of a miniature lander on the surface.

In the Gallus type of vortex generator, an axial fan creates the axial momentum. The turning vanes which are placed evenly around the circumference on the top of the duct are redirecting the flow and generating the vorticity at the same time. The strength of vortices will depend on the angle of the vanes. The flow travels through the vertical duct and enters the inflow section with the desired tangential velocity. The vortex flow is then produced at the experimental region. However, the real dimensions of this apparatus are too large. When it is introduced in geometric scale to fit the existing open-type vortex generator at the University of Alberta, the numerical simulations suggest that the strength of vortices is too low.

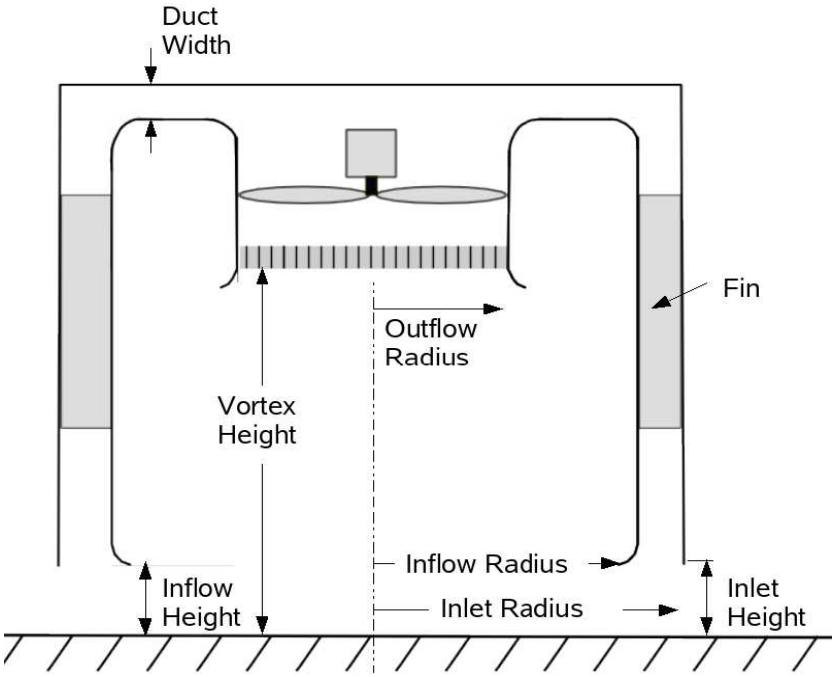

Figure 2.7: A schematic of idealized vortex generator of Altimas [2007] study.

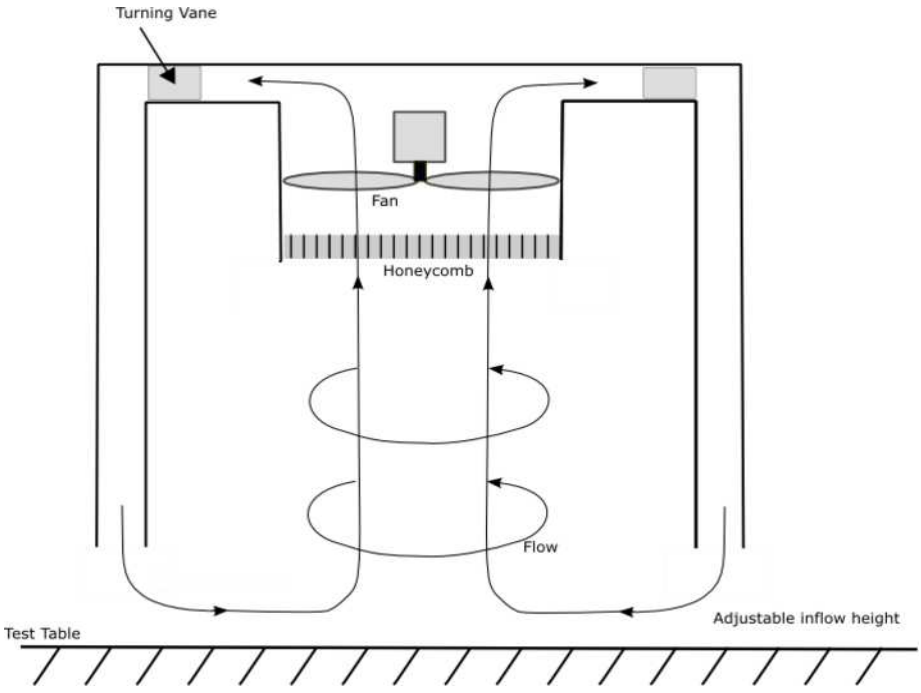

Figure 2.8: A schematic of vortex generator developed by Gallus et al. [2006]

An idealized model was the numerically designed to increase the vortices in the duct. Altimas [2007] has studied the dimensional analysis based on the both Gallus design and existing apparatus. The flow is sucked from the axial fan and traveled through from the horizontal to vertical duct. A couple of curved fins were evenly placed around the vertical duct circumferentially. The direction of flow tilts, when passing through the fins and the swirl is created. It then enters the experimental area. It should be noted that the flow that escapes from the cap is relatively small compared to the whole flow field. A total of nine length scale variables were studied to optimize the geometry of vortex generator design. From the results of sensitivity studies based on the kinematic similarity, the fin angle, outflow radius, and inlet height are the most relevant factors that impact the vortex structure.

2.7 Velocity measurement technique in SPIV

Observations of fluid flow are dated as far back as Leonardo Da Vinci [Raffel et al., 2007]. A step forward towards measurement of fluid flow began when Ludwig Prandtl developed a flow visualization experiment using a water tunnel. Scientists started to invent intrusive flow devices to measure fluid flow at a single point [Adrian, 1986]. The common devices are pitot tubes and hot-wire anemometers. These intrusive technique equipments are useful and economic, but they also cause significant effects to flow fields, such as blockage of the flow by physical probes. A non-intrusive technique, Laser Doppler Velocimetry (LDV), was then invented [Raffel et al., 2007] for measuring the direction and speed of fluid with seeding particles. However, the principle of LDV is a single-point method and not able to measure well unsteady flows. The study of turbulent flows has been one of the motivations for the development of multi-point measurement techniques. A useful planar measurement technique, particle image velocimetry (PIV), was developed in the last 20 years [Raffel et al., 2007]. PIV determines two velocity components of fluid field in a two dimensional plane. SPIV is a product of the evolution of PIV. The velocity components now can be represented in

three dimensions. It also improved from the analysis method of auto-correlation to cross-correlation [Raffel et al., 2007]. This approach tends to increase the accuracy slightly. By improving the optics, the laser, the electronics, the video and computer technique, the SPIV measurements can be employed to most flow visualization.

Chapter 3

Theory

The present work follows Prieto's study [Prieto, 2006] of local water vapour transport. The conclusion of his work was that a dust devil would enhance the local water vapour transport rate. However, the type of Open vortex generator used in his study did not produce the required characteristic parameters of dust devil-like flow. To achieve the study of mass transport phenomenon from the Martian regolith subjected to dust devils in the Martian atmosphere, the following sub-studies were performed:

- Understand the physical processes behind the water vapour transport and natural event of dust devils.
- Design an optimized vortex generator using CFD and build the new generator.
- Measure the velocity field and water vapour transport with the vortex generator.
- Validate the numerical model of vortex enhanced mass transfer with the experimental results.
- Apply the Martian conditions to the numerical models and test scaling parameter.

3.1 Type of Solution

There are three types of solution that can be used to obtain the results of flow field in engineering applications.

- Analytical solution

  It is the most accurate and robust solution. It is applicable for solving flow problems with simple geometries and physics, such as pipe flows, etc. When a fluid flow travels through complicated geometries or has multiple physical conditions, the exact solution then becomes very difficult to approach and calculate.

- Experimental solution

  It presents the realistic data from the true life. It measures the results under laboratory conditions or collects data from natural events or the use of products. The loss of accuracy and some unexpected factors will be taken into account. Although the experimental data measurements have more reliable results, as it represents the real world, their cost may be too expensive with complex geometries of engineering applications. Many unexpected factors may occur during the measurement that increase the result uncertainty.

- Numerical solution

  It uses an approximate mathematical method to approach the solution. The advantages are the testing models can be easily modified at a relatively low cost by the use of powerful computers, etc. The accuracy of results depends on the employed solution methods and on the number of mesh nodes and time steps used. The use of numerical modeling is becoming popular recently. Most common discretization methods are the finite difference method (FDM), the finite element method (FEM), and the finite volume method (FVM). In this thesis, the numerical simulations are performed using the FVM with computational fluid dynamics (CFD) ANSYS/CFX12.0 software package.

3.2 Water Vapour Transport Phenomenon

In reality, the laboratory experiments under the Martian conditions are relatively expensive compared with Earth's conditions. Further, the continuum hypothesis is well-defined under Earth's conditions. The continuum approach may not be correct when applying to Mars, because the Martian north polar atmospheric pressure close to the regolith is only approximately 720 Pa [Taylor et al., 2010]. At this pressure the mean free path on Mars is estimated to be approximately 200 times bigger than on Earth. Thus the continuum hypothesis of water vapour transport may require corrections due to high Knudsen number. Under Earth's conditions, the Navier-Stokes equations are used to approach the continuum assumption for studying the velocity and pressure fields of a compressible Newtonian fluid. The general form of Navier-Stokes equations for conservation of momentum in Cartesian coordinates can be written as,

$$\frac{\partial \rho u_i}{\partial t} + \nabla \cdot \left(\rho u_i \overrightarrow{U} \right) = -\nabla p + \nabla \cdot (\mu \nabla u_i) + S_i \tag{3.1}$$

where p is the pressure of the fluid, $\overrightarrow{U}$ the velocity vector, and S_i additional momentum sources in the i direction. For mass conservation we have

$$\frac{\partial \rho}{\partial t} + \nabla \cdot \left(\rho \overrightarrow{U} \right) = 0 \tag{3.2}$$

which for an incompressible flow (constant ρ and μ) becomes,

$$\nabla \cdot \overrightarrow{U} = 0 \tag{3.3}$$

3.2.1 Porous Media

Kieffer et al. [1976] and Sullivan et al. [2005] have described porous media that can be used to simulate the regolith. In general, the physical volume of porous medium can be defined as,

$$V_{total} = V_{pm} + V_{air} \tag{3.4}$$

where the V_{total} is total volume of porous medium, V_{pm} the volume of solid material, and V_{air} the volume of air. Base on the mass (m_{pm}) and density (ρ_{pm}) of solid material, the volume of solid material can be represented as,

$$V_{pm} = \frac{m_{pm}}{\rho_{pm}} \tag{3.5}$$

Another useful property of the porous medium is porosity (φ), an average value can be obtained as,

$$\varphi = \frac{V_{air}}{V_{total}} = 1 - \frac{V_{pm}}{V_{toal}} \tag{3.6}$$

The porosity is a ratio (between 0 and 1) of void space comparing to the total volume of the medium. If the number is close to 1, it means that the porous medium has more void space.

Darcy's law is often used to represent the fluid flows through a porous medium. It can be written as

$$\nabla p = -\frac{\mu L}{\varphi K} u_i \tag{3.7}$$

where K is the intrinsic permeability and L is the length scale. The equation is derived from conservation of momentum [Joseph et al., 1982, Do, 1998, Nield and Bejan, 1999]. It shows the proportional relationship between pressure gradient over a distance and the fluid flux through a porous medium. Further, it is applicable to viscous dominant flows, which means that the Reynolds number is small. Another relevant factor, intrinsic permeability, is also related to Darcy's law. It represents the viscosity and diffusion rate of fluid flow to a porous medium and can be defined as [Bear, 1988],

$$K = C d_p^2 \tag{3.8}$$

where C is a non-dimensional constant which depends on porosity and d_p is the effective pore size.

To study the Martian north pole regolith, an example of the Martian properties are summarized in Table 3.1. These conditions will be used to study the influence of dust devils on mass transport mechanism in Martian conditions in Chapter 5.4.

The information was complied by Hudson et al. [2007] and applied by Farahaninia [2008]. It should be noted that the effective porosity may be defined as the effective obstruction factor.

Table 3.1: An example of regolith and atmospheric properties at Martian north pole.

Property	**Value**
Pressure	600 [Pa]
Temperature	263 [K]
CO_2 density	12.07 [g m^{-3}]
Dynamic viscosity	135.09 $\times$ 10^{-7} [Pa·s]
Effective molecular diffusion coefficient	5.5 [cm^2 s^{-1}]
Permeability	10^{-12} [m^2]
Effective porosity	0.21
Ice vapour pressure	256.8 [Pa]
Ice water vapour density	2.11 [g m^{-3}]

3.2.2 Mass Transport of Water Vapour

Mass water vapour transport from the regolith is the main interest of this thesis. To calculate the mass flux of water vapour, both diffusion and advective flux are taken into consideration. Further, water vapour is transported within the air in this fluid mixture (multi-species) case.

In Section 2.2, four primary diffusion types were described: molecular diffusive flux, Knudsen diffusive flux, thermal diffusive flux, and surface diffusive flux. For the diffusion calculation, some assumptions are made to simplify the mass diffusion mechanism.

First, the temperature variation is less than 3^oC during the experiments. It implies that the temperature gradient is very small under the laboratory condition. The isothermal condition can be assumed in the experimental studies and is adapted in the numerical simulations. Because of this, the effect of thermal diffusion can be neglected. Second, a porous medium is used to represent the regolith. Thus the surface diffusion can be neglected [Thorstenson and Pollock, 1989]. Last, the Knudsen

diffusion is negligible under the laboratory conditions. This is due to the molecular mean free path being 10^{-4} smaller than the pore size in the experiment [Prieto, 2006]. However, the Knudsen diffusion correction has to be applied when simulating under Martian conditions. It is because the pore size of Martian regolith is in the order of the molecular mean free path. In other words, the mean free path is greater than the geometrical length scale of pores under Martian conditions. Therefore, to estimate the Martian diffusion flux, we have to consider both molecular and Knudsen flux.

Based on these assumptions, the diffusive flux can be simplified to

$$J_{diff} = -D_{eff}\frac{\partial \rho_w}{\partial z} \tag{3.9}$$

where ρ_w is the water vapour density and D_{eff} is the effective diffusion coefficient of water vapour. It should be noted that the Equation 3.9 is a general governing equation of mass diffusive flux, which can be applied on water vapour transport within the air and CO_2. On Earth, the effective diffusion coefficient can be represented using the molecular diffusivity, because the Fick's law of diffusion is the only diffusive flux, which is applied to the Earth's conditions. On Mars, the Knudsen diffusive flux has to be taken into consideration. The effective diffusion coefficient is then applied with the porous medium correction [Mason and Malinauskas, 1983]. The diffusion coefficient correction in a porous medium can be obtained as

$$D_{eff} = \frac{\varphi}{\tau}D' \tag{3.10}$$

where τ is the tortuosity of porous medium and D' is a binary species transition diffusion coefficient, which can be defined as

$$\frac{1}{D'} = \frac{1}{D_K} + \frac{1}{D_{wc}} \tag{3.11}$$

where D_K is the Knudsen diffusion coefficient and D_{wc} is the binary diffusive coefficient of water vapour. More detailed study of Martian effective coefficient is described by Hudson et al. [2007].

It is important to mention that water vapour transport may be enhanced by the dust devils on Mars. Flow may go into the regolith with less water vapour density (bulk

air humidity) and go out with a higher one. In this case, the advection flux cannot be ignored and can be denoted as

$$J_{conv} = \rho_w U_z \tag{3.12}$$

In terms of total flux of water vapour from the regolith, it can be estimated by combining both advection flux and diffusive flux [Bird et al., 2001],

$$J_{tot} = J_{diff} + J_{conv} \tag{3.13}$$

3.3 Kinematic Similarities of Dust Devils

Local kinematics of the dust devils is relevant for the simulation of water vapour transport. It may help define how much water vapour will be enhanced by the dust devils by ensuring that the vortex in the laboratory is similar to the simulation and to real atmospheric vortices. As described in section 2.4, a fully developed, steady, atmospheric vortex flow can be divided into five regions, illustrated in Figure 2.2 [Snow, 1982, Lewellen, 1993]. The formation of vortex structure can be varied during the vortex flow development. Since the vortex generator most likely would produce one-cell dust devil-like flow only, the multi-cell case was not included in this study. We focused on the corner flow and inflow regions, because they have direct contact with the regolith and so direct impact on the water vapour transport.

A number of relevant characteristic parameters of dust devils were discussed in section 2.5. They were generally based on three main types of characteristic parameter, 1) swirl ratio, 2) Reynolds number, and 3) aspect ratio. In this thesis, the swirl ratio is determined under two different definitions. One is determined using Equation (2.15) which was used by Haan et al. [2008] and Kuai et al. [2008]. The reason for its use is that it is applicable to Gallus type of vortex apparatus, which has been used to study water vapour transport mechanism in this thesis. The other form of the swirl

ratio is a modified equation based on Equation (2.8), which is defined as

$$S_{core} = \frac{r_{core} U_{t_{core}}}{2 h_{core} U_{r_{core}}} \tag{3.14}$$

where $U_{t_{core}}$ is an average maximum tangential velocity, $U_{r_{core}}$ the average radial velocity at r_{core} region, and h_{core} the depth of inflow at r_{core} region. It should be noted that the updraft volume flow rate within the core ($2\pi r_{core}^2 U_{z_{core}}$) has the same amount as the inflow volume flow rate through the depth of the core region ($2\pi r_{core} h_{core} U_{r_{core}}$). Hence, h_{core} can be calculated by

$$h_{core} = \frac{r_{core} U_{z_{core}}}{U_{r_{core}}} \tag{3.15}$$

where $U_{z_{core}}$ is the average vertical velocity at the radius of vortex core. This is different from the depth of the inflow, h, and has the advantage that the average radial velocity is easy to estimate in the natural vortex flows [Barcilon, 1967]. The last streamline before the circulation of the whole vortex structure exhibits weak dependence on the vortex core, which is defined at the radial location of maximum azimuthal velocity. According to the Rankine vortex flow, the maximum azimuthal velocity does not happen at the radial location of last streamline. In addition, the aspect ratio and Reynolds number in the radial direction used in this thesis are defined as

$$a_{core} = \frac{h_{core}}{r_{core}} \tag{3.16}$$

and

$$Re_{core} = \frac{2\pi r_{core} U_{r_{core}}}{\nu} \ . \tag{3.17}$$

Since the dust devils are highly dynamic, it is difficult to locate their position in the numerical simulations. A brief description of how to approach the velocity components, the core radius, and the inflow depth is needed. First, we create profile lines at different heights from 0.02 m to 0.10 m with 0.02 m spacing, and in each level we create four horizontal lines with 45 degree angle rotation. Second step is to determine the maximum tangential velocity and its location at each line. Third, the vertical velocity is estimated by taking the integral within the core region at each line. Fourth,

the radial velocity is recorded at the core radius at the maximum tangential velocity. All the velocity components and core radius at each line are averaged with several time steps. Finally, the inflow depth can be estimated with the above information using Equation 3.15.

3.4 SPIV systems and physics of the measurement technique

SPIV is an experimental method for measuring the three components of a velocity vector of the flow field on a two dimensional plane at an instant of time [Adrian, 1991, Dooley, 2005, Raffel et al., 2007]. This method calculates the velocity vector on a plane using

$$\overrightarrow{U} = \frac{ds}{dt} \simeq \frac{\Delta s}{\Delta t} \tag{3.18}$$

where the velocity $\overrightarrow{U}=(u, v, w)$ is approximated from the displacement $\triangle s$ from time t to time $t+dt$. It is derived from Taylor series expansion and assumed there is no acceleration ($\frac{d^2s}{dt^2}$=0). Higher order terms are also neglected because the values are small compared to the first order term.

With SPIV method the velocity of the vortex flow is measured by recording the displacement of small particles of same size, which are carried with the flow. The seeding particles used were produced by a smoke generator and they are typically sufficiently small (order of 0.3 microns) to follow the flow. The seeded flow field is illuminated by a double pulsed laser, which fires two laser beams within a short time $\triangle t$ in Equation (3.18). A camera, which is placed perpendicular to the light sheet, is capturing these two images of the illuminated particles. The pixelization of images is transferred into sub-interrogation regions. Particle image locations can be determined using a correlation approach, namely a discrete cross-correlation function [Raffel et al., 2007], defined as

$$\phi_{fg}(x, y) = \sum_{i=-\infty}^{\infty} \sum_{j=-\infty}^{\infty} f(i + x, j + y)g(i, j) \tag{3.19}$$

where f and g are the intensity values, which are extracted from the images. Generally, f is larger than the template g. The values of x and y are the shift distances, which can be positive or negative. The sum of the products of all overlapping pixel intensities produces one cross-correlation value $\phi_{fg}(x, y)$. By calculating cross-correlations in the interrogation area, the highest peak results when the particles match up with their corresponding shifted particles. A validation process helps to correct the error of the velocity vectors, shown as red arrows in Figure 3.1, that occur during image reconstruction at cross-correlation step.

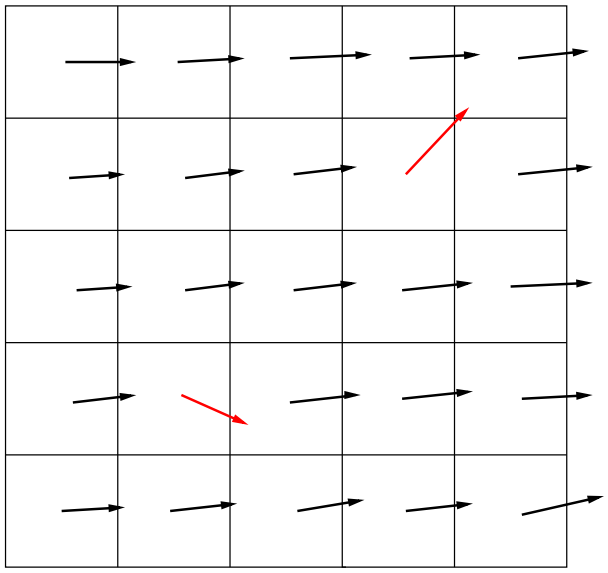

Figure 3.1: An example of the error in the velocity vectors.

Figure 3.2 shows an angle displacement method that is used to calculate the local displacement vector by the viewing direction and magnification factor for each camera [Raffel et al., 2007]. The tilting of image planes and camera lenses, which is associated with this configuration, causes image distortion but keeps the images in complete focus. The correlation between the object plane (X, Y) and the image (x,y) may be described through geometric optics and obtained as

$$X = \frac{fx \sin\phi}{M_0 \sin\theta(x \sin\phi + fM_0)} \tag{3.20}$$

$$Y = \frac{f_l y}{x \sin\phi + f_l M_0} \tag{3.21}$$

where f_l is the lens focal length, ϕ and θ are the angles between the various plane, and M_0 is the nominal magnification factor. This configuration does not incorporate lens distortions and is sensitive to small variations in each parameter. This will result in some errors of the actual positions.

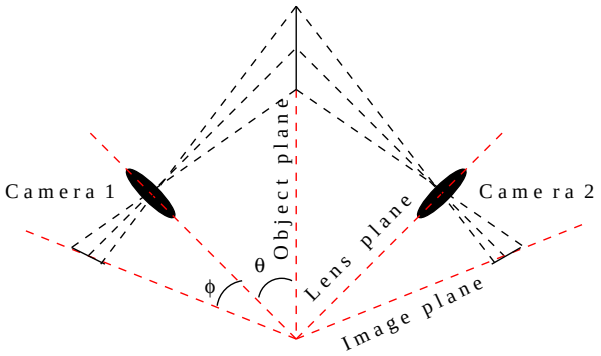

Figure 3.2: The angle displacement method with a tilted back plane.

Since the local displacement vector has been determined, it is possible to reconstruct a three dimensional velocity field through its geometry from two projected displacement fields. An illustration of velocity components is shown in Figure 3.3. The velocity components measured by the left camera are given by

$$u_1 = -\frac{x_i' - x_i}{M_0 \Delta t} \tag{3.22}$$

$$v_1 = -\frac{y_i' - y_i}{M_0 \Delta t} \tag{3.23}$$

Similarly, the velocity components u_2 and v_2 for the right camera can be found. Using these equations, the velocity components $\overrightarrow{U} = U(u, v, w)$ is then obtained using

$$u = \frac{u_1 \tan\alpha_2 + u_2 \tan\alpha_1}{\tan\alpha_1 + \tan\alpha_2} \tag{3.24}$$

$$v = \frac{v_1 \tan\beta_2 + v_2 \tan\beta_1}{\tan\beta_1 + \tan\beta_2} \tag{3.25}$$

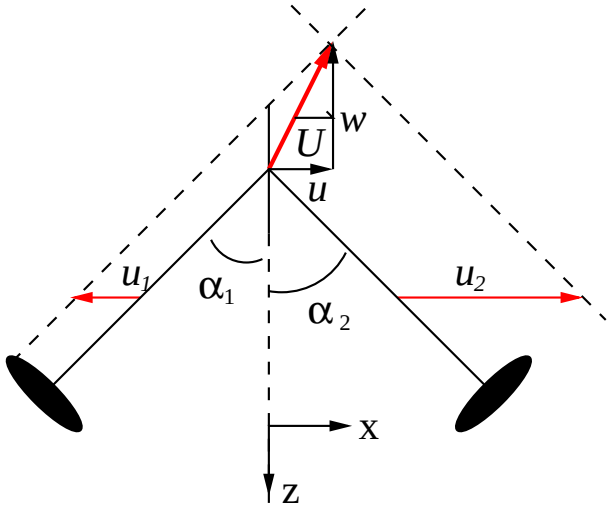

Figure 3.3: The velocity components in the XZ-plane.

$$w = \frac{u_1 - u_2}{\tan\alpha_1 + \tan\alpha_2} = \frac{v_1 - v_2}{\tan\beta_1 + \tan\beta_2} \tag{3.26}$$

where α and β define the angle within the YZ plane and α_i,$\beta_i \geq 0$.

Finally, these formulae give three velocity components, which are measured by SPIV measurement techniques. Some errors such as velocity vector may be incurred during the configurations and neglections. Nevertheless, the accuracy of this measurement technique is still very good comparing with other measurement techniques. Hence, SPIV technique was employed to measure the velocity field of vortex flows.

3.5 Computational Fluid Dynamics (CFD)

In principle, a dust devil is a highly turbulent and transient flow in the atmosphere. Analytical solutions for this type of flow motion are very difficult to obtain. The numerical method will be a better choice for approaching this study. A numerical software package, ANSYS/CFX12.0, is used to design an optimized vortex generator and to simulate the water vapour transport. It is based on the FVM. The domain is first divided into a set of control volumes (CVs). A generic conservation equation for

any type of fluid flow can be written as [Versteeg and Malalasekera, 1995],

$$\frac{\partial \rho \phi_c}{\partial t} + \nabla \cdot \left(\rho \phi_c \overrightarrow{U} \right) = \nabla \cdot \left(\Gamma_\phi \nabla \phi \right) + S_\phi \tag{3.27}$$

where ϕ_c is the intensive transport quantity and Γ_ϕ the diffusivity coefficient, and S_ϕ the source term. The equation can be rewritten in an integral form as,

$$\frac{\partial}{\partial t} \left(\int_V \rho \phi_c dV \right) + \int_A \mathbf{n} \cdot \left(\rho \phi_c \overrightarrow{U} \right) dA = \int_A \mathbf{n} \cdot \left(\Gamma_\phi \nabla \phi_c \right) dA + \int_V S_\phi dV \tag{3.28}$$

where A is the surface of the control volume, and $\mathbf{n}$ is a vector normal to the surface. This equation will be integrated over the each CV and then produced the balance solutions at the center point of the CVs.

3.5.1 CFX Meshing

In the numerical study, three dimensional domains were generated and meshed using the ANSYS Workbench and the ANSYS CFX-Mesh, respectively. There are three main types of grids: Cartesian (Orthogonal), non-orthogonal structured, and unstructured grids can be selected. Cartesian and non-orthogonal structured grids are not considered, because they are limited in use and hard to generate due to the complicated geometry. From those disadvantages, the unstructured mesh was selected. It is known that unstructured grids may introduce larger artificial diffusion. However, the use of inflated layers (the mesh perpendicular to the chosen surface) and increase of mesh resolution would help to improve the solution.

Each new numerical simulation starts from a fast and coarse mesh for the purpose of saving the cost. The refinement is made in the locations where the flow structure is of interest or has a high Courant number. The Courant number is relevant to the accuracy of transient solutions and can be defined as,

$$Courant = \frac{\overrightarrow{U} \Delta t}{\Delta x} \tag{3.29}$$

where Δt is the timestep, and Δx is the local mesh size. It also presents the relationship between the speed of flow field and mesh size at each timestep. In this study, the

region of dust devil and the atmosphere-regolith interface are the special locations. Because of this, the inflated layers and finer mesh are applied in those regions.

High mesh resolution usually results in more accurate solution with the appropriately setup. On the other side, it may require more computer power and increase the cost. The improvement of numerical solutions is not proportional to the rate of refinement. Therefore, the analysis of grid independence is included to find more efficiency of mesh setup. It also could be used to verify that the solution difference between the coarse and fine meshes is less than a reasonable value. Richardson extrapolation [Ferziger and Peric, 2002] is often used to obtain and to calculate the exact solutions. First of all, the discretization method is based on Taylor series and can be obtained as,

$$f(x) = f(a) + \frac{f'(a)}{1!}(x-a) + \frac{f''(a)}{2!}(x-a)^2 + \frac{f'''(a)}{3!}(x-a)^3 + \cdots . \tag{3.30}$$

To approach the solution, the truncation error of Taylor series (ϵ_h^d) can be expressed by,

$$\epsilon_h^d = f(x) - F_{\Delta x} \tag{3.31}$$

where $F_{\Delta x}$ is the approximation of Taylor series. In other words, it is the numerical solutions. However, the exact solution is usually unknown. Fortunately, it is possible to calculate the truncation error by the following steps. Equation 3.32 shows the order of the scheme, p, can be estimated from three calculations performed with progressively refined grid sizes.

$$p = \frac{\log(\frac{F_{\Delta x_2} - F_{\Delta x_1}}{F_{\Delta x_3} - F_{\Delta x_2}})}{\log(a^{\frac{1}{3}})} \tag{3.32}$$

where a is a constant refinement rate which can be defined as,

$$a = \frac{N_2}{N_1} = \frac{N_3}{N_2}. \tag{3.33}$$

where N_1, N_2, and N_3 are the number of nodes in the coarse, medium, and fine grids, respectively. The truncation error can be then estimated by,

$$\epsilon_h^d = \frac{F_{\Delta x_3} - F_{\Delta x_2}}{a^{(p)} - 1}. \tag{3.34}$$

Finally, the exact solution can be obtained as,

$$F_{exact} = f(x) \approx F_{\Delta x_3} + \epsilon_h^d. \tag{3.35}$$

3.5.2 CFX Solver

Turbulent flows may be modelled using a Reynolds averaged Navier-Stokes (RANS) model, large eddy simulation (LES), detached eddy simulation (DES), or direct numerical simulation (DNS). Our simulations used RANS models which are based on the Navier-Stokes equations [ANSYS, 2009]. The advantages of RANS are 1) relatively cheap comparing to LES, 2) can be calculated with coarse mesh, 3) be able to solve with complicated models, and 4) good for most engineering applications. However, The RANS models may not be able to well handle the flow separation problems, in contrast to LES which obtains better solution of large-scale turbulent fluid motion [Rodi and Mulas, 2005]. In RANS models, the fluid velocity may be divided into averaged and fluctuating velocity components in the transport equations, given by:

$$\overrightarrow{U} = \overrightarrow{\overline{U}} + \overrightarrow{u'} \tag{3.36}$$

This method also allows the averaged equations to be solved for transient flow using CFX. The most common RANS models are:

- k-ε Model

  The k-ε turbulence model, developed by Launder and Spalding [1974], is categorized as one of Eddy Viscosity Models (EVM) in RANS. It includes turbulent kinetic energy (k) and turbulence eddy dissipation (ε) in the transport equations. This model is not only good for general engineering flows applications but also provide faster convergence of an initial result. However, it is well known that rotating flows may not be suitable using this turbulence model, which was confirmed by Prieto [2006].

- Reynolds Stress Model (RSM)

It introduces six additional variables of the Reynolds stress tensors in the transport equations. In this study, the SSG-RSM model [Speziale et al., 1991], which uses a quadratic relation for the pressure-strain correlation term [ANSYS, 2009], is used to solve the vortex flow simulations. The advantages are higher degree of universality and better solutions for the swirl flows.

ANSYS/CFX12.0 also uses different types of numerical advection schemes to solve the equation 3.28 [ANSYS, 2009]. They are:

- Upwind Differencing Scheme (UDS)

  This is the first order space and very robust. However, it is not suitable for low diffusion problems because of diffusive discretization errors. In other words, it adds artificial diffusion to the solutions especially for coarse grids.

- Central Differencing Scheme (CDS)

  This scheme is the second order in space and provides the most accurate scheme. It has no artificial diffusion and is good for oscillating flows.

- High Resolution and Specified Blend Factor

  Both high resolution scheme and specified blend factor are almost second order in space and are the blends between UDS and CDS. The specified blend factor is a manual input value between 1 and 0. Typically, the blend factor to 1 means pure CDS and to 0 means pure UDS. For the high resolution, CFX will adjust the blend factor depending on the solutions. When small gradients and fine grids are present, the blend factor may lead to 1 (CDS). It may lead to 0 (UDS) in the regions of high flow gradients to prevent non-physical oscillations.

Chapter 4

Vortex Generator Design

Since a dust devil is hard to locate the event's place and to control its strength, a vortex generator was often used to study this type of vortex flow. From Prieto's study [Prieto, 2006], the existing Open-type vortex apparatus built at the University of Alberta was not able to produce the desired velocity profiles of dust devils. As a result, the modification of this vortex generator is needed. A new design of vortex apparatus should consider the following goals:

- A redesigned vortex generator should be able to produce the desired structure of vortices and kinematically similar to dust devils.
- The physical scale of the vortex generator should be able to not only fit in the laboratory room, but also not exceed the width of the water tank. (The size of the laboratory environment is 6.05 m $\times$ 3.54 m $\times$ 3.40 m and the size of the water tank is 2.00 m $\times$ 1.00 m $\times$ 0.20 m.)

Figure 4.1 shows the procedures used for designing a new vortex generator. It consists of a combination of numerical simulations and laboratory experimental validations. Numerical simulations are studied using the commercial package ANSYS/CFX12.0 based on the finite volume method. Numerical results may help to lower the cost of designing a vortex generator, such as optimizing the geometry of enclosure, reducing

the amount of experiments, etc. The idealized geometric dimensions are taken from the recommendations by Altimas [2007]. Numerical results are compared with the characteristic parameters. A modified vortex generator is constructed based on the best agreement between the numerical results and the desired structure of dust devil. A safety factor is taken into account for building the solid structure of the new vortex generator in the laboratory environment. The detailed design drawings can be found in Appendix B. Velocity profiles, which are produced with different fan speeds, are measured using the SPIV technique. The results are verified by comparison with other experimental data from the literature and then used for validation of the numerical simulations.

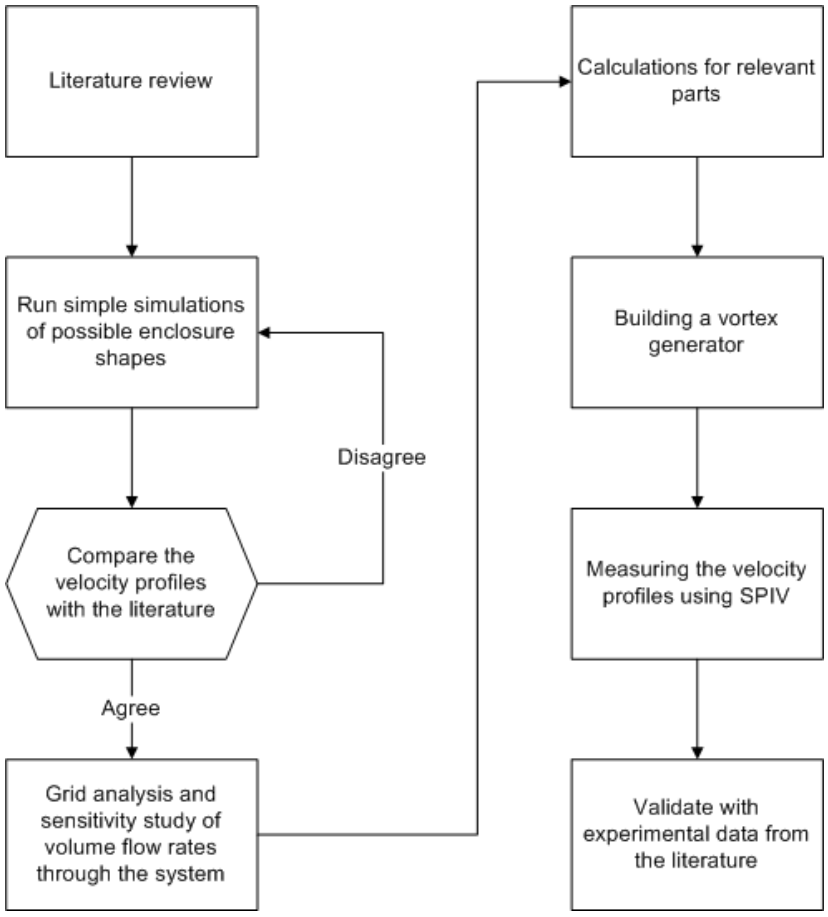

Figure 4.1: A flowchart for designing a suitable vortex generator.

4.1 Numerical Simulations for the Vortex Generator Design

Designing a capable vortex generator is an important initial step for this project. The use of computational fluid dynamics simulations is a good approach, as it allows for quickly understanding the relationship between the local flow kinematics and the apparatus geometries. From Altimas [2007], Haan et al. [2008], and Kuai et al. [2008] studies, a suitable vortex generator should consist of three main components, the cylinder-electrical motor combination, the enclosures with the air duct in between, and several curved fins or several angle adjustable vanes.

A series of sensitivity studies of the new apparatus were performed by Altimas [2007]. The results show that the relevant parts are the fin angle, outflow radius, and inlet height, as illustrated in Figure 2.7. As a result, the additional numerical simulations for the vortex generator modification should focus on these parameters. However, the geometry of the fins used by Altimas [2007] is very difficult to construct in practice, because they are located at the vertical section of the cylinder enclosures. Octagonal and decagonal enclosures were considered and simulated as the alternative solutions. However, a significantly large amount of eddies and recirculation, which results in poor local kinematic, may be introduced by the edges. The eddies and the recirculation may increase the uncertainty and instability at the inflow region. As a result, a Gallus type of vortex generator is deemed to be the most feasible and build-able structure for this project.

Initially, Altimas [2007] simulated a Gallus type vortex generator with the smaller scales. The dimensions of the numerical model was within 1 m in diameter for the enclosure size. The size of the vortex generator was much smaller than the one at Iowa State University. Due to limitations of computer power at that time, the models were simulated with the k-ε turbulence model and only a pie-shaped section was used. The vortices had nearly died out when the flow traveled downward through the vertical duct of cylindrical enclosures. This was the main reason why the fins

were evenly placed at vertical duct circumferentially in his study. However, the k-ε turbulence model was not the best modeling set-up for the vortex flow simulations [ANSYS, 2009]. A significant amount of artificial diffusion is added to the simulation results. Both the shrinking of the geometry and the use of a poor turbulence model contributed to the loss of the vortices, but which one had most influence to the results was unknown.

To improve the Altimas [2007] study, the Reynolds Stress Model (RSM-SSG) turbulence model is employed in all simulations in this thesis. Further, a full three-dimensional numerical model is used instead of the wedge shaped model. The main advantages of these two changes are increase of the solution accuracy and increase of the investigation field for the validation, respectively. Combining both Altimas [2007] and Gallus et al. [2006] design ideas, a modified vortex generator is mainly based on Gallus type of vortex generator, but used curved fins instead of flat vanes. Church and Snow [1993] found that the curved fins might introduce better vorticities than flat vanes. In addition, curved fins may resolve the problem of the dissipated vortices in the Gallus type of vortex generator. This significant improvement was confirmed, as the vorticities remained strong, when the flow traveled down through the vertical duct.

Figure 4.2 shows the goal of the laboratory experimental setup with the relevant geometric parameters in this thesis. At initial design stage of vortex generator, the numerical simulations would not include the porous media. The use of porous media in numerical simulations may provide a better understanding of actual flow field for the experimental study. However, to test the main characteristics of the vortex flow such as the vortex structure, the effect of a porous medium at the bottom surface is not needed and can be neglected. Therefore, a flat panel is used instead of the experimental tank for the first part of this thesis.

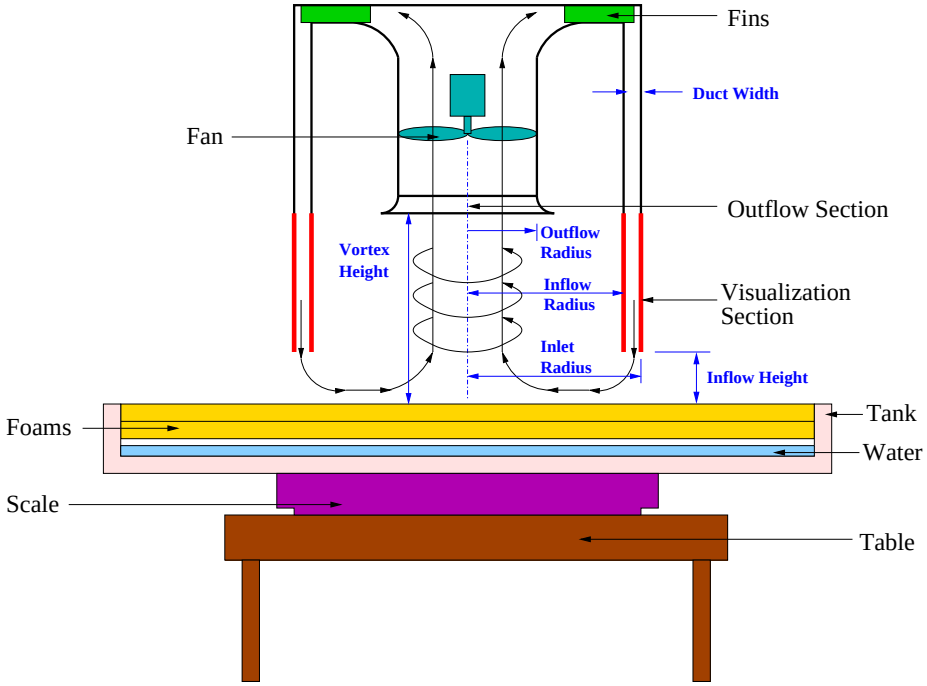

Figure 4.2: Schematic of experimental set-up with the relevant geometric parameters.

4.1.1 Model Setup for Designing the New Vortex Generator

The numerical simulations are performed with the vortex generator part only. The scales of the most relevant characteristic parameters are recorded in Table 4.1. The chosen scaling is referred to Altimas [2007] study. Outflow radius adjustment is made with a restriction ring at the entrance of the outflow region. It should be noted that the diameter of the internal cylinder does not change with the outflow radius. Figure 4.3 shows a three-dimensional domain with a typical mesh. An unstructured tetrahedral grid is applied to the majority region and an inflation layer of 10 control volumes is used at the bottom surface, which is used as the ground. Both types of mesh are created using a mesh generation tool of CFX-Mesh [ANSYS, 2009]. The refinement mesh is implemented at the vortex core region for better accuracy and convergence, since the turbulence kinetic energy (TKE) is higher there.

Table 4.1: Apparatus geometry used for three-dimensional numerical model.

Parameter description	**Value**
Inlet radius	500 mm
Inflow radius	445 mm
Inflow/Inlet height	150 mm
Outflow radius	225 mm & 120 mm
Vortex height	700 mm
Duct width	55 mm
Fin angle	90^o
Fin radius	200 mm
Fin space	45^o

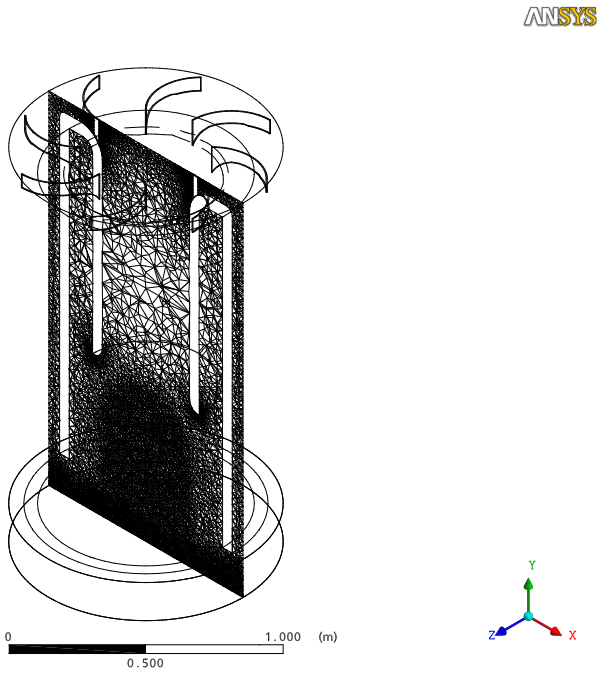

Figure 4.3: A three-dimensional numerical model of vortex generator with the diameter of 450 mm and the use of typical mesh.

Transient simulations are performed with a second order backward Euler time discretization scheme and a high resolution scheme for the transient terms and advection terms, respectively. A reasonable timestep of 0.02 s is selected to evaluate the characteristic parameters. Low Courant number can be achieved within this timestep, which means the simulations are relatively accurate and non-diverged. The atmospheric conditions are set to an isothermal, incompressible, and Newtonian fluid of air. At dry blub temperature of 20 °C, the air density (ρ_a) is 1.204 kg m^{-3} and the air dynamic viscosity is 1.825e-5 kg m s^{-1} [Çengel, 2002]. Convergence criteria requires the value of the residual RMS to be less than 10^{-4}. The Reynolds Stress Model (RSM-SSG) turbulence model is employed for better numerical solutions.

The boundary conditions of duct walls and ground are modeled using a no-slip condition. The inflow boundary (see Figure 4.2) is modeled using a free-slip condition. This is because the flow is assumed be under a perfectly recirculated condition, which means no air escape/enter through the gap at the inflow height. An axial momentum source is introduced at a cylindrical domain which represents the fan inside the internal cylinder. In addition, a honeycomb feature is applied to this domain in order to isolate the momentum source from the vortex flow. It should be noted that the honeycomb feature would reduce the tangential velocity generation in the numerical models. This is because a significant amount of resistance would be applied. For the sensitivity study purpose, this is acceptable. A commercial fan blade would be used to lower the cost of design in this study. It has the ability to generate the volume flow rate of 0.94 m^3 s^{-1} at the maximum RPM of 1725. Hence, the swirl ratios are calculated within this range of volume flow rate.

4.1.2 Grid Analysis

The accuracy of numerical simulations depends on the mesh size. Although this factor is very relevant, the gain of accuracy is not necessarily proportional to the grid refinement rate. Computational efficiency may also decrease by the increase

of mesh resolution. Grid analysis is often used to define the best mesh size for the numerical studies. Richardson extrapolation can be employed to determine the relative discretization error and to calculate estimates of the exact solutions. It should be noted the majority of the grid refinement is applied at the region of interest. In other words, increased mesh density would be applied at the vortex core region.

A refinement ratio of approximately $1.5^{1/3}$ is used to the mesh sensitivity study. Figure 4.4 shows the average volume flow rates that correspond to five different levels of mesh density with two different outflow diameters. The relative discretization errors are determined using the Richardson extrapolation and the relevant factors are shown in Table 4.2. The grid sizes from level 1 to 5 correspond to the mesh densities in Figure 4.4. In other words, the higher number of grid size means the finer mesh density. To validate the Richardson extrapolation, the order of the scheme should be between 1 and 2. It means a grid-independent (asymptotic) solution level is reached in the numerical models. The mesh sensitivity results show that the grid in the grid independent region may be obtained approximately at the grid size of 600,000. To balance between the solution accuracy and computational efficiency, the number of nodes approximately to 600,000 is applied to the numerical simulations of vortex flow field analysis.

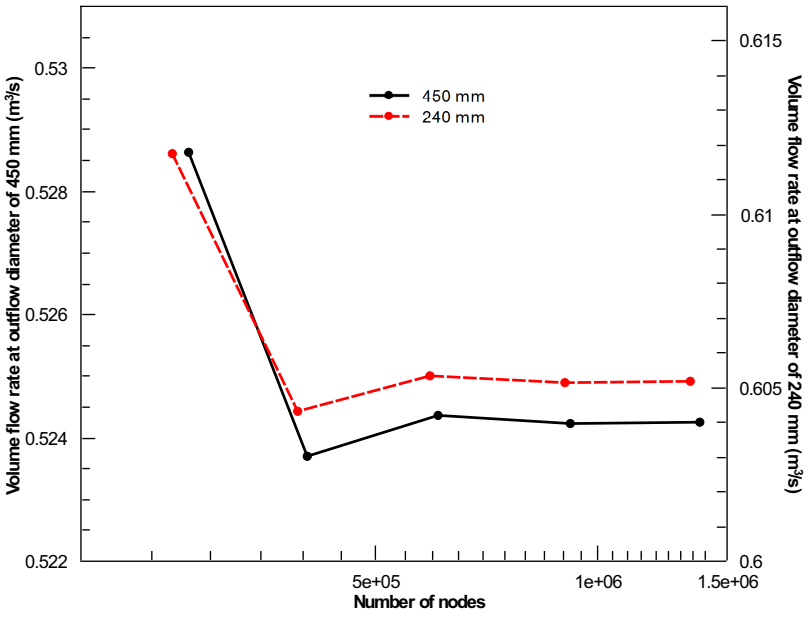

Figure 4.4: Mean volume flow rate through the fan as a function of grid sizes.

Table 4.2: The relevant parameters of grid analysis.

Outflow diameter	**Grid size**	**Order of scheme** (p)	ϵ_h^d
450 mm	1, 2, 3	1.09	0.00427
	2, 3, 4	1.89	-0.00052
	3, 4, 5	1.57	0.00012
240 mm	1, 2, 3	1.11	0.00639
	2, 3, 4	1.71	-0.00082
	3, 4, 5	1.60	0.00017

4.1.3 Numerical Results of Vortex Flow Field

From the results of grid analysis, the level 3 gird size is chosen for the sensitivity study of volume flow rate. The number of nodes of 609,276 and 593,369 are used for the outflow diameter of 450 mm and 240 mm, respectively. The detailed setups of the numerical models can be found in Section 4.1.1. This section will be focused on the effective of volume flow rate between two different outflow diameters.

Figure 4.5 shows the mean maximum tangential velocity is relatively proportional to the volume flow rate. The outflow diameter of 450 mm has better agreement with the linear relationship. A large standard deviation happens at higher flow rate with the small diameter case. It is believed that the back eddies or recirculation are present when the flow goes through the restriction. Higher flow rate would result in higher instability in the measurement.

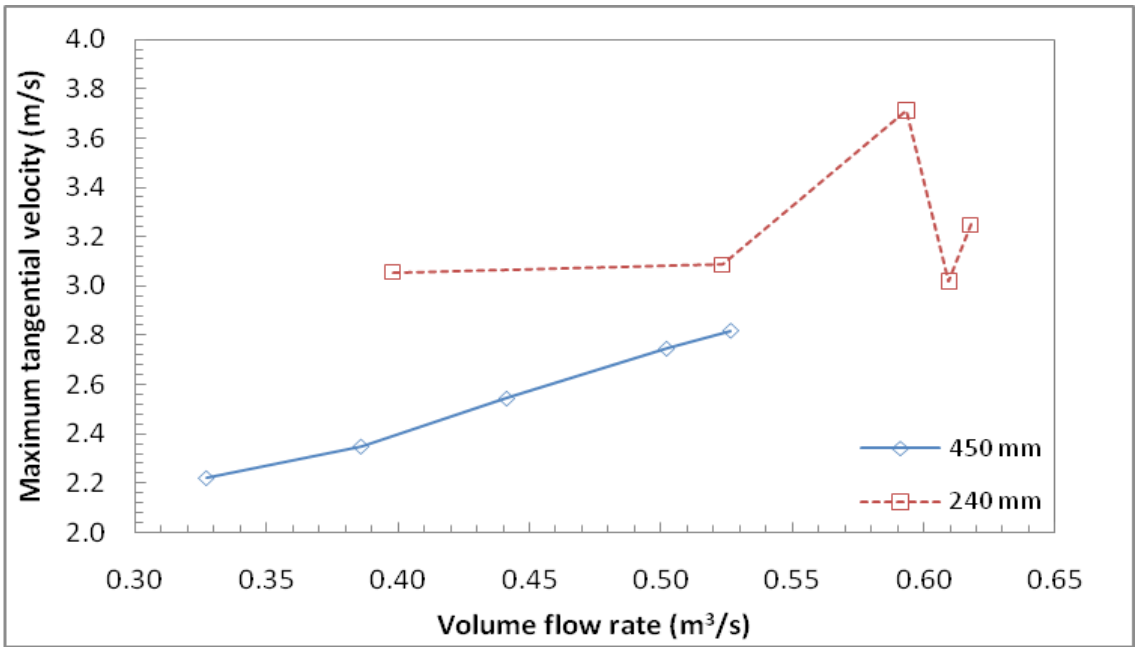

Figure 4.5: Mean maximum tangential velocity as a function of volume flow rate with honeycomb feature.

Figure 4.6 shows the core radius increases with increasing outflow radius. From this information, the variation of outflow radius can be a control factor to adjust the size of vortex flow. This agrees with previous studies, e.g. Nolan and Farrell [1999] and Altimas [2007]. Generally, the shape of vortex flow, which is characterized by aspect ratio, does not vary with the outflow radius in Figure 4.7. However, it has slight tendency of the decrease of outflow radius increasing the aspect ratio when compared with the volume flow rate at 0.395 m^3 s^{-1} and 0.515 m^3 s^{-1}. More investigations are required on the effect between this control strategy and the aspect ratio in the SPIV

experiments.

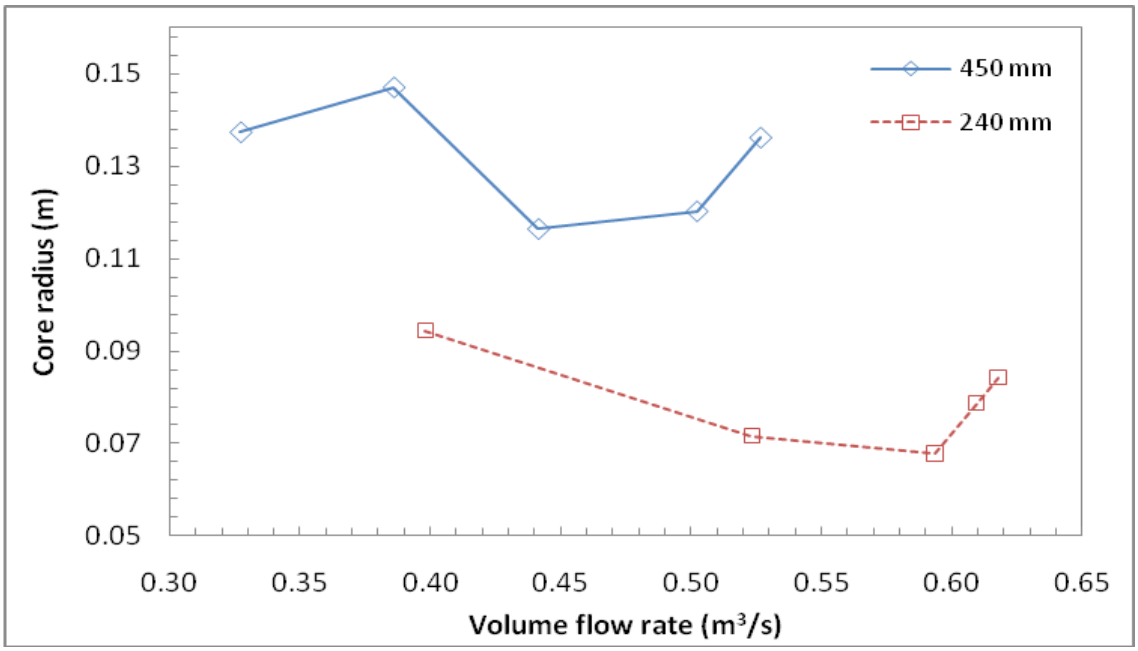

Figure 4.6: Core radius as a function of volume flow rate with honeycomb feature.

Figure 4.8 shows the results of two different types of swirl ratio definitions. Swirl ratio estimated using Gallus et al. [2006] definition provides that increasing outflow radius and decreasing volume flow rate would result in the increasing swirl ratio. They agree with Altimas [2007] and Haan et al. [2008], respectively. It should be noted that the range of S_{gallus} indicates that the use of numerical models can be applied to the modification of vortex generator. In contrast, a vortex generator with smaller outflow radius produces a higher the core swirl ratio, S_{core}. This makes more intuitive sense than the results of S_{gallus}. In general, the swirl ratio is a dimensionless character of vortex strength. When applying the same amount of flow rate to different outflow radius, a smaller one usually has higher concentration force.

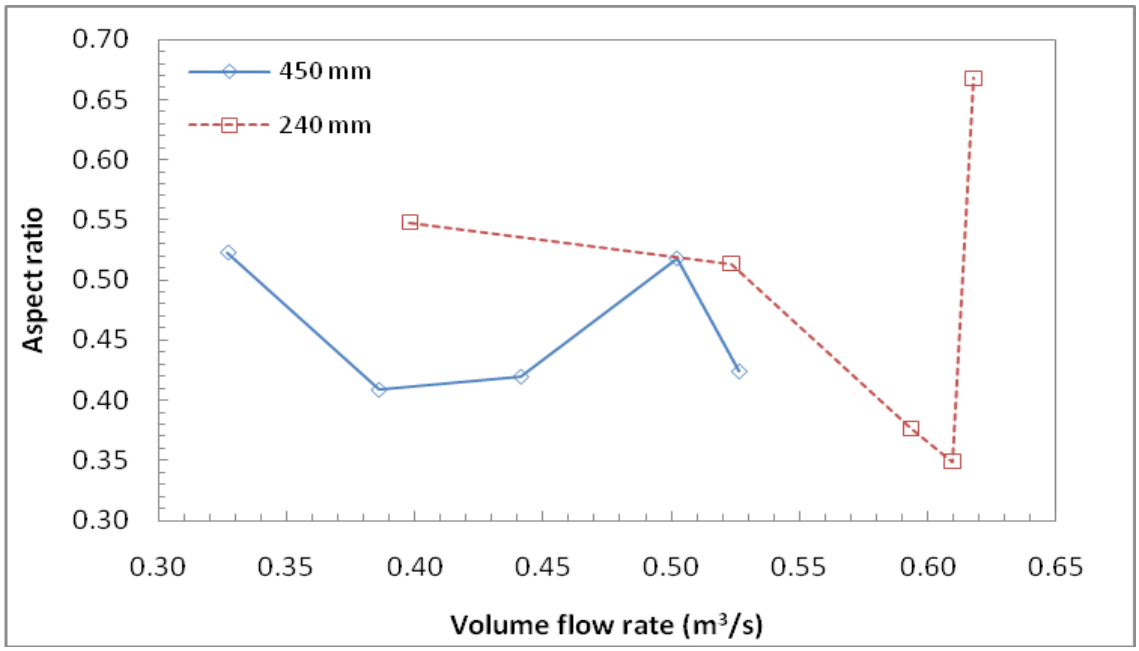

Figure 4.7: Aspect ratio varies with volume flow rate with honeycomb feature.

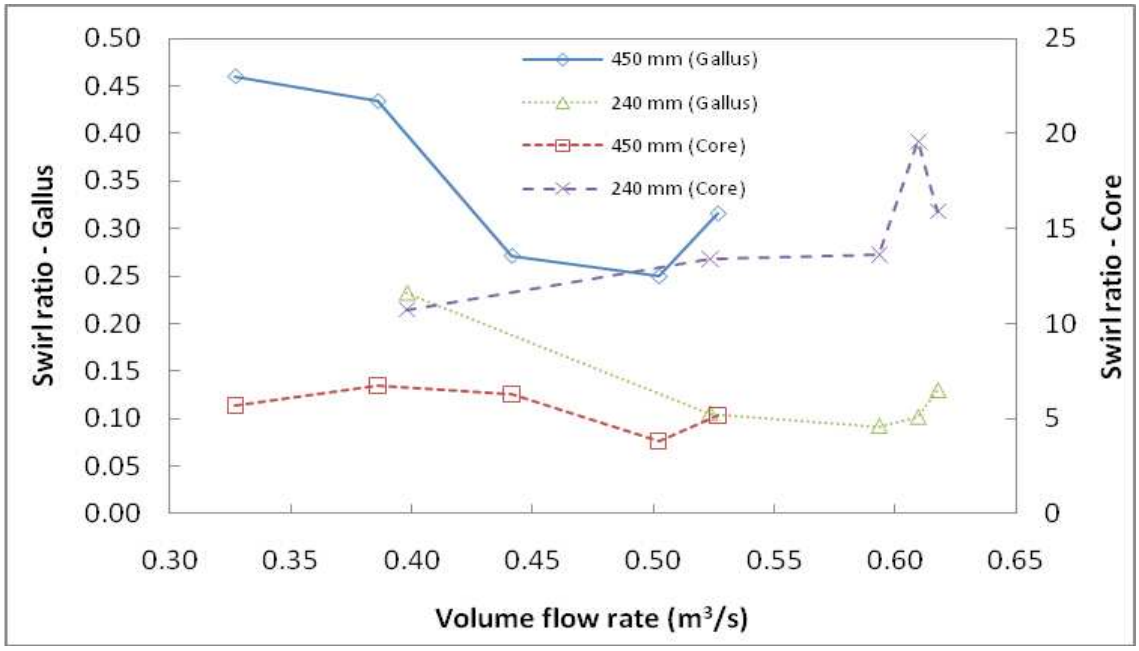

Figure 4.8: Swirl ratio estimated using Gallus definition varied with volume flow rate with honeycomb feature.

Figure 4.9 shows that the radial Reynolds number at the vortex core (Re_{core}) does not vary much with the flow rate, especially for the 240mm cases. This is because, as the radial velocity increased, the core radius reduced proportionally, due to the presence of honeycomb feature. The radial Reynolds number is higher for larger outflow radius. It means that the radial Reynolds number is proportionally associated with the core radius, when the radial velocity is changed slightly.

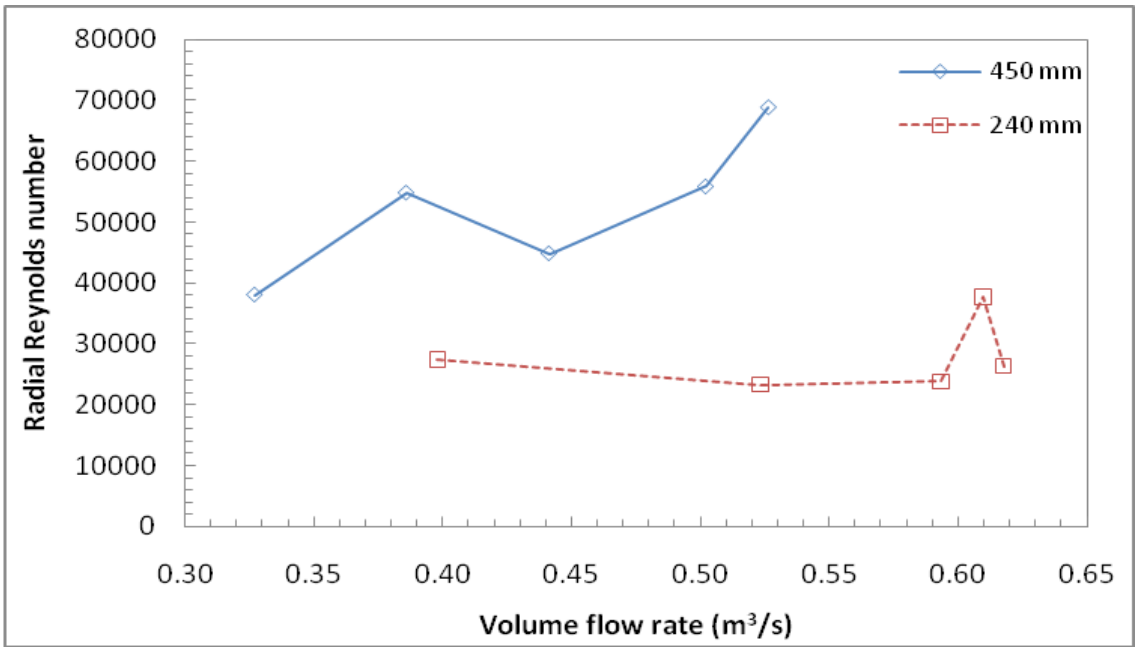

Figure 4.9: Radial Reynolds number as a function of volume flow rate with honeycomb feature.

4.2 Stereo Particle Image Velocimetry (SPIV) Experiment

A modified vortex generator was tested with the SPIV technique. By recording the velocity fields, the significant results helped validate the numerical simulations. It should be noted that the previous numerical simulations (sensitivity analysis) were not validated with the SPIV measurement. The flow field validated with SPIV is the one from the numerical simulations for water vapour transport study. The reason is that a small modification was made in the vortex apparatus, namely there is no honeycomb in the experimental apparatus. In fact, the fan blade created helical wind profiles which created additional vorticity. This does not agree with the numerical setup in the sensitivity studies. However, the previous numerical results were still good for the sensitivity studies. In addition, a flat plane was used as the regolith, instead of a porous medium tank, which was used with the water vapour transport experiments. The flat plane was used to avoid potential turbulence generated by the sensors. The SPIV experimental procedures are illustrated in Figure 4.10.

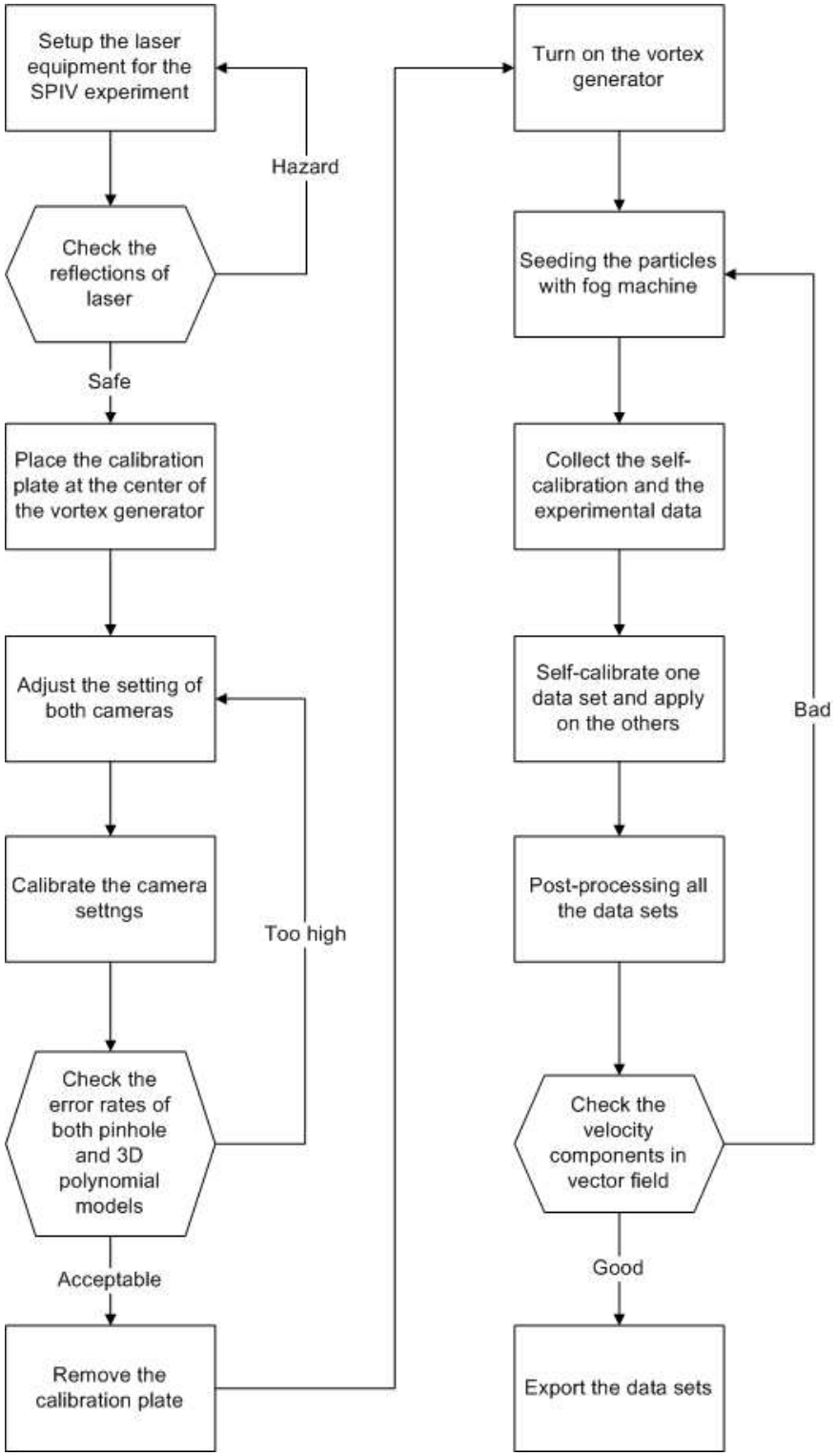

Figure 4.10: A flowchart of designing a vortex generator.

Figure 4.11 shows the SPIV experimental setup in the laboratory environment. A double pulsed laser was used to form a light sheet. The specification of the laser equipment is provided in Table 4.3. A fog machine was used to generate the seeding particles in the vortex field. It should be noted that the size of seeding particles (smoke) are around or less than 0.3 nm, which are able to follow the flow well and close. When the particles passed through the field of view on the light sheet, two cameras captured the instantaneous images. By post visualization using the software, DaVis, the flow field can be illustrated with three dimensional velocity profiles.

Figure 4.11: A setup view of SPIV experiment.

Table 4.3: Information of the laser equipment.

Model of laser	**NEW WAVE Solo III -15**
Wavelength (nm)	532
Beam diameter at $1/e^2$ pts (mm)	4
Beam divergence Φ_o (mrad)	<0.4
Pulse energy Q_o (joules/pulse)	0.05
Pulse repetition F (Hz)	15
Power ϕ_o=$Q_o\times$ F (Watts/pulse)	0.75

Figure 4.12 shows a visible dust devil created using the modified vortex generator. As shown in the picture, the dry ice is raised on the test table used in the SPIV measurement.

Figure 4.12: Simulated dust devil with dry ice.

The experiments were taken at the volume flow rate between 0.25 $m^3\ s^{-1}$ and 0.75 $m^3\ s^{-1}$ with both the outflow diameter of 450 mm and 240 mm. It should be noted that the system can create a maximum flow rate of up to 0.75 $m^3\ s^{-1}$, despite the fan blade being capable to produce the maximum volume flow rate of 0.94 $m^3\ s^{-1}$. This is because the flow is recirculated in the vortex generator, causing an energy loss by re-directing the flow. However, the efficiency of the fan blade is 80%, which is an acceptable value.

Figures 4.13, 4.14, 4.15, and 4.16 illustrate the average contour views of total, radial, vertical, and tangential velocities, respectively. The images are taken from the case using the outflow diameter of 240 mm with the maximum volume flow rate of 0.62 $m^3\ s^{-1}$. Each image consists of eight sub-images of the flow contour because the

maximum field of view in the SPIV measurement is about 130 mm by 100 mm. The results show a small amount of velocity jump at the overlap area. This is acceptable using this measurement technique. In practice, the results show a good agreement on the axisymmetric behavior of dust devil when taking the results and averaging in time. Noise appears at the height between 150 mm and 200 mm on each velocity profile. It was caused by the optical blockage from the metallic frame. The center of dust devil is offset by 20 mm. This phenomenom is caused by the restriction ring which has an offset value of 20 mm at the outflow region.

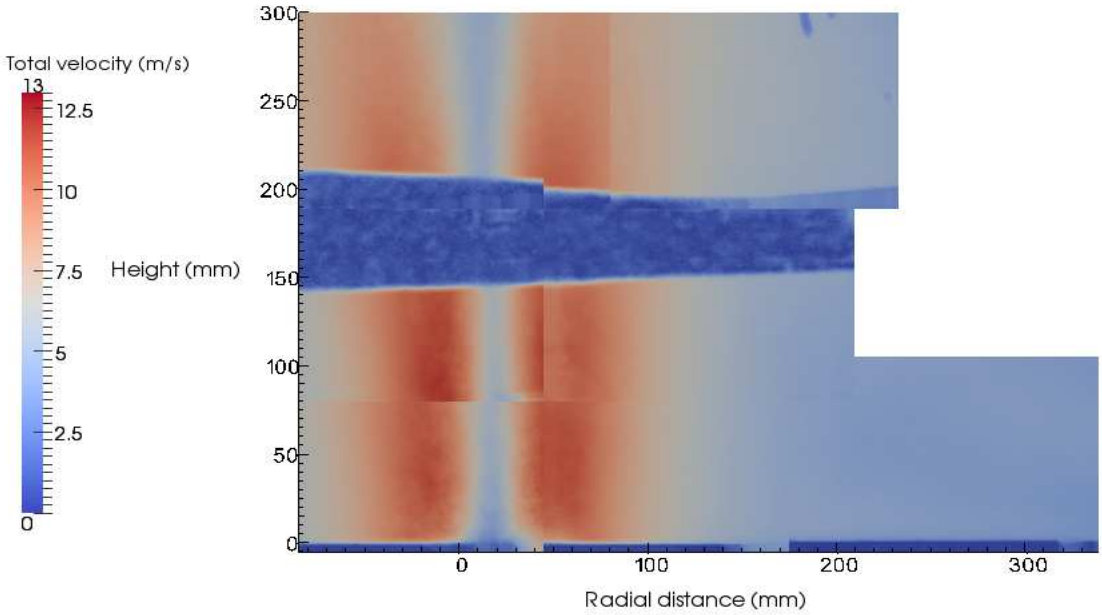

Figure 4.13: A contour view of mean total velocity in the SPIV experiment.

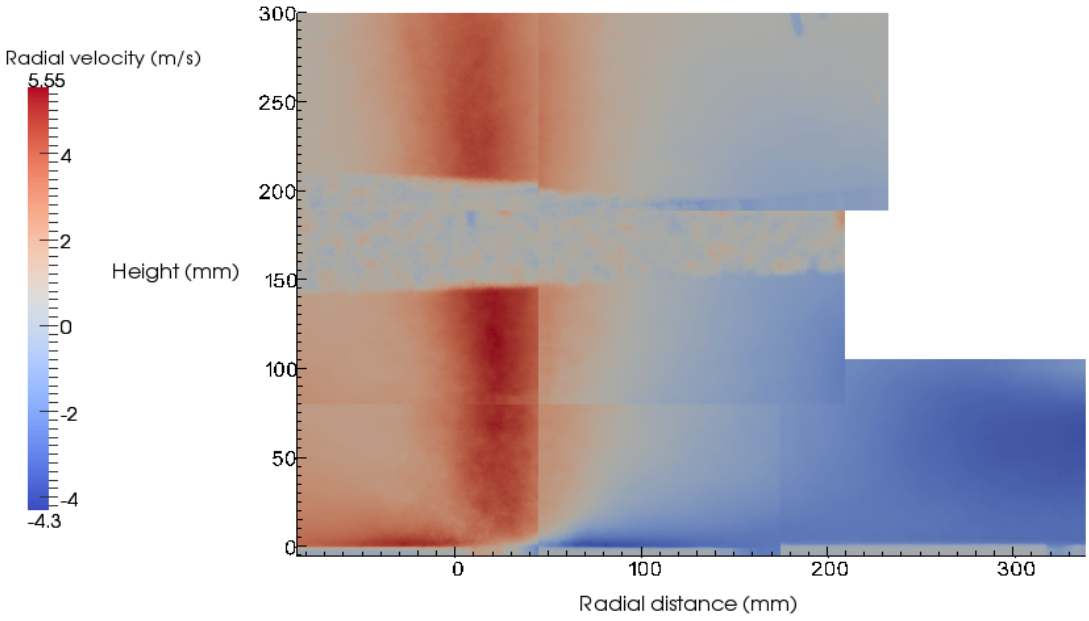

Figure 4.14: A contour view of mean radial velocity in the SPIV experiment.

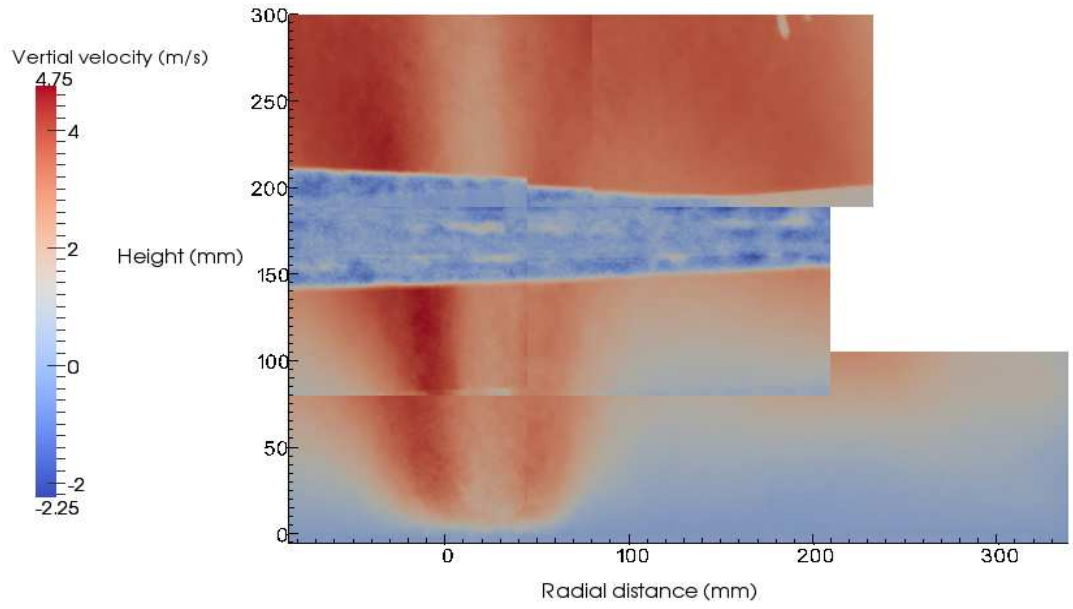

Figure 4.15: A contour view of mean vertical velocity in the SPIV experiment.

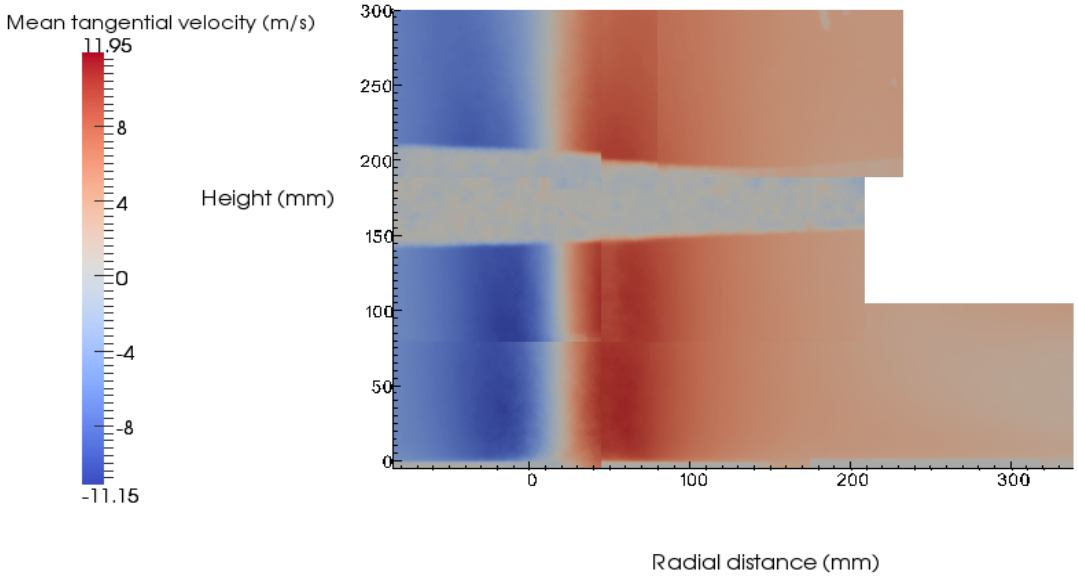

Figure 4.16: A contour view of mean tangential velocity in the SPIV experiment.

4.3 Numerical Validation for Flow Field

Since the vortex generator configuration was slightly changed during the construction, the velocity profiles did not fit well with the sensitivity studies. This is mainly due to the honeycomb feature that was removed in order to produce a better flow field in the corner region. To validate the numerical setup with the experimental velocity field of dust devils, the simulations were set to be the same as the experimental configuration. This allows for proper comparison between experimental and numerical results.

4.3.1 Setup for the Numerical Simulations

Figure 4.17 shows a three dimensional numerical model which is used for validation with both the flow field and water vapour transport experiments in Chapter 5. The top part is a vortex generator domain, which is same as the one used in the sensitivity

study, as shown in Figure 4.3, but without the numerical honeycomb effect. The middle part is an open area which represented the region between water tank and vortex generator. The rectangular shape was adapted to cover the area above the water tank. However, the shape of this section does not have strong influence on the vortex region. Both the top and the middle domains are simulated as the fluid regions (air). The bottom part represents the porous medium, which corresponds to the foam in the water vapour transport experiments. More details will be described in Chapter 5. It should be noted that the porous medium in the numerical model and the foams in the experiment are used to represent the regolith on both Earth and Mars.

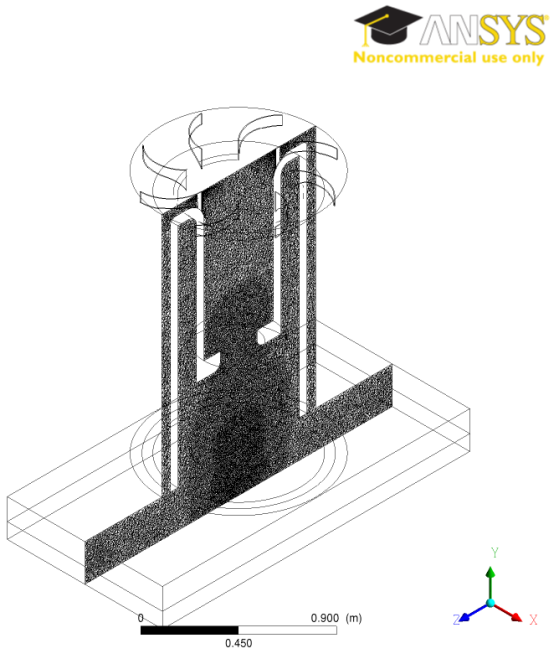

Figure 4.17: A three-dimensional numerical model setup and the use of typical mesh at the YZ plane.

An unstructured tetrahedral grid is applied to the entire model. The inflation layers are not applied at the interface between the fluid and porous domains. It is known that the inflation layers may result better solution in the flow field. However, some error at the interface may be present in the numerical solver code. Prieto [2006] also

indicated this problem in his study. As a result, the Courant number may increase rapidly at the interface outside of the vortex region if mesh inflation is used. Several attempts, such as the change of turbulence model (RSM-SSG to k-ε), the change of the scheme, and the reduction of timestep, etc. did not overcome this issue. The best solution to avoid this possible error was to use the mesh with the tetrahedral elements, i.e. without mesh inflation.

The geometric dimensions of the top part can be referred to Table 4.1. The middle and bottom parts have the same surface size of 2 m $\times$ 1 m with the different height/thickness of 15 cm and 10 cm, respectively. The boundary conditions of the middle part is set to be free-slip wall, since it is assumed to be no flow passing through the boundaries. The porous media has the porosity of 0.97 and the saturated permeability of 2.22×10^{-9} [Prieto, 2006]. The boundary condition at the tank walls is set to be no-slip wall.

Transient simulations are resolved with a second order backward Euler discretization scheme and a high resolution scheme for the transient terms and advection terms, respectively. The adaptive timestep between 0.00075 and 0.005 s was selected to keep Courant number low in the CFX-solver. Basically, the timestep would be depended on the Courant number of the previous timestep. The timestep used has to be very small, because of the RSM-SSG turbulence model was chosen in both the porous medium and fluid domains. As a result, the computational efficiency decreased when simulating this complex flow field. The atmospheric conditions were set to an isothermal, incompressible, and Newtonian fluid of air. The dry blub temperature of 21.2 ^{o}C was used from the average room temperature in the experiments. The air density (ρ_a) is 1.204 kg m^{-3} and the air dynamic viscosity is 1.825e-5 kg m/s [Çengel, 2002]. Convergence criteria required the value of residual RMS to be less than 10^{-4}. The Reynolds Stress Model (RSM-SSG) turbulence model was also employed.

4.3.2 Flow Field Validation

Figure 4.18 illustrates the streamlines in the fluid domain. It provides significant information about how the flow converged to the core region. A few streamlines outside the vortex generator indicated that the flow was not completely recirculated. However, their speeds were very slow, which means there was almost no flow across the open boundaries. This agrees with the assumption made in the sensitivity and flow validation studies. Figure 4.19 illustrates the velocity vectors within the core and corner regions. From the velocity vectors, it is apparent that the flow was going slightly in and out across the interface between the porous media and fluid domain. This is an evidence that a dust devil may cause the occurrence of advection flux within the porous medium, as explained in Section 3.2.2.

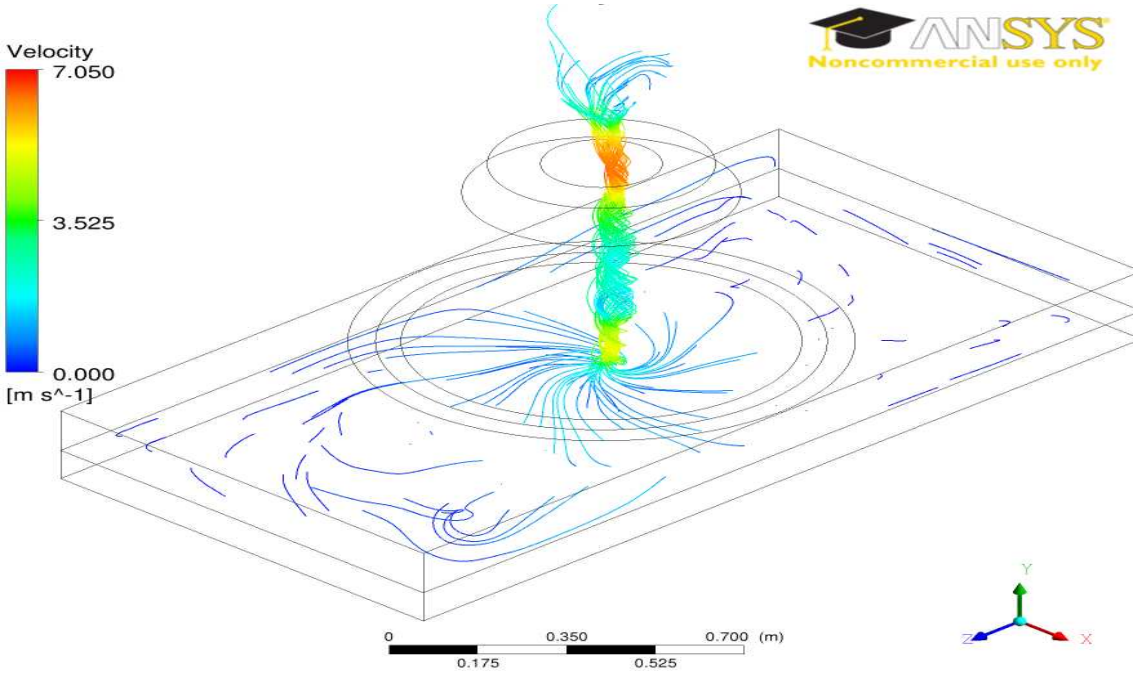

Figure 4.18: A 3-dimensional view of streamlines in the numerical model.

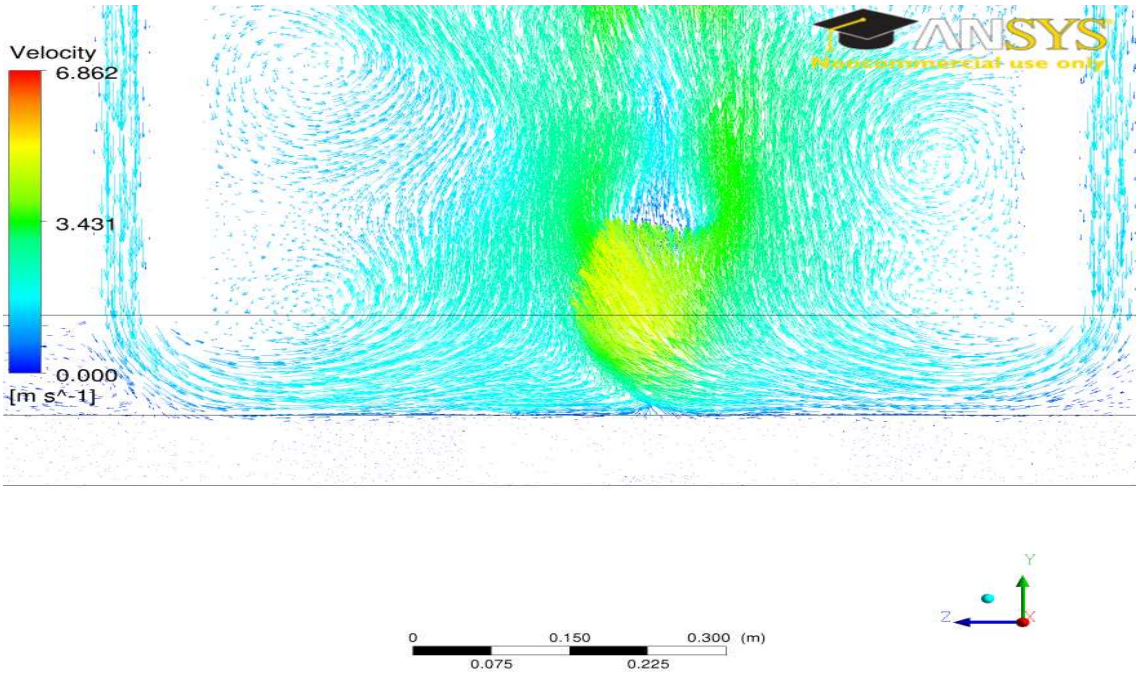

Figure 4.19: Velocity vectors within the core and corner regions.

Figure 4.20 shows that the mean maximum tangential velocity has a linear relationship with the volume flow rate. When the volume flow rate through the outflow region increases, the difference of mean maximum tangential velocity between two different outflow diameters increases. This does not agree with the sensitivity studies. However, it may be caused by the absence of the honeycomb feature, which would reduce the tangential velocity and increase the core radius. The result of mean core radii is shown in Figure 4.21. Both average quantities show excellent agreement between the numerical estimates and the SPIV measurements, validating the vortex flow structure of the numerical model.

By comparing the non-dimensional tangential velocity profiles between the simulation and experimental results, as shown in Figure 4.22, it indicates that the numerical RSM-SSG turbulence modeling can be used to produce a similar flow field. The good agreement between the flow profiles provides further validation of the numerical model, this time with respect to the detailed flow field within the vortex.

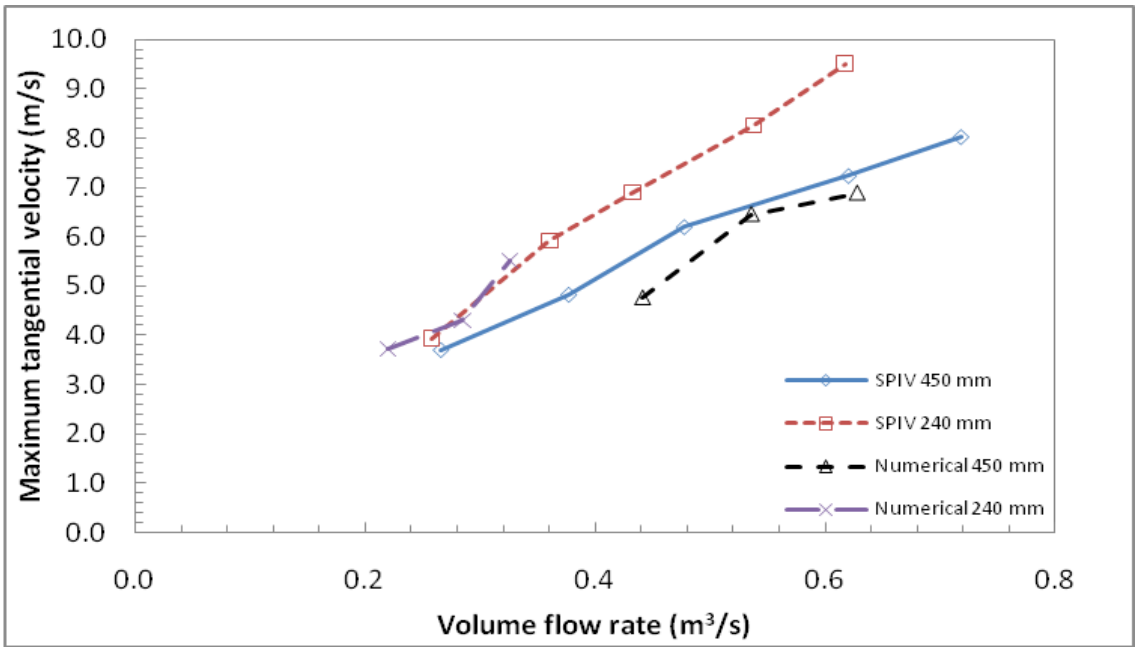

Figure 4.20: Mean maximum tangential velocity as a function of volume flow rate.

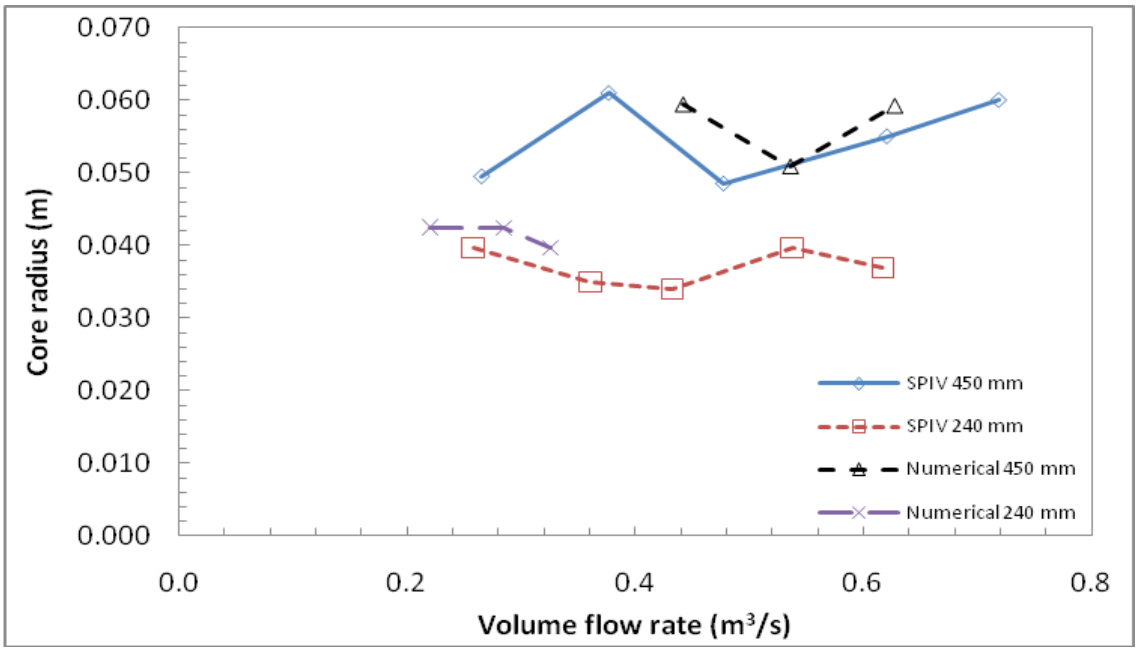

Figure 4.21: Mean core radius as a function of volume flow rate.

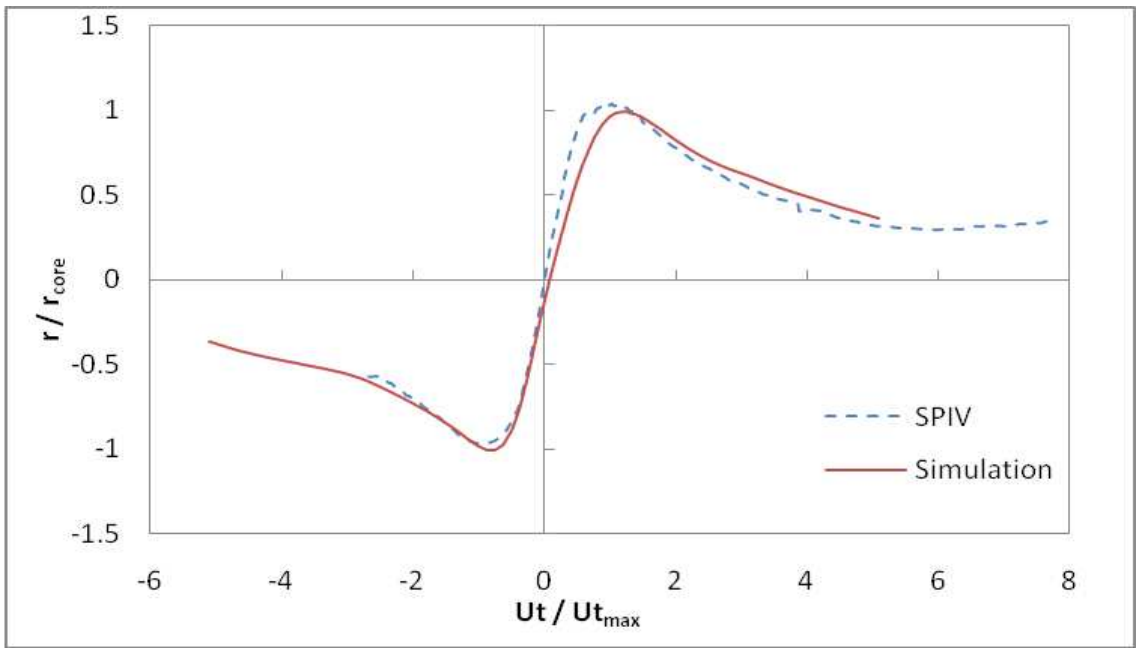

Figure 4.22: Tangential velocity comparison between the experiment and simulation at the elevation of 0.06 m.

Swirl ratios calculated in different methods are shown in Figure 4.23 and 4.24. The relationship between the outflow diameter and swirl ratios is consistent with the sensitivity study and again shows good agreement. The small variation shown in all cases implies that the swirl ratio is independent of the volume flow rate. In contrast with the sensitivity study, which included a honeycomb, this time both definitions of swirl ratio show an increased value with a reduction of the outflow radius, as expected.

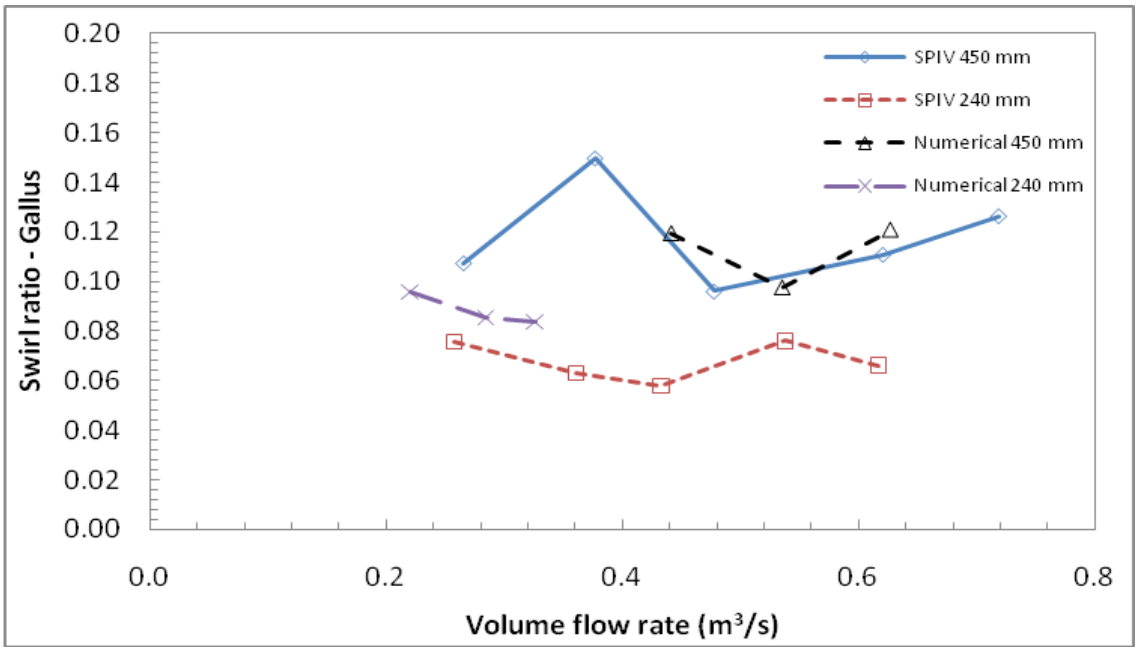

Figure 4.23: Swirl ratio using Gallus definition as a function of volume flow rate.

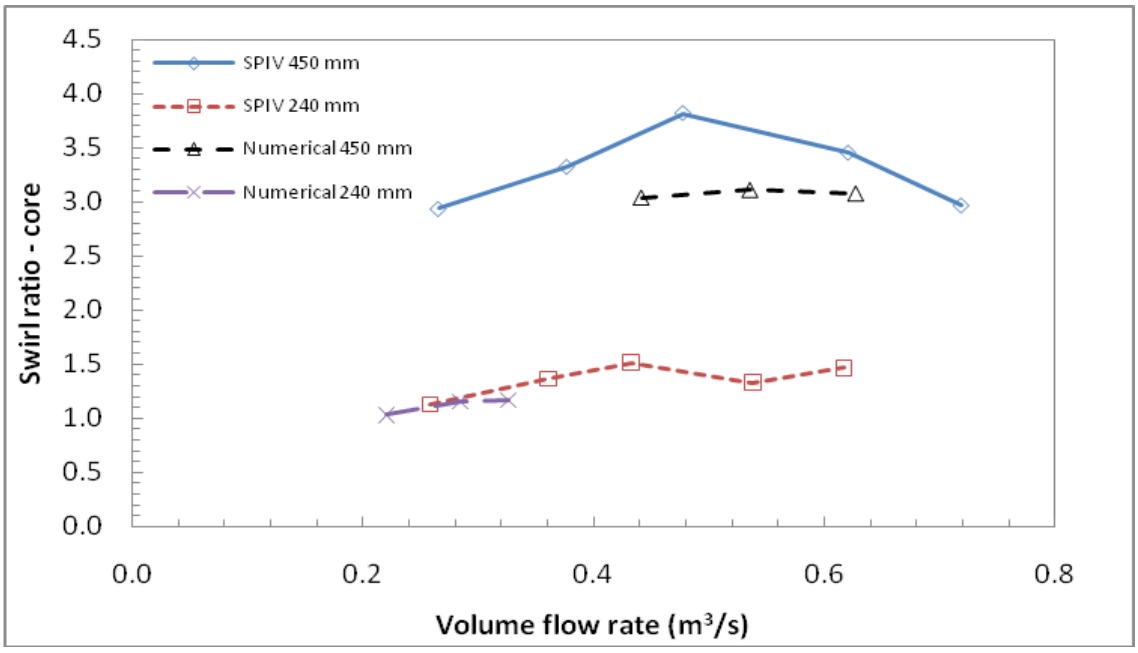

Figure 4.24: Swirl ratio within vortex core as a function of volume flow rate.

Figure 4.25 shows that the aspect ratio also depends on the outflow diameter. This is another obvious result, which was not shown clearly in the sensitivity study. As a result, the outflow diameter can help define the geometry of dust devils. Again good agreement is found between the numerical and the experimental data.

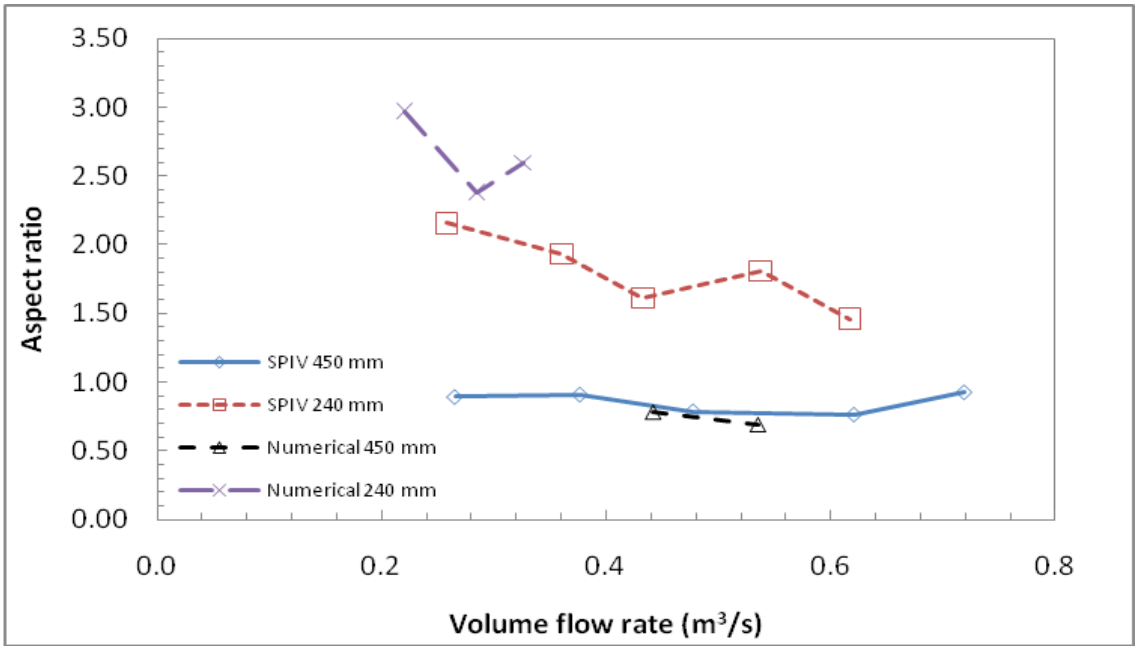

Figure 4.25: Aspect ratio as a function of volume flow rate.

From the previous results, the change of volume flow rate may not influence directly the swirl ratios or the aspect ratio. In contrast with these parameters, the radial Reynolds number seems to be mainly a function of the volume flow rate, as shown in Figure 4.26. This information will be particularly useful for the water vapour transport analysis.

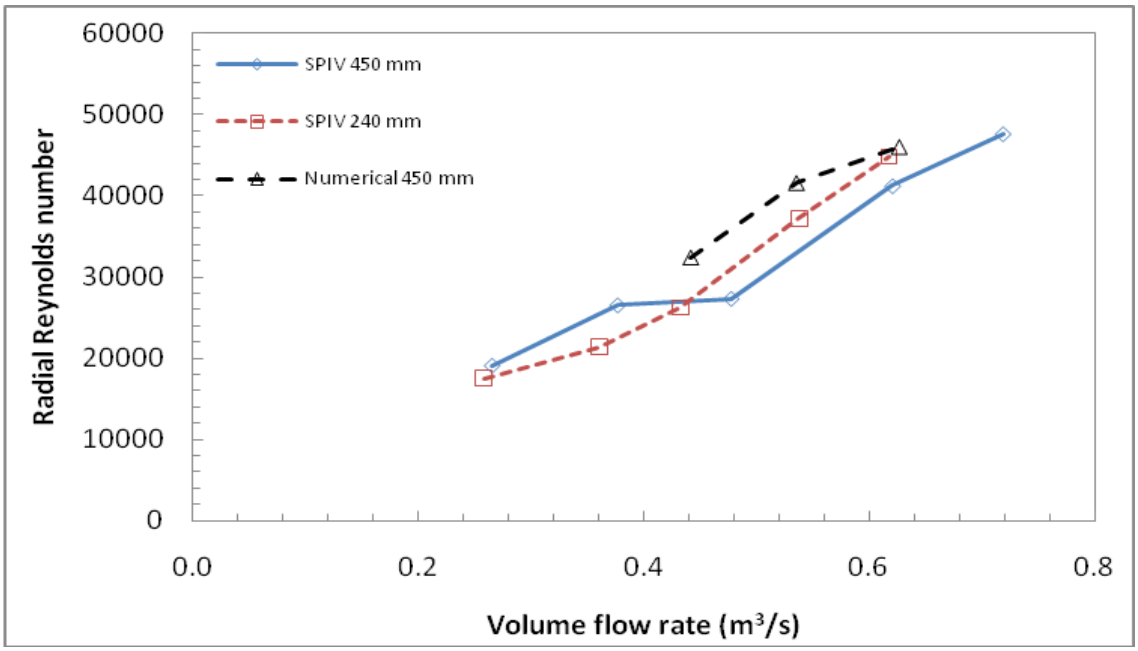

Figure 4.26: Radial Reynolds number as a function of volume flow rate.

Chapter 5

Water Vapour Transport

From the previous chapter, it is known that the modified vortex generator can reproduce the flow characteristics of real dust devils. This chapter will focus on water vapour transport mechanisms due to the natural and forced evaporation. In order to trust the simulation of water vapour transport with a dust devil on Mars, the numerical model should be first partially validated. The validation procedures were not complete, because they were subject to only Earth ambient conditions. First, an experiment setup was designed to study the effect of dust devils on the water vapour transport. It was obtained using a water tank, a weight scale, many digital humidity and temperature sensors, and the vortex generator described earlier. A numerical model was then set to the same conditions as the experimental setup. The results of the flow field in the numerical simulation agreed with the experiments, despite the laboratory conditions being somewhat unsteady during the experiment. Finally, the numerical model was adapted to use Martian conditions and the effect of dust devil on Mars was estimated. The goal of this numerical study is to predict how much water vapour transport rate may be enhanced by a dust devil.

5.1 Experimental Setup of Water Evaporation

Figure 5.1 shows the experimental setup for the mass transport study. Sensiron solid-state humidity/temperature (SHT71) sensors were used to measure the humidity and temperature at three layers within the porous foams in the experiments. The work of calibration for the humidity and temperature sensors was done together with Farahaninia [2008]. The calibration data can be also found there. A total of 120 sensors were placed at three surface layers. Each layer has 40 sensors and the layout is shown in Figure 5.2. To record the relative humidity (RH) and temperature data, an in-house data acquisition system was used. The system requires about 38 s to record all 128 sensors. A weight scale was placed centered under the water tank to measure the amount of water loss. The water tank was levelled horizontally and was filled with distilled water. The water level was slightly lower than the bottom surface of the foam, because the sensors can not be immersed in the water and the foam is also to remain dry.

5.2 Experimental Results of Water Evaporation

The first part of the experiments was performed at room conditions (no wind) after filling the amount of water (around 20 kg) into the reservoir. Figure 5.3 shows that the room temperature changed slightly in a one day cycle. The locations of sensors "Room A" and "Room B" were at two opposite corners in the laboratory. The other four out-of-foam sensors were located at different levels of the vortex center (the center of the horizontal foam surface). The room temperature could be considered as isothermal, since the temperature variation was around one degree within a day. The bottom foam temperature was decreasing at the beginning due to the evaporation cooling, since the evaporation is an endothermic process. The middle foam temperature always increased significantly before reaching the steady state. During this short period of time, the foam absorbed water vapour from the water source, which released heat

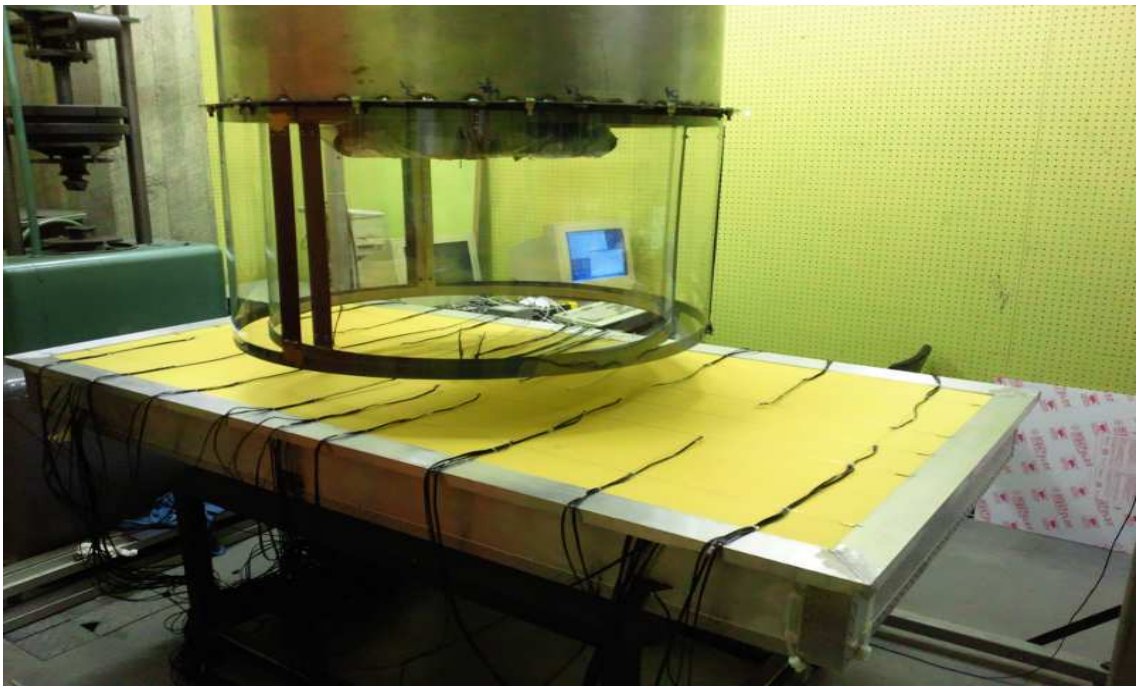

Figure 5.1: The experimental setup of water vapour transport study.

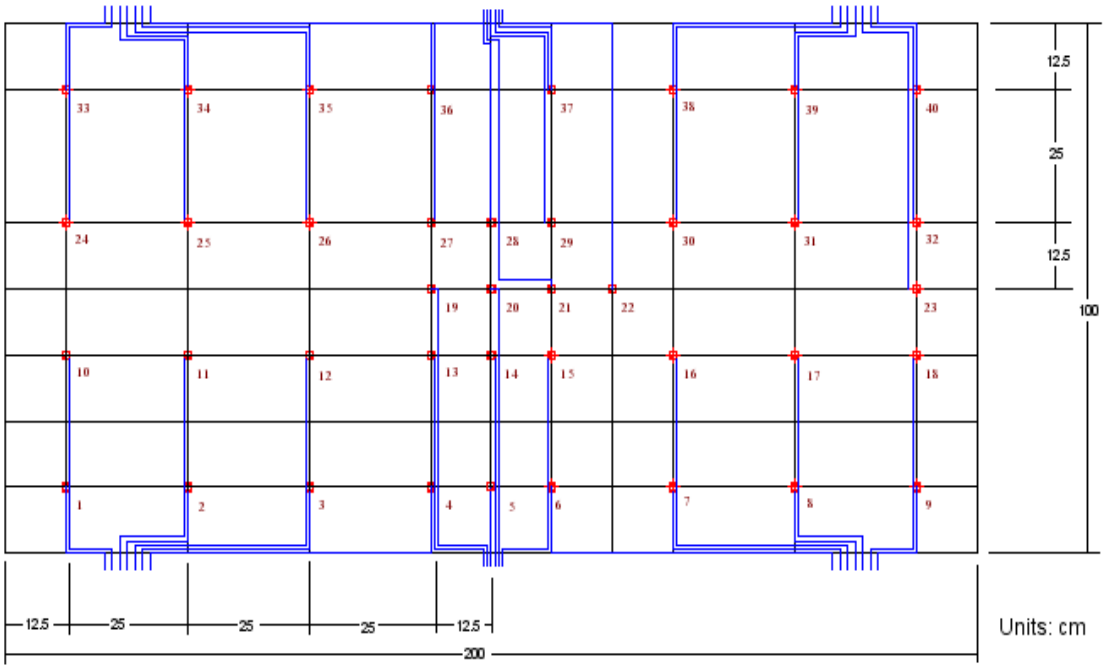

Figure 5.2: An example layout of sensor path.

because absorption is an exothermic process. The temperature started to decrease when the foam was saturated, which may be seen in the humidity profiles, shown in Figure 5.4. The humidity profile of the top foam surface was constantly fluctuating within a range of 1 g m^{-3}. A reasonable explanation for this fluctuation was that the sensors located at the top foam surface were offset a very small amount of distance above the foam due to the weight of foams.

From this experiment, we can assume that the steady state condition has been reached at 30,000 s (≈8 hours). This experiment was repeated 3 times to ensure a better mean value. After the steady state condition was reached, the water evaporation rate was calculated to be 3.26E-6 kg s^{-1}. The results agree well with the Prieto [2006] study. This still air case will be used as a basis for comparison with the vortex cases.

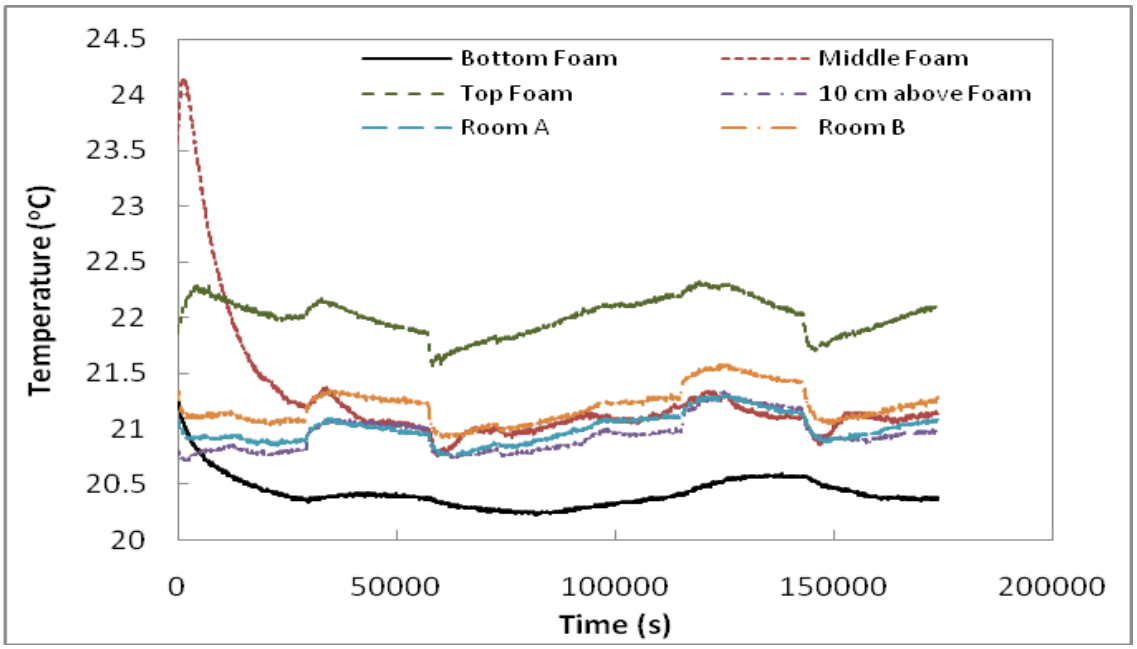

Figure 5.3: Temperature profiles as a function of time in laboratory environment.

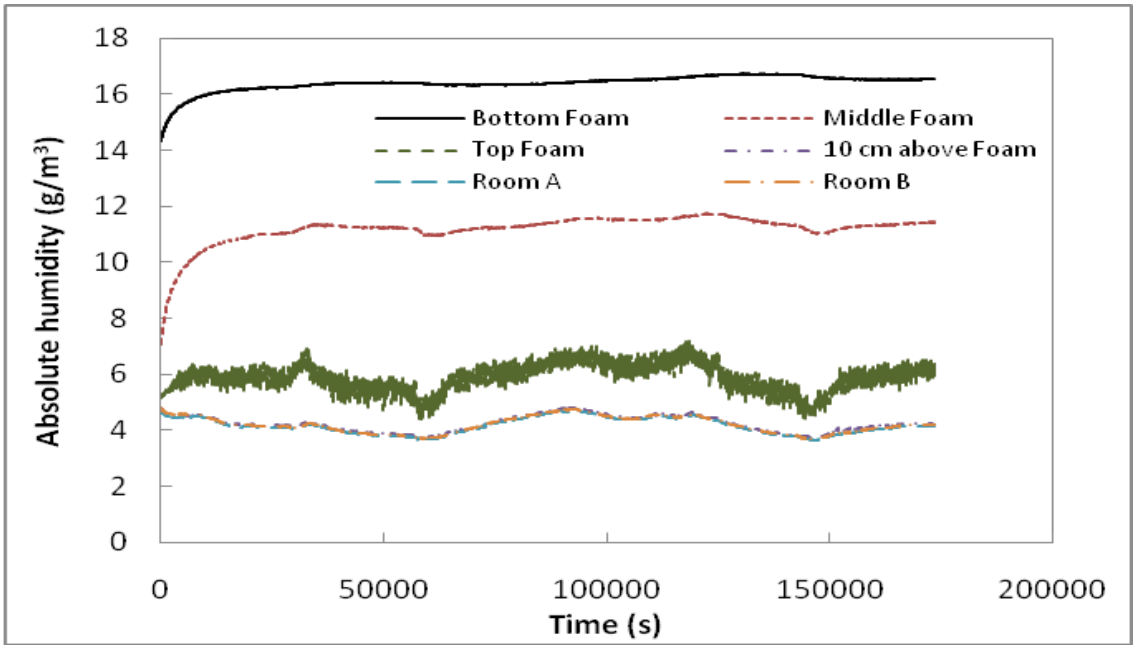

Figure 5.4: Absolute humidity profiles as a function of time in laboratory environment.

The second part of experiments was to study the influence between turbulent vortex flows and the water evaporation rate. The water tank set-up was the same as the case of still air. Each experiment was delayed for at least 30,000 s after the last one. The purpose was to reach the steady state conditions and to wait for the foam to be fully saturated again. The vortex generator was operated within the rotation speed of 1725 RPM due to safety issues. Five different strengths of updraft volume flow rates through the fan were conducted.

From Figure 5.5 to 5.14, the temperature and humidity profiles presented similar behavior with the various volume flow rates. A lower strength of updraft volume flow rate would result in longer time to reach the steady state condition without adding relevant data. In general, the evaporation rate with the presence of laboratory dust devils can be calculated at 6,000 s after starting the vortex generator.

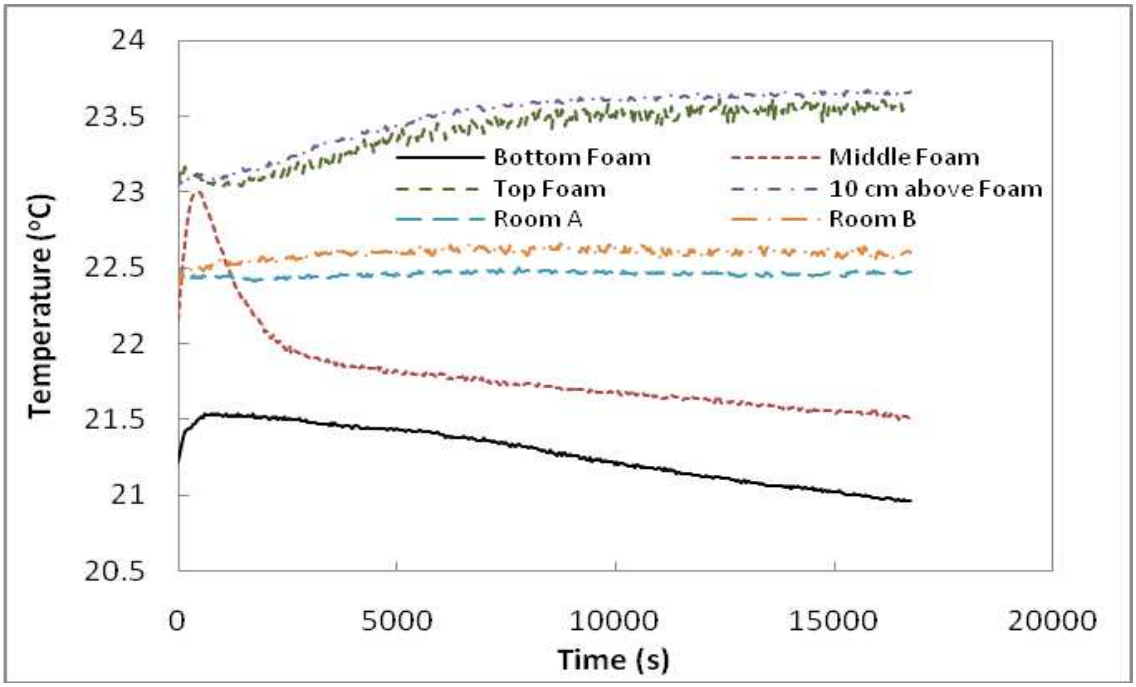

Figure 5.5: Temperature profiles as a function of time with Q=0.26 m^3 s^{-1}.

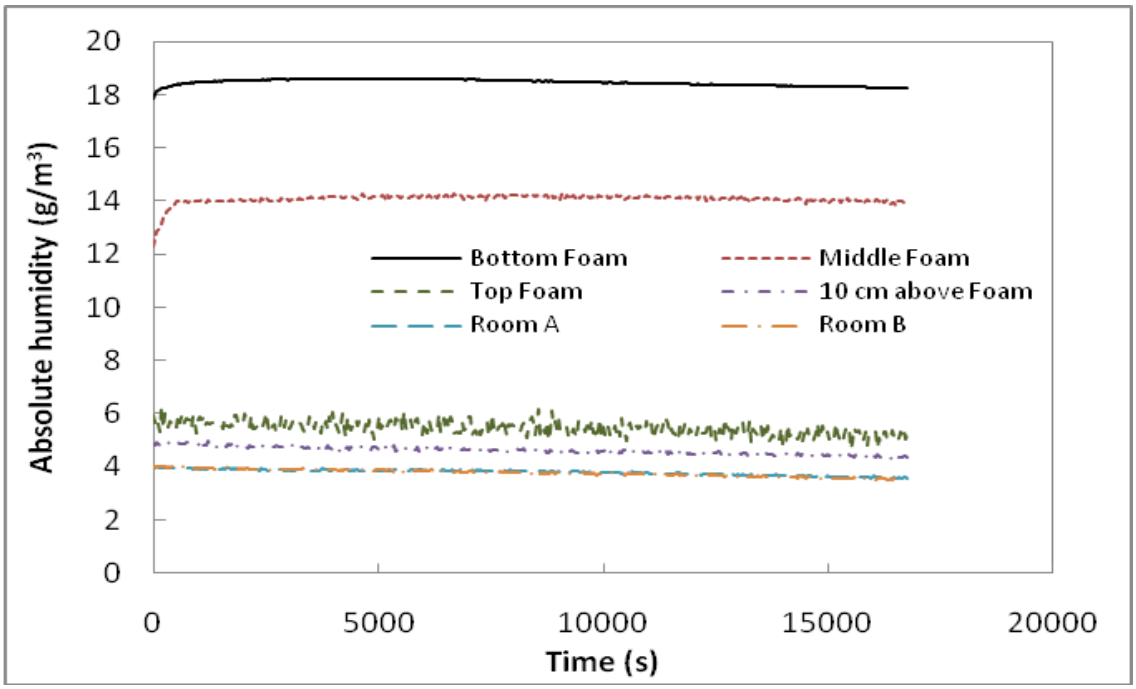

Figure 5.6: Absolute humidity profiles as a function of time with Q=0.26 m^3 s^{-1}.

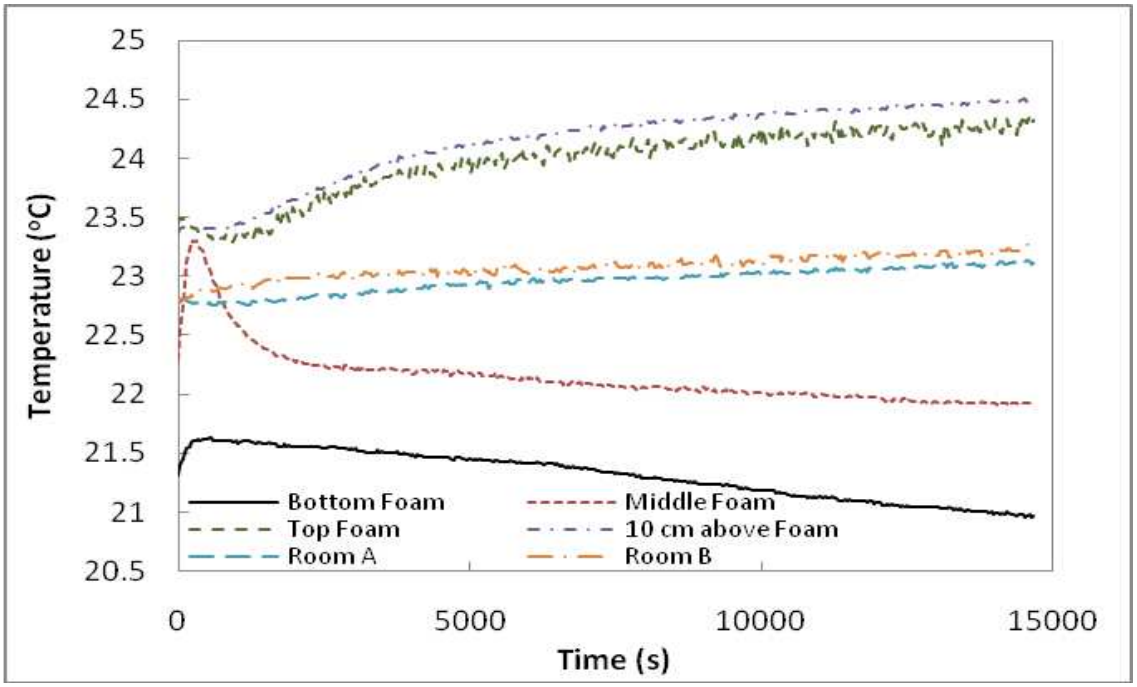

Figure 5.7: Temperature profiles as a function of time with Q=0.36 m^3 s^{-1}.

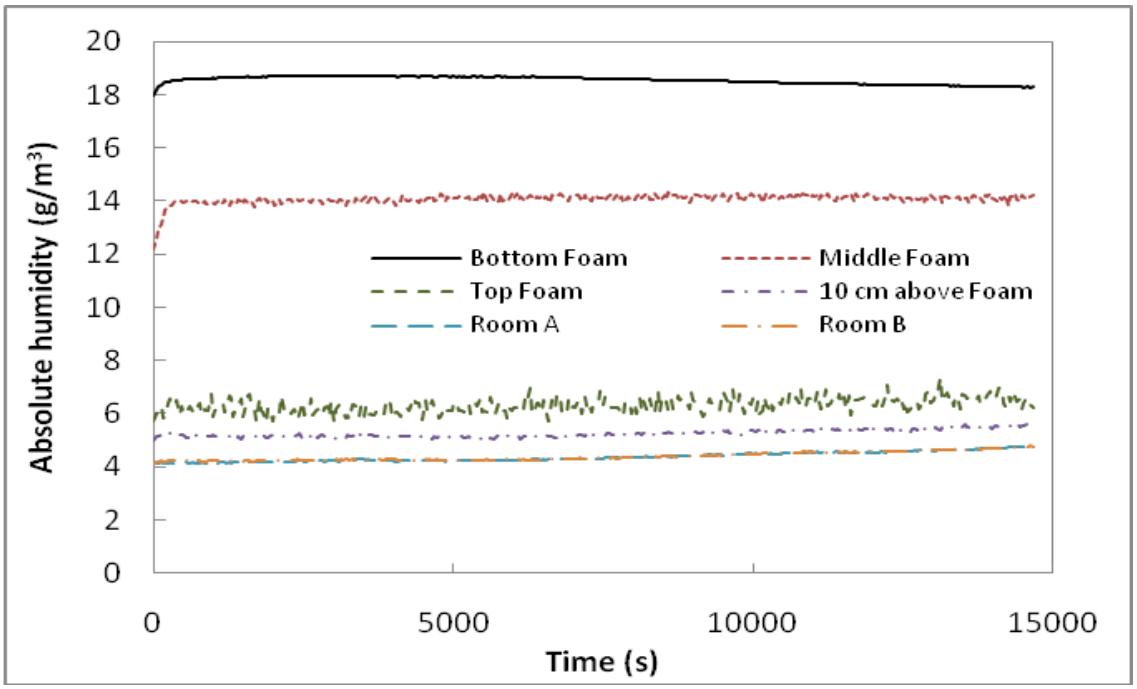

Figure 5.8: Absolute humidity profiles as a function of time with Q=0.36 m^3 s^{-1}.

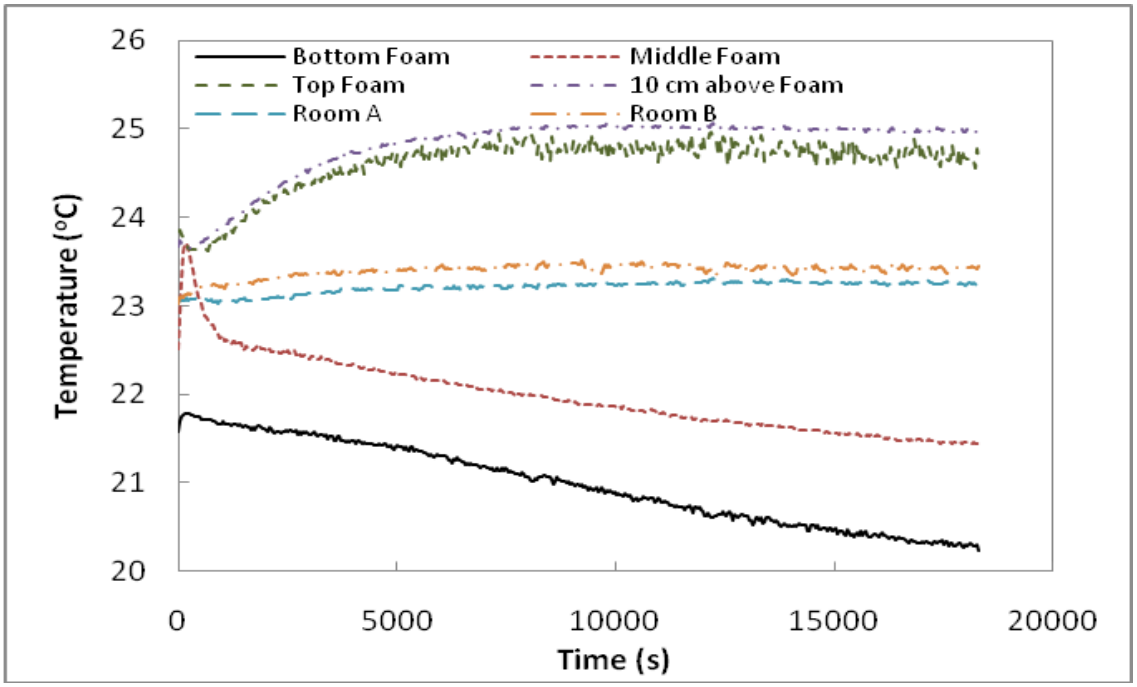

Figure 5.9: Temperature profiles as a function of time with Q=0.43 m^3 s^{-1}.

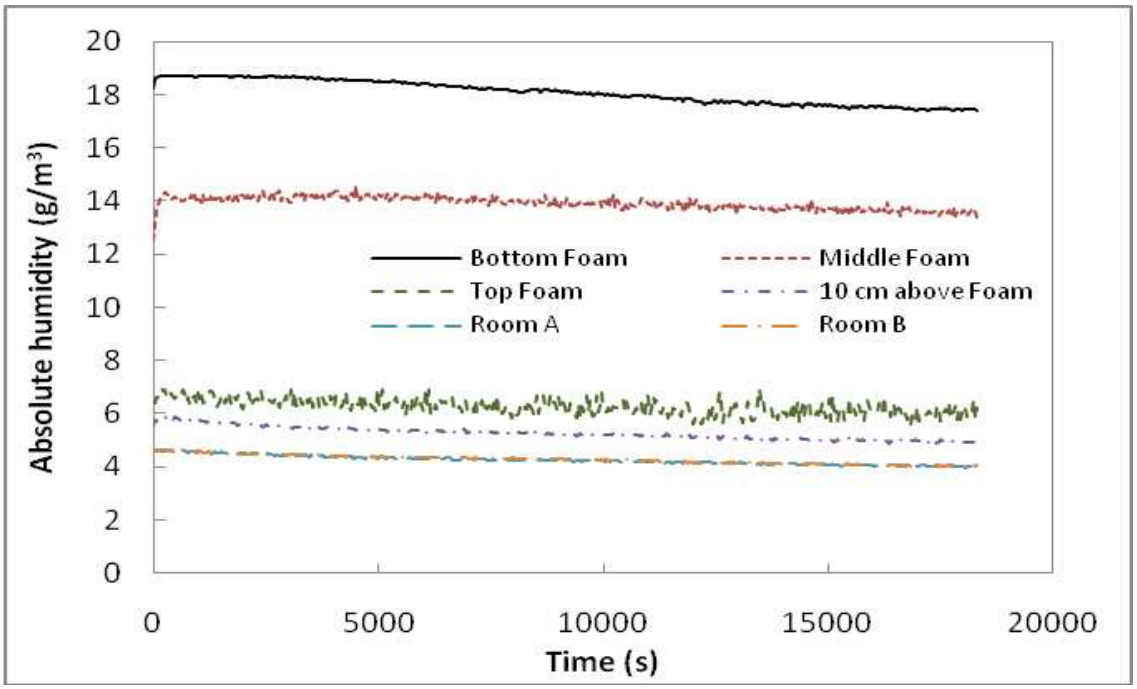

Figure 5.10: Absolute humidity profiles as a function of time with Q=0.43 m^3 s^{-1}.

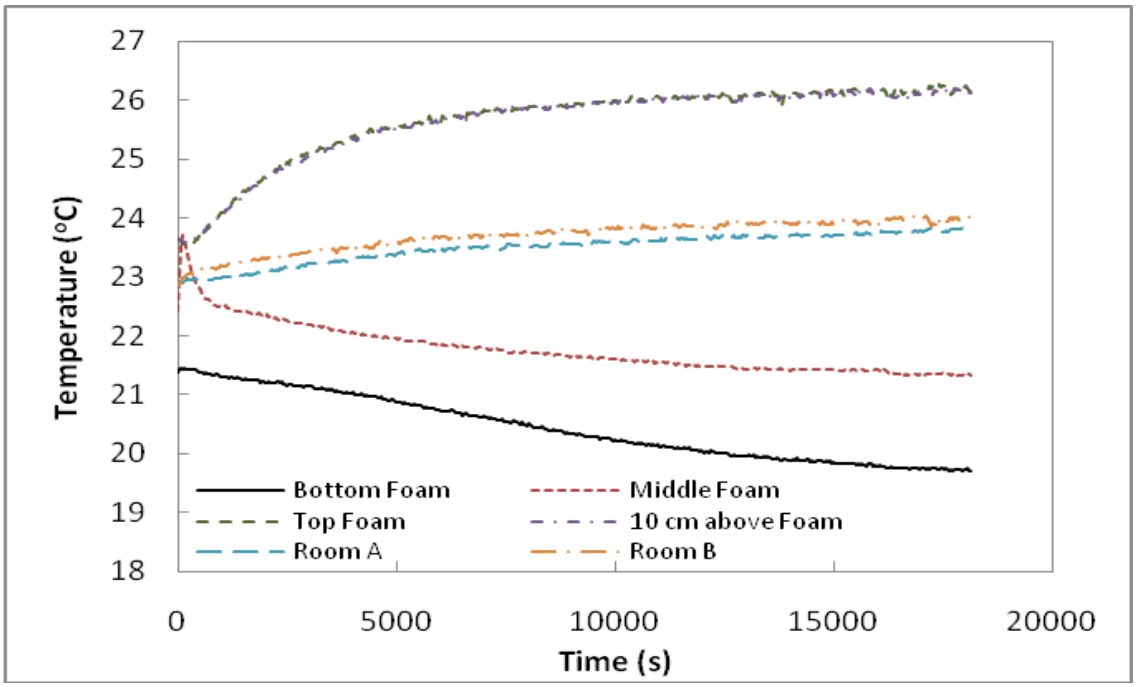

Figure 5.11: Temperature profiles as a function of time with Q=0.53 m^3 s^{-1}.

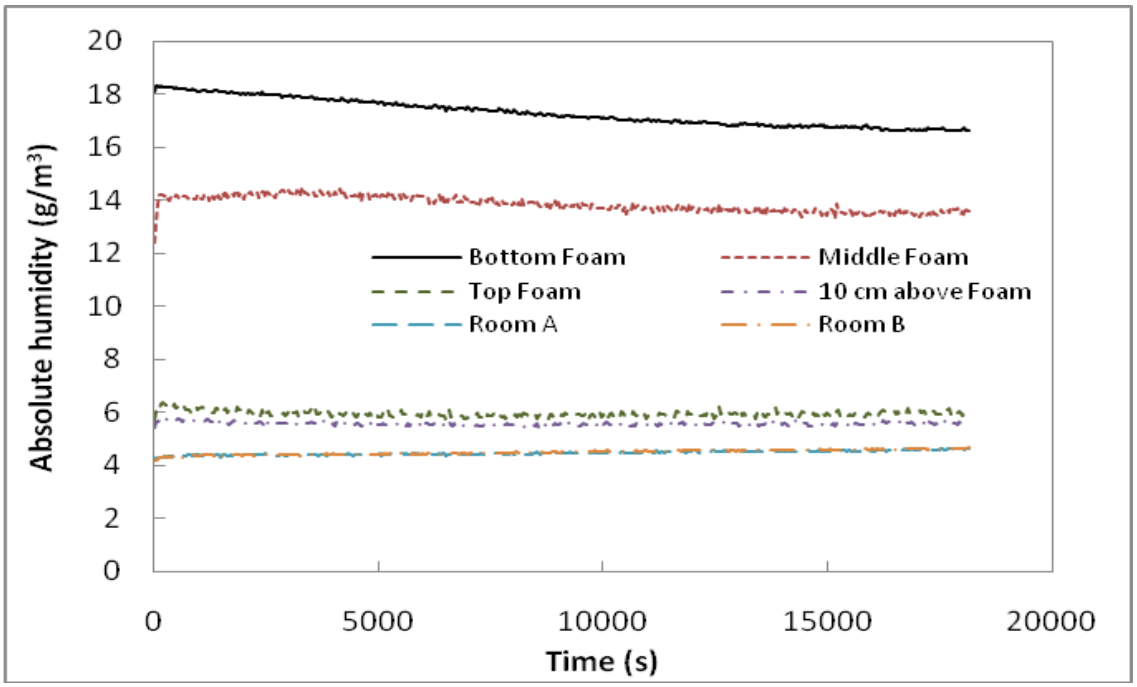

Figure 5.12: Absolute humidity profiles as a function of time with Q=0.53 m^3 s^{-1}.

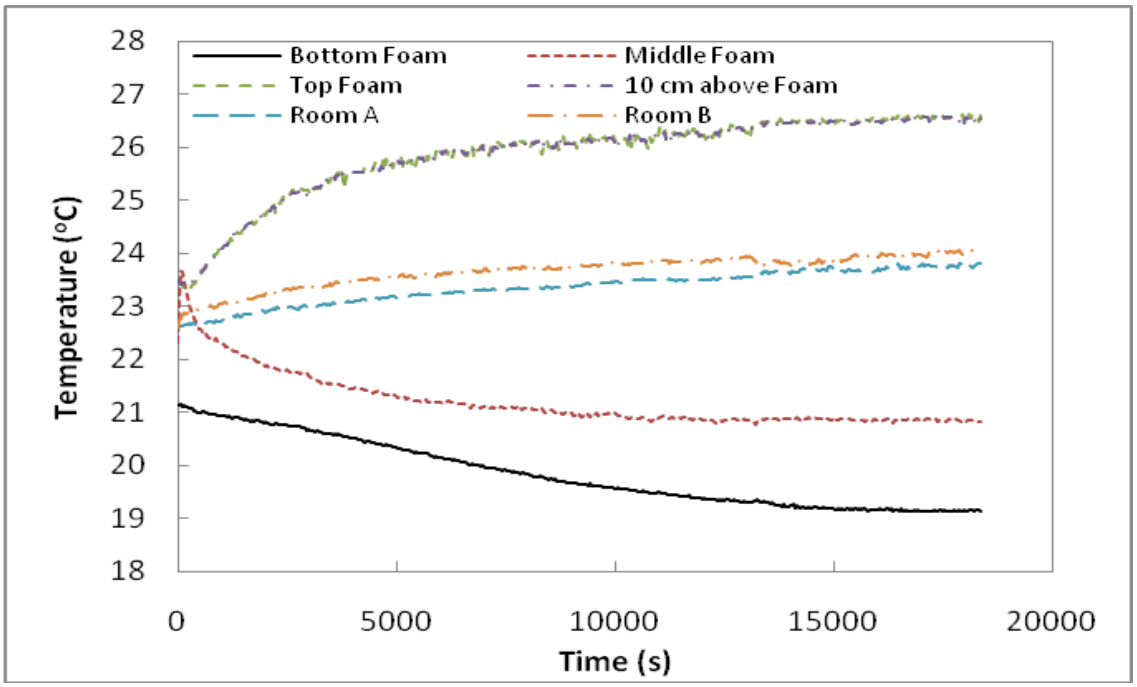

Figure 5.13: Temperature profiles as a function of time with Q=0.62 m^3 s^{-1}.

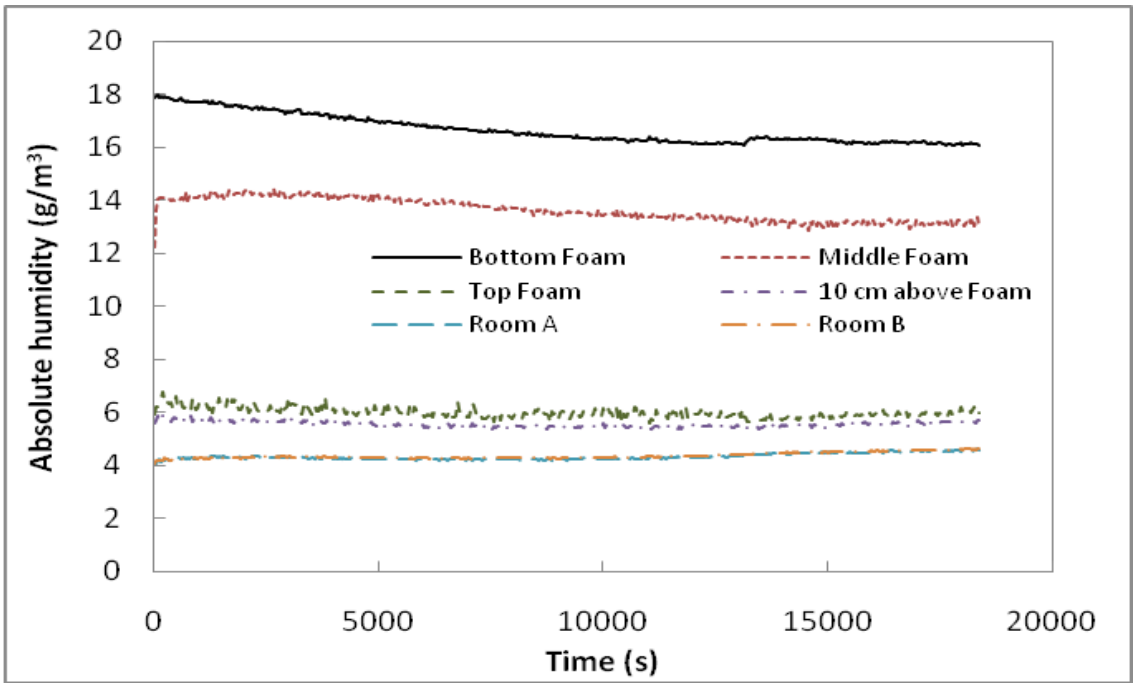

Figure 5.14: Absolute humidity profiles as a function of time with Q=0.62 m^3 s^{-1}.

A significant influence of the vortex flow on the temperature at the middle height of the foam is shown in Figure 5.15. As in the still air case, a sudden increase in the temperature at the beginning of experiment was caused by the absorption process. This description is supported by the absolute humidity profiles, shown in Figure 5.16. The temperature can be increased by up to 2 °C with the highest flow rate in the experiments. The temperature at top foam surface was increased slowly and progressively by up to 3 °C, shown in Figure 5.17. This was probably caused by both the heat of the motor and the heat dissipated from the foam from the absorption. It is believed that the heat of the motor may have more influence on the temperature, because most air was recirculated in the system and the same air was used to cool the motor.

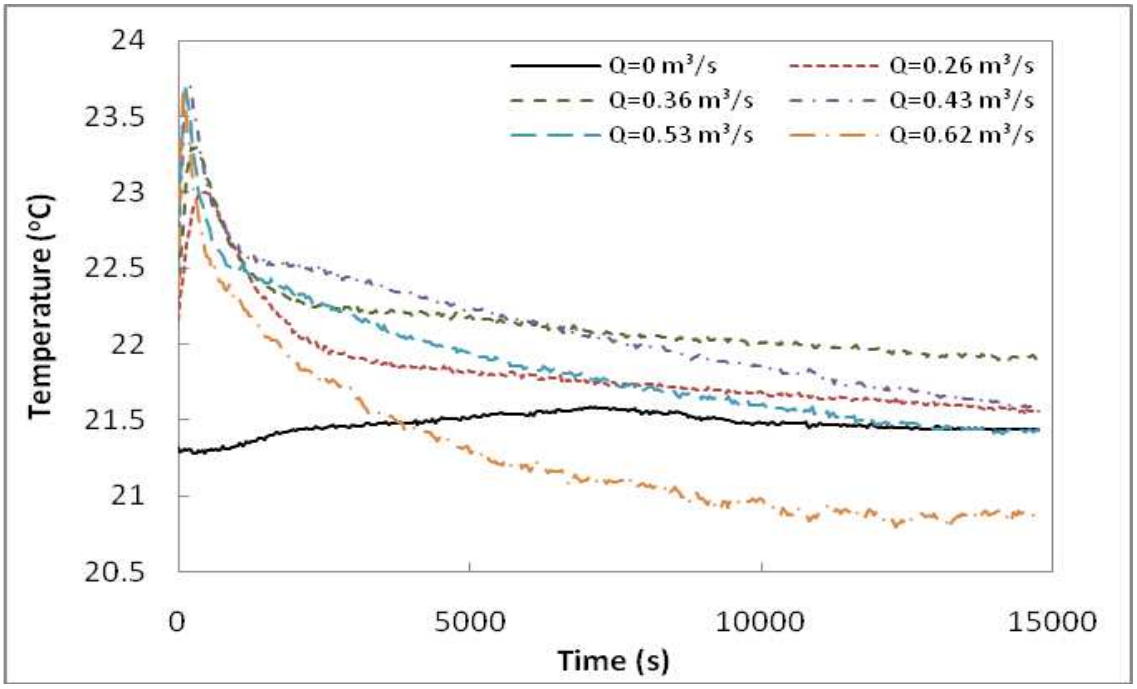

Figure 5.15: Temperature profiles at middle layer with varied flow rates.

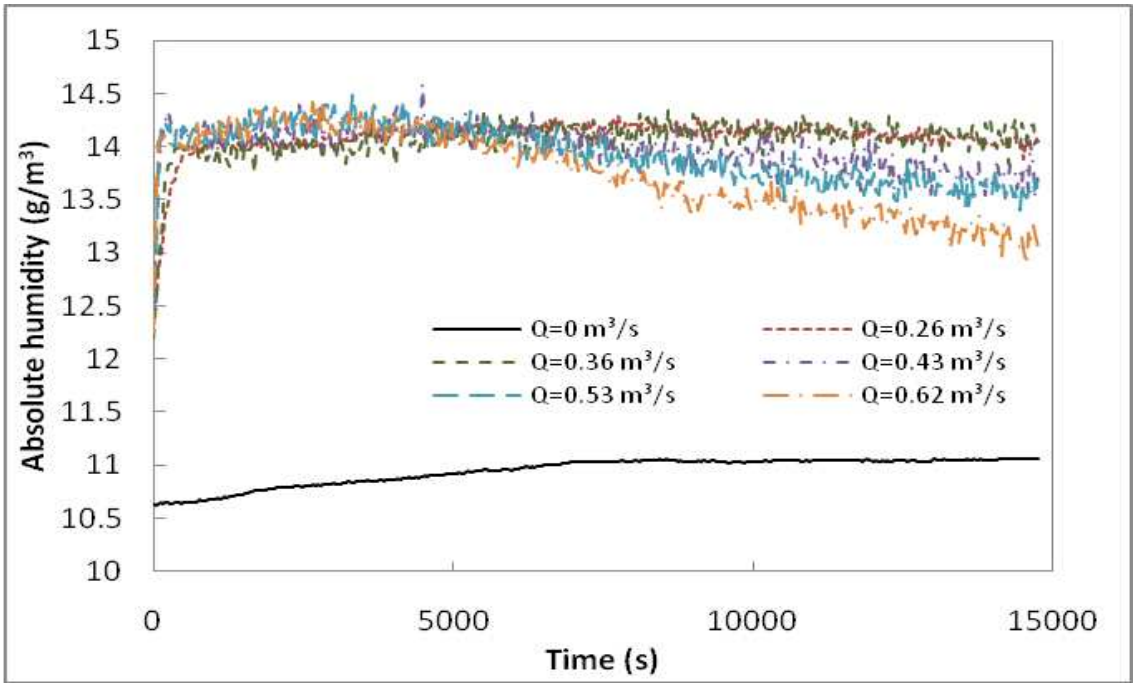

Figure 5.16: Absolute humidity profiles at middle layer with varied flow rates.

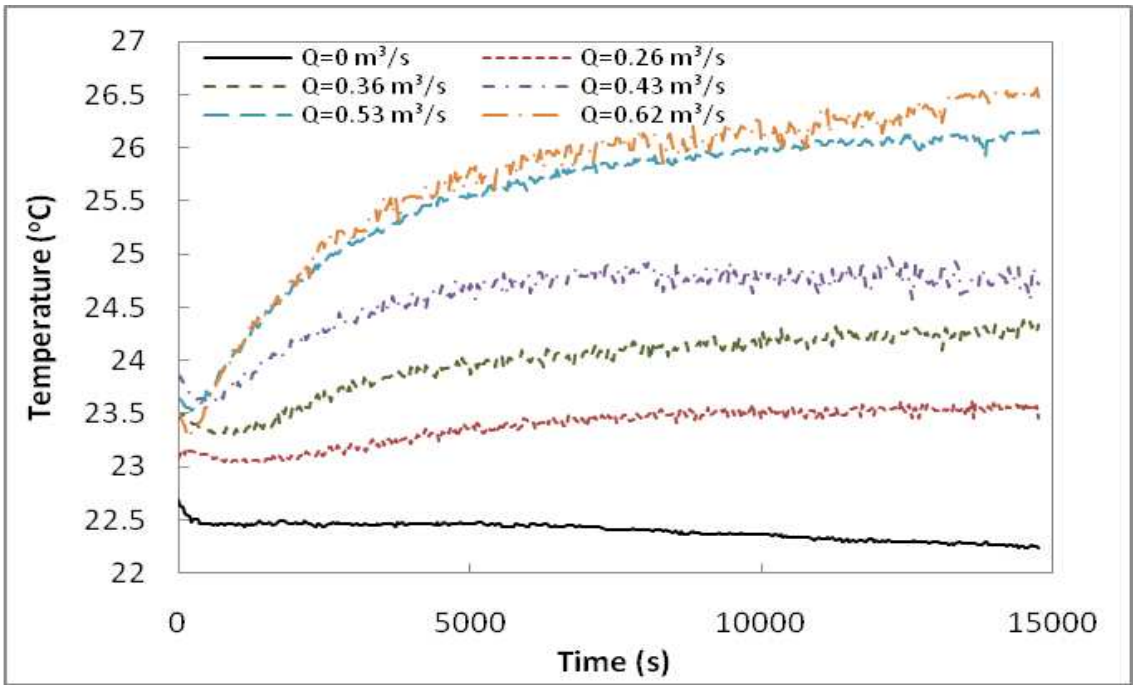

Figure 5.17: Temperature profiles at top layer with varied flow rates.

Figure 5.18 and 5.19 show the temperature and humidity profiles as a function of time at different locations from the vortex center. When water vapour concentrated toward the vortex center, because of the advection flux inside the foam, the temperature increased at the vortex center but decreased at the locations offset from the center. The demonstration shows that a higher flow rate may have a smaller concentration region. This high concentration region can also be seen when the experiments have reached the steady state condition, as shown in the contour plots in Figure 5.20 and 5.21.

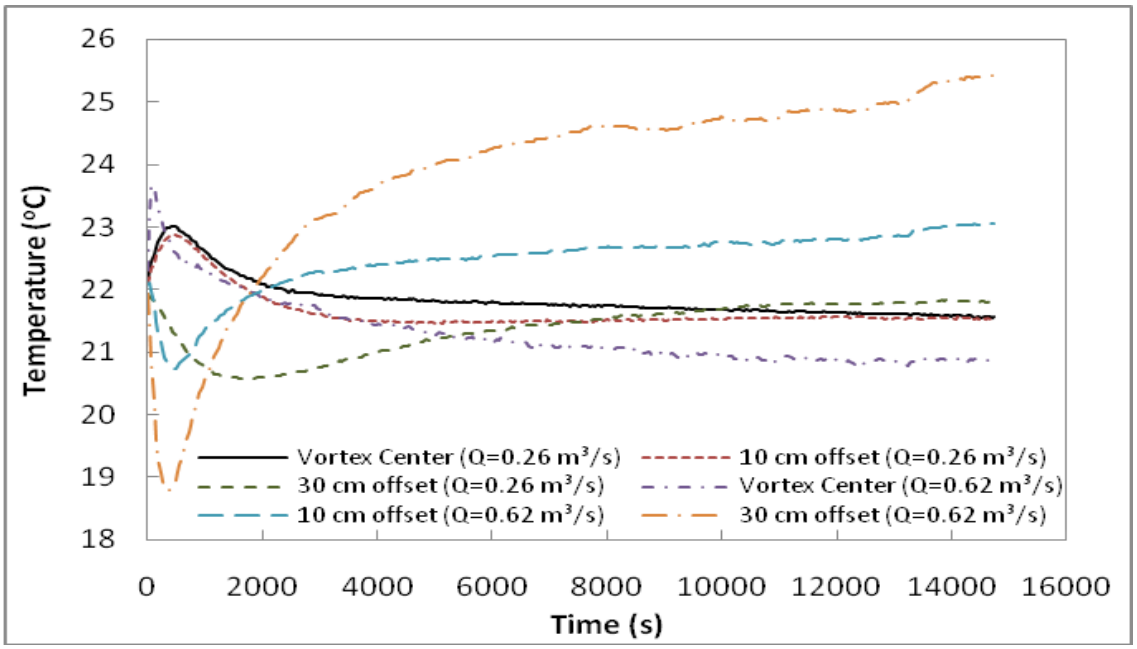

Figure 5.18: Temperature profiles as a function of time at different middle surface locations.

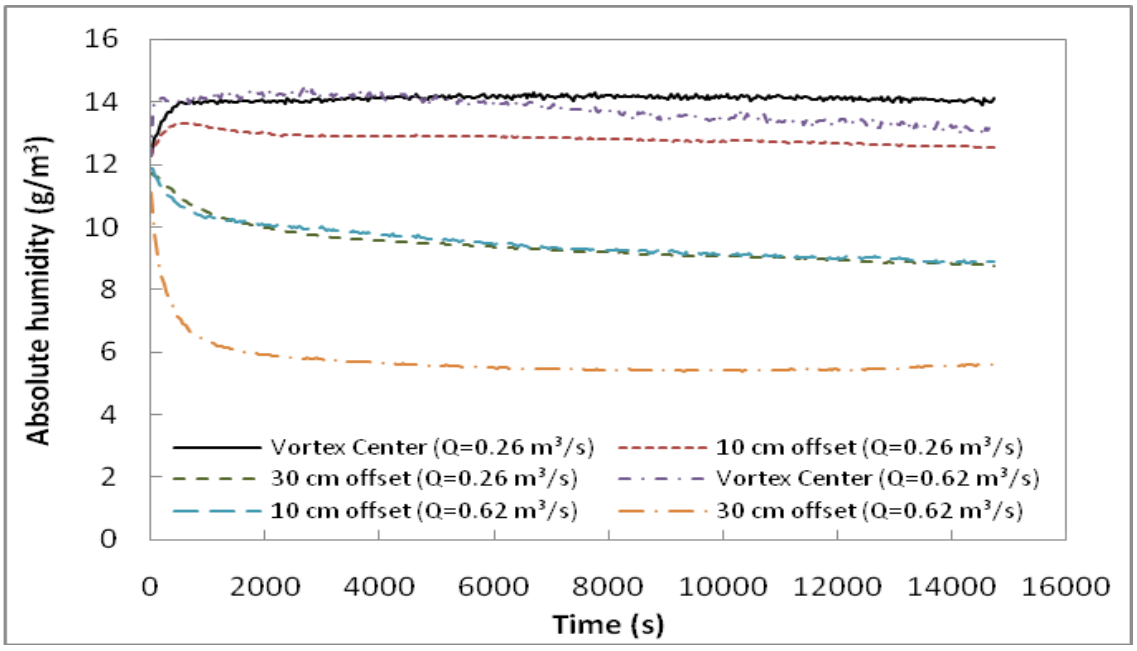

Figure 5.19: Absolute humidity profiles as a function of time at different middle surface locations.

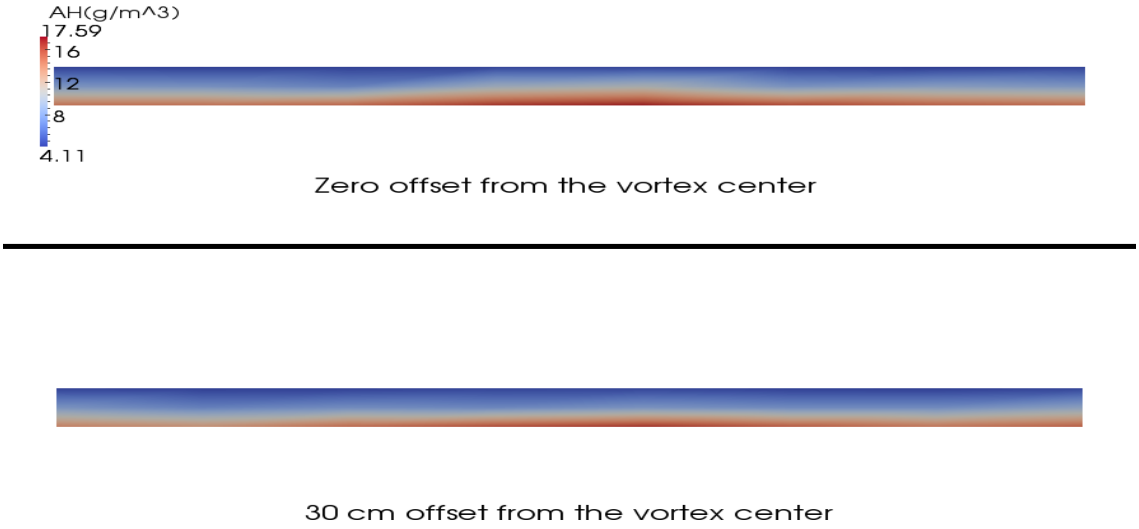

Figure 5.20: A 2D water vapour density distribution at the steady state condition with Q=0.26 m^3 s^{-1}.

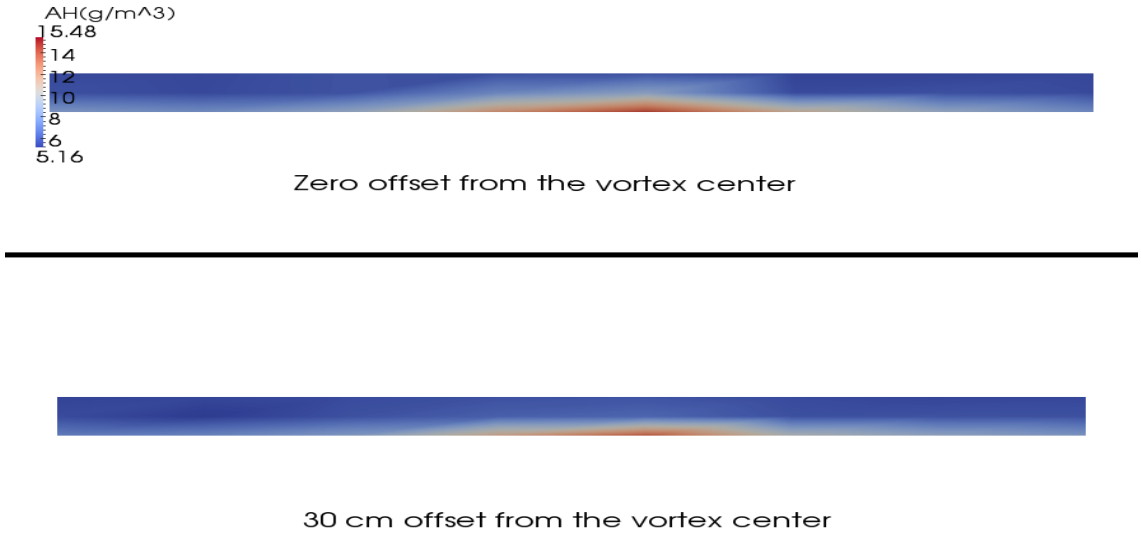

Figure 5.21: A 2D water vapour density distribution at the steady state condition with Q=0.62 m^3 s^{-1}.

Water loss as a function of time due to the vortex influence is shown in Figure 5.22. It clearly shows the significant increase in water loss with the increase of updraft volume flow rate. More details can be found in Table 5.1. Based on these values, the water evaporation rate from the porous media (regolith) is 3 to 8 times larger than the case of still air. As a result, a laboratory dust devil over a water tank has an obvious effect on the water vapour flux. The flows that go through the porous region (Figure 4.19) can be used to argue that the advection flux dominated the water vapour transport mechanism even inside the porous medium. This may be caused by the lower pressure at the vortex center region. This result will be described in the following section. The pressure gradients dominate the diffusion terms. Higher velocities may result in higher pressure gradients and higher water vapour loss rate. Hence, a dust devil can have an important role to affect the water evaporation from the regolith.

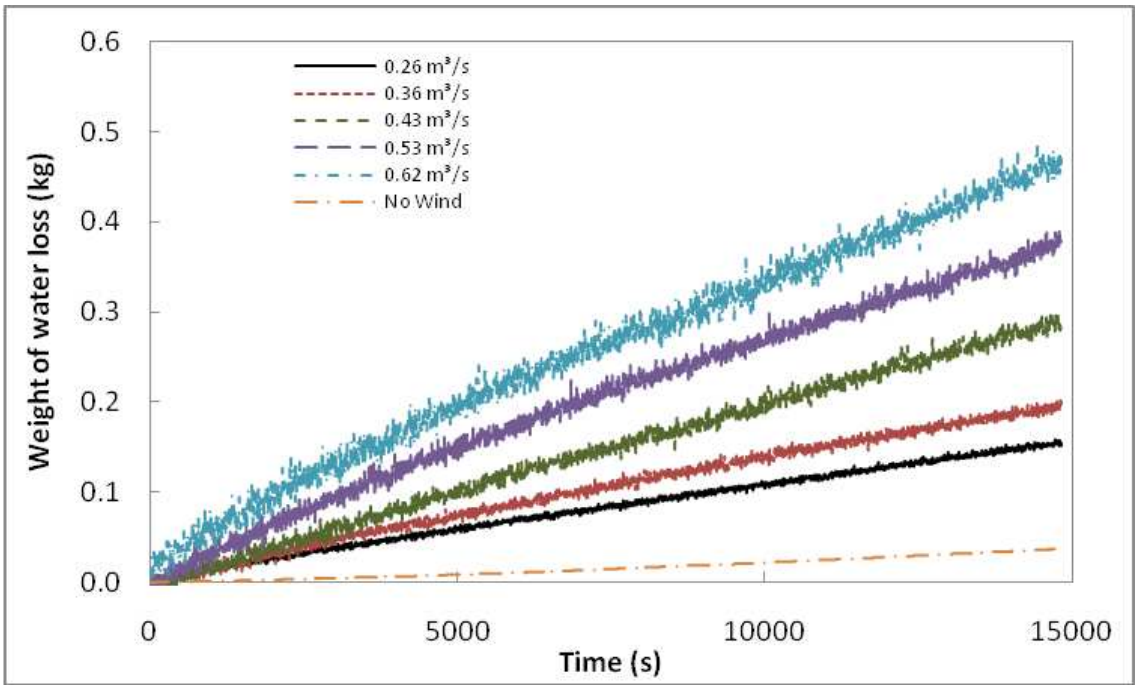

Figure 5.22: The amount of water loss as a function of time.

Table 5.1: Summary of water evaporation rate with varies of flow rate.

Updraft volume flow rate, Q [m^3 s^{-1}]	**Water evaporation rate [kg s^{-1}]**
Zero wind	3.36E-6
0.26	8.71E-6
0.36	1.20E-5
0.43	1.86E-5
0.53	2.16E-5
0.62	2.77E-5

5.3 Numerical Validation of Water Vapour Transport

The section describes the procedure and the results of the numerical model. To validate the numerical model for the influence of laboratory dust devils, the experimental results were adapted. The room conditions were the same as described in the previous section. Water vapour density at the bottom foam surface was set to 0.178 g m^{-3}, and decreased linearly to 0.037 g m^{-3} at the top foam surface to provide initial conditions similar to still air. It should be noted that the bottom foam surface was assumed to have uniform distribution of water vapour density. The air domain has the initial constant absolute humidity of 0.037 g m^{-3}. Same value was applied to the open area boundaries with free slip wall condition. This means the air momentum is zero at these boundaries, but they act as a vapour sink condition to prevent the humidity from filling up the entire domain. The diffusion coefficient was set to 2.55E-5 m^2 s^{-1}. The permeability of porous media was set to 2.22E-9 m^2.

First simulation was set to zero wind, which can be used to verify foam properties and to validate the water vapour flux in steady state condition. Figure 5.23 shows the water vapour distribution at steady state condition. The water vapour density concentrated or filled up at the vortex generator region. The water vapour flux through the interface was calculated to be 1.51 g m^{-2} s^{-1}. It well agrees with the averaged experimental result of 1.63 g m^{-2} s^{-1}. However, the small difference can be accepted because the room ventilation system corresponds to a very small wind that enhances the flux, as shown by Prieto [2006].

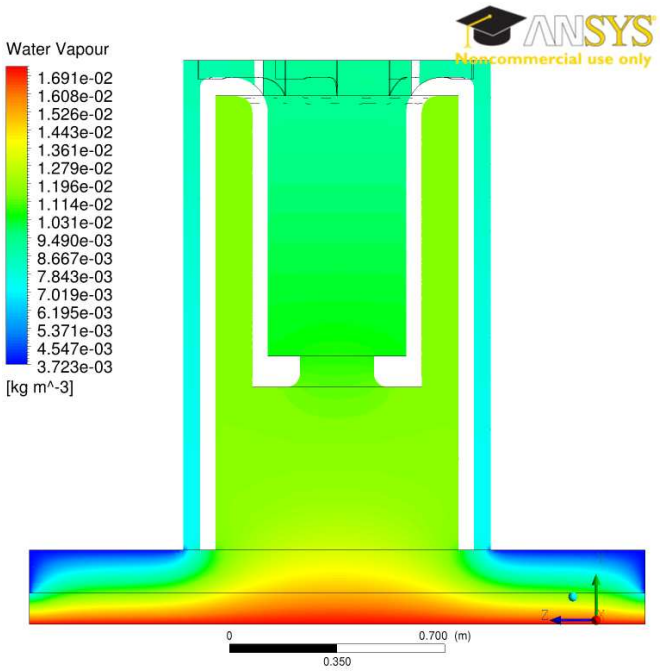

Figure 5.23: A contour view of water vapour density with zero wind velocity.

The repeat simulations with varied momentum sources were used to validate the influence of laboratory dust devils on water vapour transport. All of the numerical simulations in the following were conducted with the initial conditions using the steady state result of zero wind velocity. The numerical simulations were obtained starting from the steady state condition, which was the same as the experimental initial conditions. The simulations were preformed using the Reynolds stress models (RSM-SSG) of turbulence.

Figure 5.24 is an example of water vapour distribution with a laboratory dust devil. It demonstrates that water vapour concentration depends highly on the vortex flow. This is an important evidence for the phenomenon that water vapour was enhanced within the vortex core region. This phenomena were associated with the negative pressure at the vortex core region, as shown in Figure 5.25. The negative pressure was also present in the porous media. Because of the lower pressure the water vapour was dragged towards the vortex center by the pressure gradient. In other words, the

higher water vapour concentration would be present at the vortex center. It agrees with the experimental results at the steady state condition. It should be noted that a significant pressure jump at the inner cylinder is due to a momentum source was set at same location.

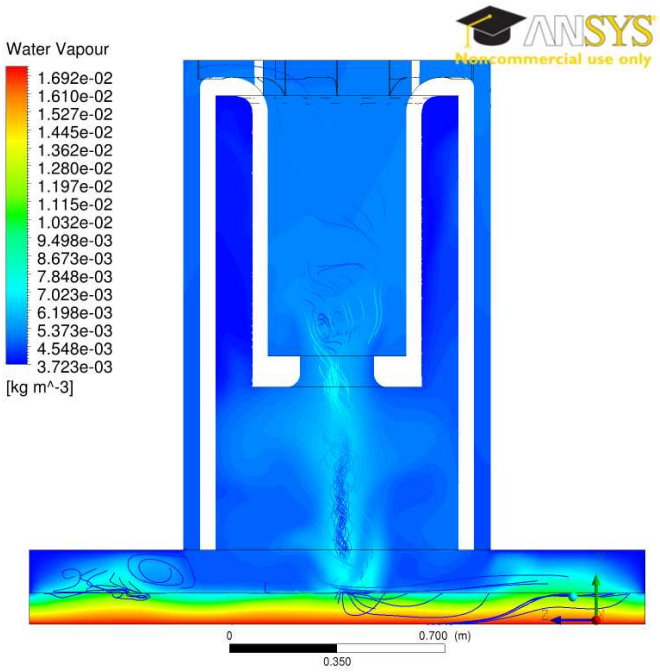

Figure 5.24: A contour view of water vapour density with the presence of a dust devil.

Figure 5.26 shows a contour view of water vapour flux comparison at the interface. It indicates that higher updraft volume flow rate may result in higher water concentration at the vortex center. Moreover, the strong convective term played an important role to increase the water vapour flux rate at the vortex center.

Figure 5.27 shows the relationship between the aspect ratio and mass water vapour transport rate. It was clear that the aspect ratio did not have any influence on the water vapour transport in this case, because we did not test it in this project. Therefore, the aspect ratio can only be described as a geometric parameter of dust devils, according to the results obtained. Its influence on the mass transport requires further investigation.

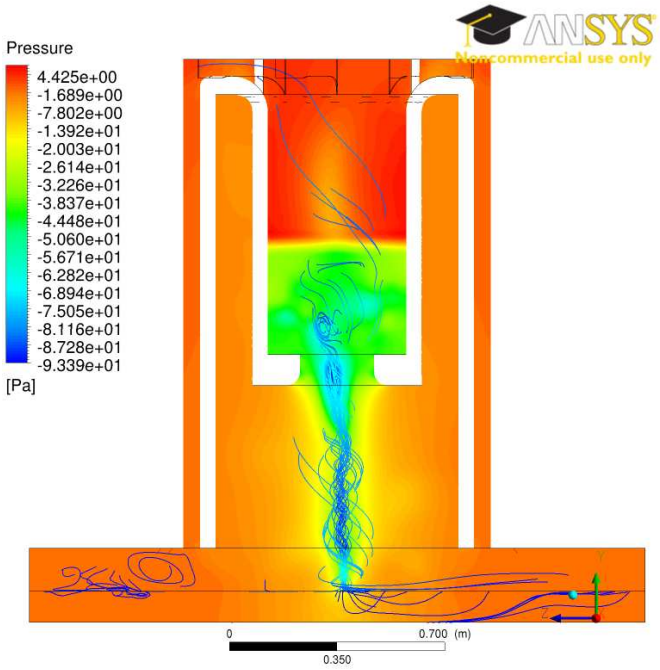

Figure 5.25: A contour view of pressure with the presence of a dust devil.

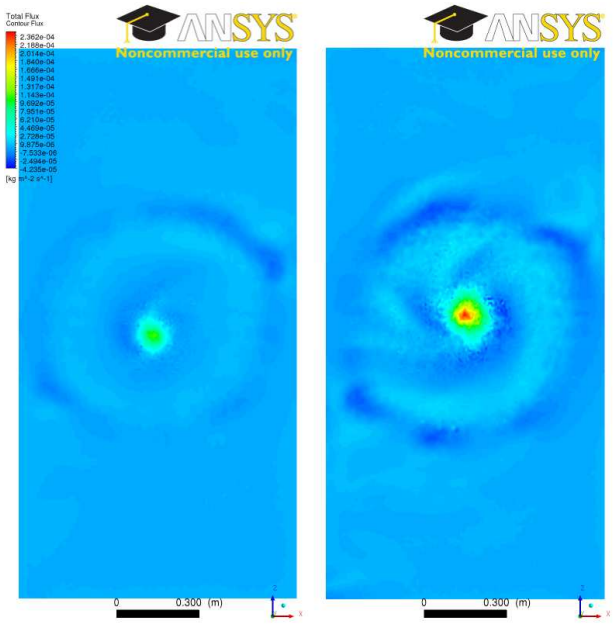

Figure 5.26: Water vapour flux comparison: Left) Q = 0.26 m^3 s^{-1} and Right) Q = 0.62 m^3 s^{-1}.

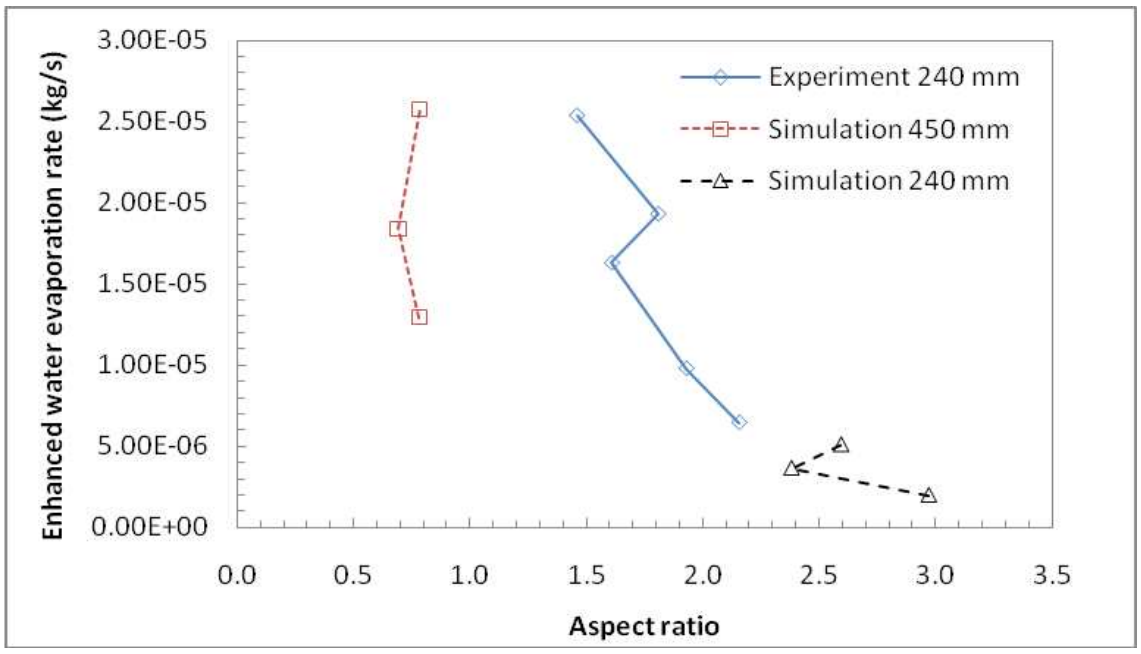

Figure 5.27: The enhancement of water evaporation rate as a function of aspect ratio.

Figure 5.28 and 5.29 present the enhanced water vapour rate that corresponds to two different swirl ratios, Gallus and core, respectively. Since both dimensionless parameters can be argued as relatively constant values in the simulations and experiments, it was concluded that there was no relationship between the enhancement of water evaporation rate and swirl ratios. This is due to the fixed fin curvature and fin angle used in this study. The change of updraft volume flow rate did not affect the relative strength of swirl of vortex flow. In addition, the change of outflow radius did influence both swirl ratios but cannot present any information on the water vapour transport mechanism.

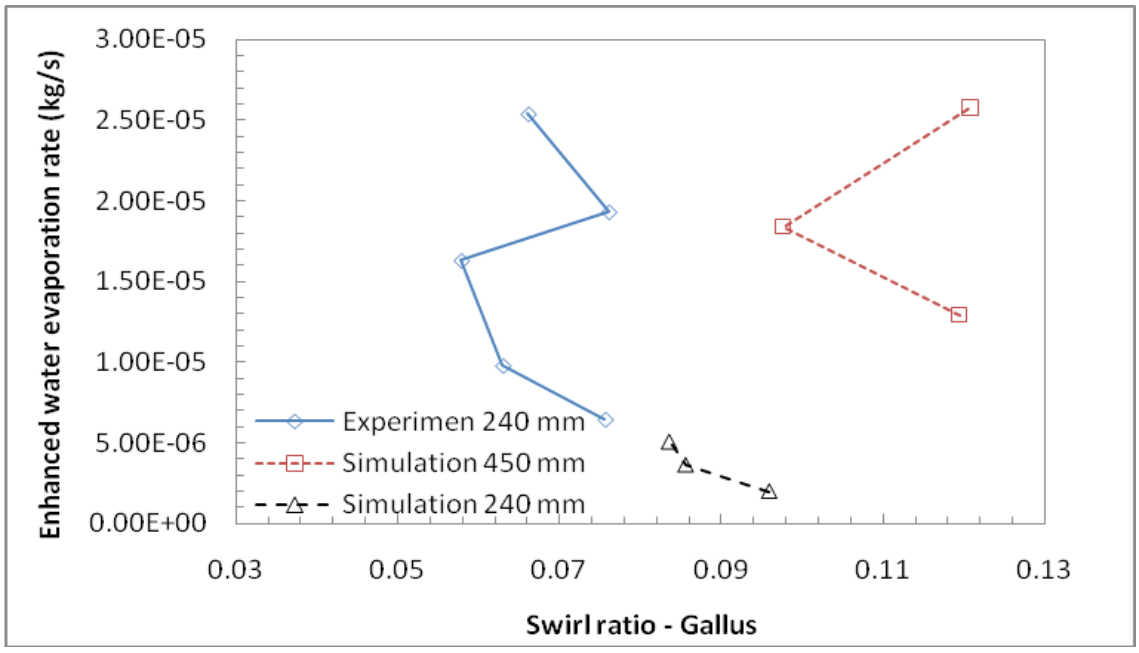

Figure 5.28: The enhancement of water evaporation rate as a function of Gallus' swirl ratio.

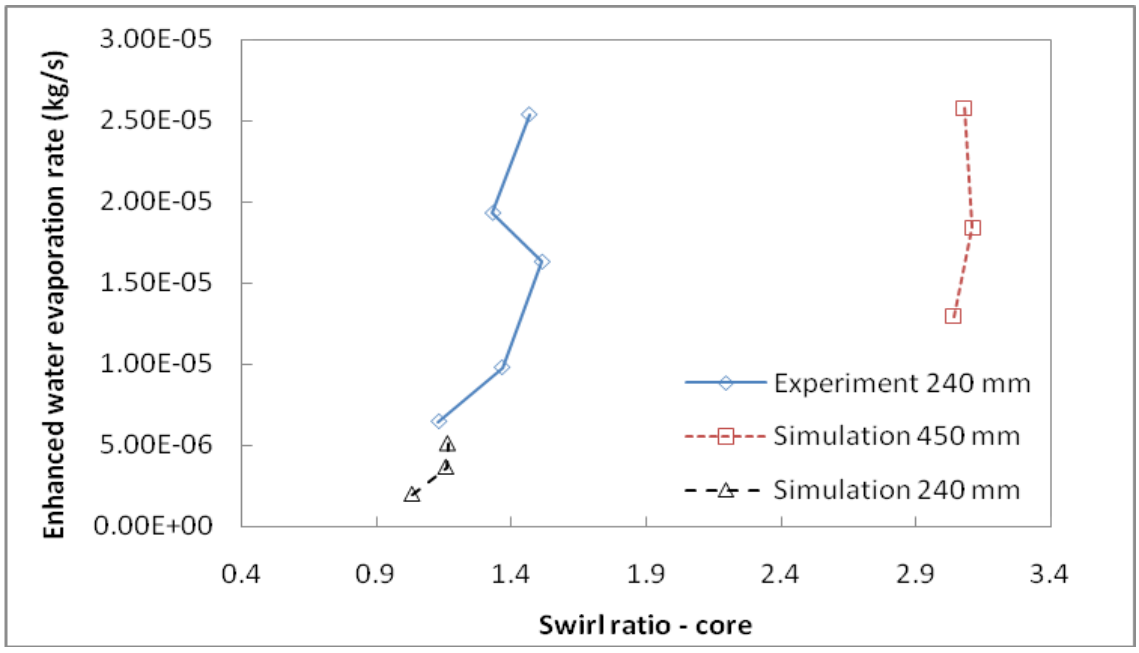

Figure 5.29: The enhancement of water evaporation rate as a function of core swirl ratio.

Figure 5.30 shows clearly that the radial Reynolds number is a major factor in the enhanced water vapour rate. The error bars indicate the standard deviation of the experimental data. The comparison between the experimental and numerical results, show a small difference, which can be explained by the choice of boundary condition in the numerical models. In the experimental set-up, a small gap exists between the liquid water and porous media. If the liquid water contacted the foam, the depth of water would be difficult to determine due to the capillary action. As a result, the flow within the gap may cause a non-uniform water vapour density distribution at the bottom foam surface, seen in Figure 5.31. The vortex center has the same value, but the locations away from the vortex center have less humidity.

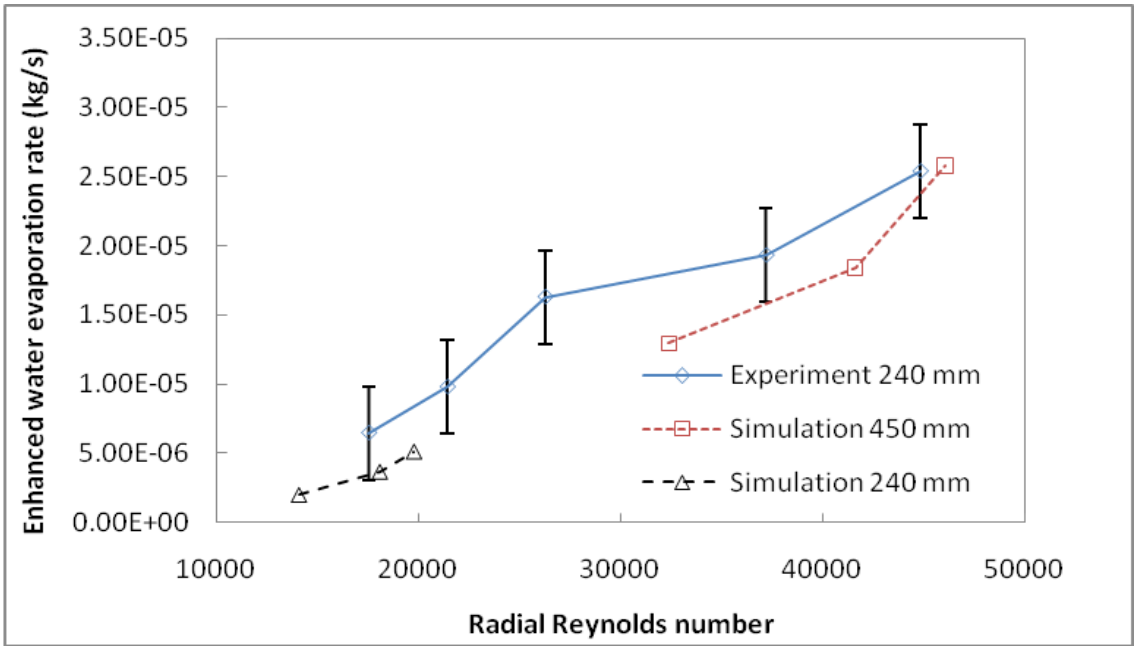

Figure 5.30: The enhancement of water evaporation rate as a function of Reynolds number. The error bars indicate the standard derivation of the experimental data.

To improve the numerical results further, the gap section should be added in the numerical models in a following study. However, adding more interfaces may result in more instability in the CFX-solver code and decreasing computational efficiency.

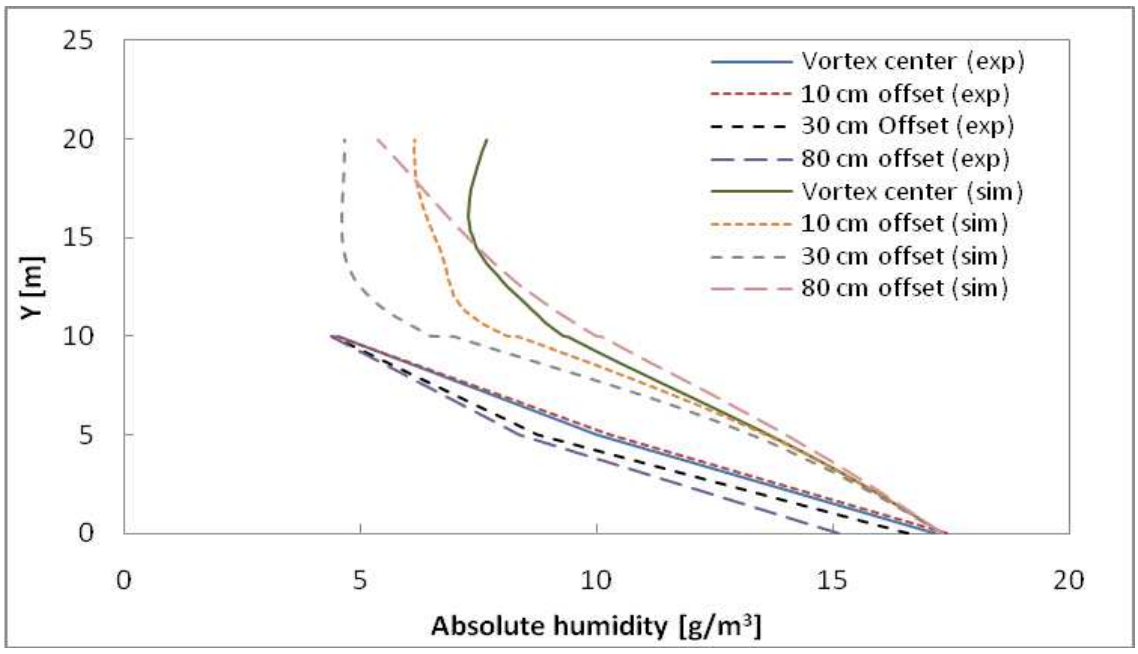

Figure 5.31: Absolute humidity as a function of height.

The increase of result accuracy is also not certain with this highly transient vortex flow.

5.4 Numerical Simulations under Martian Conditions

Gheynani and Taylor [2010] used the LES turbulence model to simulate dust devil-like vortices in highly convective Martian boundary layers at the Phoenix lander site. The simulations were based on zero wind, 4 m s^{-1}, and 8 m s^{-1} wind case. A sensible surface heat flux of 24 W m^{-2} was applied at the bottom surface boundary to cause dust devils to form. They indicated that the vortex column could be up to 1600 m at which height the main circulation disappears. Table 5.2 shows the characteristic parameters of mean dust devil-like vortices on Martian conditions.

Using the geometry of numerical models obtained in the previous section, we can

Table 5.2: The characteristic parameters of Martian dust devil-like vortices from Gheynani and Taylor [2010].

Parameter	**zero wind**	**4 m s^{-1}**	**8 m s^{-1}**
S_{gallus}	2.80	3.61	5.31
S_{core}	1.40	1.81	2.65
a_{core}	1.03	1.37	0.71
Radial Re_{core}	677,302	509,950	781,738

attempt to estimate how much water vapour flux would be enhanced with the presence of dust devils on Mars. First, the atmospheric and porous media properties listed in Table 3.1 were implemented in the numerical model. Zero wind velocity model was then simulated as an initial condition for the other simulations. Figure 5.32 shows the water vapour density distribution for the still air model. It has more uniform distribution within the porous media comparing to the Earth's case due to the lower porosity. The calculation showed the water evaporation rate without a dust devil is 1.67E-05 kg s^{-1}. The result was slightly higher than the model used by Farahaninia [2008]. This is because the use of the numerical model in this study did not have an enclosure to stop the vapour from escaping to the laboratory environment.

Table 5.3 presents the characteristic parameters of dust devil-like flows under Martian conditions in the laboratory scale numerical models. Both swirl ratios and aspect ratio agree with the results obtained in Gheynani and Taylor [2010]. However, the radial Reynolds number is much smaller because the core radius of dust devils on Mars is wider than the laboratory scale.

Table 5.3: Characteristic parameters of Martian dust devil-like flows.

Parameter	**Value**
S_{gallus}	≈ 0.3
S_{core}	≈ 1.8
Aspect ratio	≈ 0.9
Radial Re	2300 to 3900

Figure 5.33 shows the enhancement of water evaporation rate from the porous media as a function of the radial Reynolds number. It indicated that the enhancement ratio

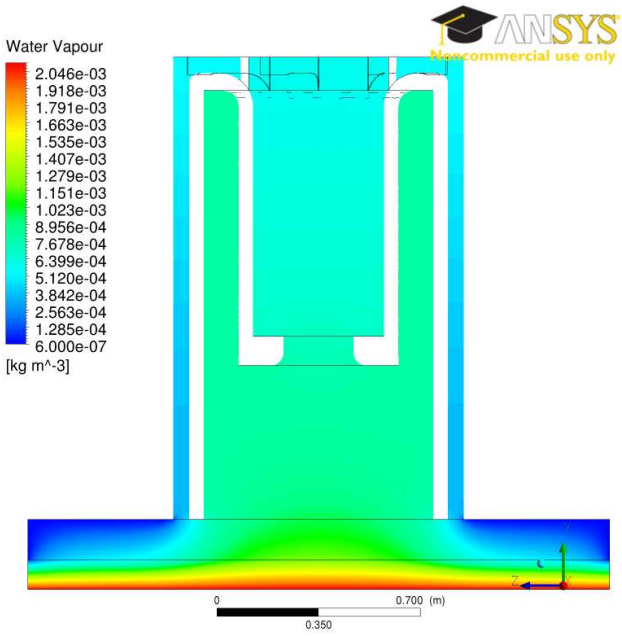

Figure 5.32: A contour view of water vapour density with zero wind velocity under Martian conditions.

of water vapour loss rate between the presence of dust devils and still air models vary from 1.24 to 1.28. The increase of the water vapour transport rate seems to be proportional to the increase in the radial Reynolds number. This means that a dust devil-like flow does affect locally the water evaporation rate under Martian conditions, too.

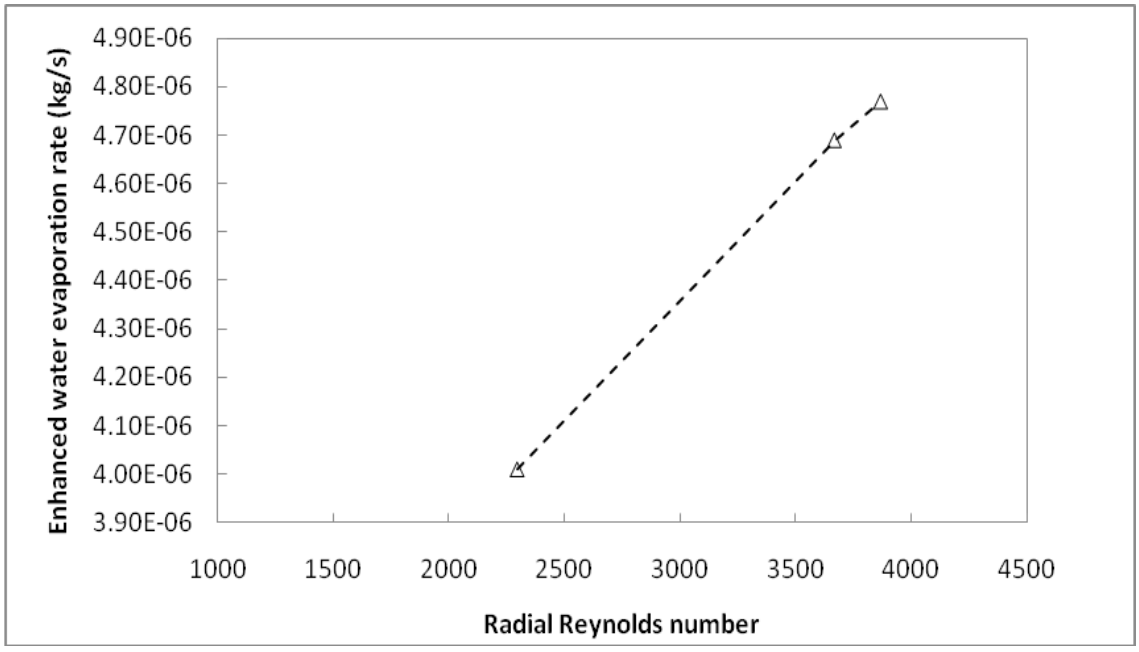

Figure 5.33: Radial Reynolds number as a function of evaporation rate under Martian conditions.

However, the radial Reynolds number of laboratory scale dust devil-like flows are much smaller than the real ones on Mars. When scaling up from the laboratory scale to the Martian atmospheric scale, the effective area should be taken into account. The increase of the scale would result in the decrease of the velocity, if the radial Reynolds number remains the same. However, the enhancement ratio of water evaporation rate may not be a constant value. In other words, the linear relationship between the radial Reynolds number and enhanced evaporation rate may break down when enlarging the size. This is because the enhanced evaporation rate would decrease as a square of effective area. Hence, we only can conclude that dust devils have significantly strong influence on the mass water vapour transport from the Martian regolith when applying to similar size vortices.

Based on these results, the best solution is to scale up the numerical model to simulate realistic sized of dust devils on Mars. However, with the current limitations of ANSYS/CFX 12.0, we may not be able to resolve this numerical problem. This is

because the radius of Martian dust devils (average ≈50 m) is much bigger than the thickness of the Martian regolith (≈10 cm). To keep similar mesh size reasonably fine for both domains, the increase in computational cost would be very significant, requiring a super computer to handle or using an open source code, such as OpenFoam. Hence, the simulation of dust devils at real Martian scales will remain an important target for further investigation.

Another possible solution is to investigate the Sherwood number as a characteristic parameter for this phenomenon. The Sherwood number is defined as the ratio of convective to diffusive coefficients, which relates to a length scale. This is because the comparison with the Sherwood number in flat surfaces seems to indicate that the water vapour enhancement may actually increase, while the Sherwood number would remain constant with the Reynolds number. Further, a special Sherwood number, which was introduced by Farahaninia [2008], may help describe the water vapour transport mechanism from the regolith. This coefficient combined sub-surface and atmospheric transport mechanisms and included all the non-linearities and complexities associated with the influence of surface flows on water vapour transport mechanism from the regolith. However, this would be a recommendation for the future studies of enlarged vortices.

Chapter 6

Conclusions

In this study, a numerical analysis was conducted to predict the local water vapour transport mechanism with the presence of dust devils on Mars. The objective was to provide a better understanding of dust devils in the Martian atmosphere. Since the Phoenix Lander has confirmed the existence of subsurface water ice and the frequent occurrence of dust devils, the study of water vapour transport under the influence of dust devils would be relevant to the interpretation of the mission data. The Martian atmospheric properties used in this study corresponded to the landing site.

To define a suitable numerical model, three characteristic parameters, such as swirl ratio, aspect ratio, and Reynolds number were reviewed. The values of these characteristic parameters corresponding to Martian dust devils were extracted from the NCAR LES results of the Gheynani and Taylor [2010] study. Furthermore, in order to model the Martian regolith, the properties were adapted from Farahaninia [2008]. These data were used in the final, validated numerical models to study the influence of dust devils on the water vapour transport phenomena close to the Phoenix landing site. It should be noted that the experimental and numerical studies used for validation of the numerical model were performed under Earth's conditions.

Initially, several sensitivity studies were performed to find the best shape and dimensions for a new vortex generator. Reynolds stress model (RSM-SSG) was selected to

model turbulence in the CFX-solver, based on the review of previous studies. The modified generator model was an improvement over the existing Open-type vortex generator at the University of Alberta. The sensitivity study indicated the fin angle, outflow radius, and inlet height were the most relevant parameters of the structure and provided recommended ranges of values. However, only the outflow radius, in addition to the updraft flow rate, was varied in this study. A modified vortex generator was designed and constructed following the recommended values.

SPIV flow measurement technique was used to obtain the velocity field of laboratory dust devils for validation of the numerical model. It was observed that the wider outflow radius would result in a wider vortex core radius. The increase of updraft volume flow rate did increase maximum tangential velocity in the experiments. However, the swirl ratios of both Gallus and core definitions essentially did not change with the volume flow rate, despite small variations. This is in agreement with the sensitivity study, since the fin angle was fixed. In other words, the flow passing through the fixed fin angle would create a similar strength of swirl ratio. Furthermore, the aspect ratio was independent of either the outflow radius or the updraft volume flow rate, since it is a scaling factor for the vortex shape. The radial Reynolds number was revealed as a useful characteristic parameter in studying the influence of dust devils on the water vapour transport rate.

A numerical model with the water vapour transport part included was used for validation with the SPIV results. Not only was the flow field successfully validated but also the simulation did show the presence of flow in the porous media. This indicates that water vapour concentration may be associated with the vortex flow due to the flow that happens inside the porous media.

Experiments of water vapour transport were conducted at Earth's conditions. One hundred twenty-eight solid-state humidity/temperature sensors were used to measure the humidity and temperature profiles during the experiments. The data show that steady state condition can be reached about 8 hours after adding the distilled water

in the reservoir (water tank). A significant increase of temperature in the middle of the foam happened due to the absorption process (exothermal) at the beginning of measurements. Once the foam was fully saturated, the temperature decreased slowly to the room condition. Repeated experiments were performed to study the water vapour loss rate with different flow rates. Water vapour concentration at the vortex center had higher humidity, but this region became smaller with higher updraft volume flow rate. As a result, the influence of laboratory dust devils on the water evaporation rates was obvious. The water evaporation rate from the porous media was 3 to 8 times larger than under still air condition.

A numerical model of the water evaporation experiments was set to the experimental conditions for validation purposes. The bottom porous media surface was assumed to have a constant water vapour density (humidity). The numerical results agreed reasonably well with the experiments in the still air and vortex cases. In all cases a slightly higher water vapour mass flux was measured, but those differences could be shown to be caused by limitations in the boundary conditions used. An additional domain between the liquid water and porous media can be considered to improve the results in the future studies. However, the results showed a good agreement on the tendency between radial Reynolds number and enhanced evaporation rate. It implies that this numerical model can be used to study the water vapour mass transport on Mars.

The results with various updraft momentum sources demonstrated that the water vapour flux would be influenced by the laboratory dust devils. Higher humidity would be carried by the vortex flow due to the negative pressure within the vortex core. In addition, an increase in the updraft volume flow rate through the fan would result in higher water vapour flux. In this study, the most relevant characteristic parameter was the radial Reynolds number. It presented a good relationship between its values and water vapour mass transport from the regolith.

Finally, the Martian conditions were implemented in the numerical model. This nu-

merical study was designed to investigate the effect of dust devils on mass water vapour transport mechanism from the Martian regolith. The characteristic parameters, such as swirl ratio and aspect ratio, could be reproduced from the results of LES model provided by collaborators. However, the radial Reynolds numbers were much smaller due to the smaller core radius produced in the range studied. When dust devil-like flows were present, an increase of 1.25 times in water evaporation rate from the regolith was calculated, but this result only applies to similar laboratory scales.

In summary, dust devils can be concluded to have a strong influence on the water vapour transport mechanism on both Earth and Mars. The radial Reynolds number is a good characteristic parameter in this study, but may not be a capable scaling factor to predict the water evaporation rate with the enlarged scale dust devils on Mars.

Two recommendations are made for the future studies on similar topics. One is using an open source code, OpenFoam, and one is to investigate the special Sherwood number. The use of OpenFoam would result in the ability to resolve the interface and scale up problems, because this software would allow access to more powerful computers. The special Sherwood number may be a useful scaling factor to help predict the surface flows of water vapour in scaled up models on Mars.

Bibliography

R. J. Adrian. Multi-point optical measurements of simultaneous vectors in unsteady flow - a review. *Int. J. Heat and Fluid Flow*, 7:127–145, 1986.

R. J. Adrian. Particle-imaging techniques for experimental fluid mechanics. *Annual reviews fluid mechanics*, pages 261–304, 1991.

G. Altimas. Evaluation of local kinematics of atmospheric vortex flow. Master's thesis, University of Alberta, 2007.

A. A. Alzaydi and C. A. Moore. Combined pressure and diffusional transition region flow of gases in porous media. *AICHE J.*, 24(1):35–43, 1978.

ANSYS. *ANSYS/CFX12.0 Manual, Theory.* Ansys Inc., Waterloo, Ontario, Canada, 2009.

R. Arvidson, D. Adams, G. Bonfiglio, P. Christensen, S. Cull, M. Golombek, J. Guinn, E. Guinness, T. Heet, R. Kirk, A. Knudson, M. Malin, M. Mellon, A. McEwen, A. Mushkin, T. Parker, F. S. IV, K. Seelos, P. Smith, D. Spencer, T. Stein, and L. Tamppari. Mars Exploration Program 2007 Phoenix landing site selection and characteristics. *J. Geophys. Res.*, 113(E00A03), 2008. doi:10.1029/2007JE003021.

M. R. Balme, P. L. Whelley, and R. Greeley. Mars: Dust devil track survey in Argyre Planitia and Hellas Basin. *J. Geophys. Res.*, 108(E8), 2003.

A. I. Barcilon. Vortex decay above a stationary boundary. *J. Fluid. Mech.*, 27: 155–175, 1967. doi:10.1017/S0022112067000114.

J. Bear. *Dynamics of Fluids in Porous Media.* Dover Publications, 1988.

R. B. Bird, W. E. Stewart, and E. N. Lightfoot. *Transport Phenomena.* John Wiley and Sons, Inc., 2 edition, 2001.

W. V. Boynton, W. C. Feldman, S. W. Squyres, T. H. Prettyman, J. Bruckner, L. G. Evans, R. C. Reedy, R. Starr, J. R. Arnold, D. M. Drake, P. A. J. Englert, A. E. Metzger, I. Mitrofanov, J. I. Trombka, C. d'Uston, H. Wanke, O. Gasnault, D. K. Hamara, D. M. Janes, R. L. Marcialis, S. Maurice, I. Mikheeva, G. J. Taylor, R. Torkar, and C. Shinohara. Distribution of Hydrogen in the near surface of Mars: Evidence for surface ice deposit. *Science*, 297:81–85, 2002.

E. Buckingham. Studies on the movement of soil moisture. *USDA Bur. Soils Bull.*, (38), 1907.

J. M. Burgers. A mathematical model illustrating the theory of turbulence. *Adv. Appl. Mech.*, 1:171 – 199, 1948.

Y. A. Çengel. *Heat Transfer: A Practical Approach*. McGraw-Hill, 2 edition, 2002.

C. R. Church and J. T. Snow. *The Tornado: Its Structure, Dynamics, Prediction, and Hazards*, chapter Laboratory Models of Tornadoes, pages 277 – 295. American Geophysical Union, Washington, D. C., USA, 1993.

C. R. Church, J. Snow, G. Baker, and E. M. Agee. Characteristics of tornado-like vortices as a function of swirl ratio: A laboratory investigation. *J. Atmos. Sci.*, 36: 1755 – 1776, 1979.

S. M. Clifford and D. Hillel. Knudsen diffusion: The effect of small pore size and low gas pressure on gaseous transport in soil. *Soil Science*, 141(4):289–297, 1986.

H. Darcy. *Les Fontaines Publique de la Ville de Dijon*. Dalmaton, 1856.

R. P. Davies-Jones. The dependence of core radius on swirl ratio in a tornado simulator. *J. Atmos. Sci.*, 30:1427 – 1430, 1973.

R. P. Davies-Jones. Laboratory simulations of tornadoes. *Preprints Symposium on Tornadoes*, pages 151 – 174, 1976.

R. P. Davies-Jones. *Thunderstorms: A Social, Scientific and Technological Documentary*, volume 2, chapter Tornadoes Dynamics. U.S. Department of Commerce, Washington, D. C., USA, 1982.

R. P. Davies-Jones and E. Kessler. *Weather and Climate Modification*, chapter Tornadoes, pages 552–595. John Wiley, New York, USA, 1974.

S. R. de Groot and P. Mazur. *Non-Equilibrium Thermodynamics*. Dover Publications, Inc, 1984.

D. D. Do. *Adsorption Analysis: Equilibria and Kinetics*, volume 2. Imperial College Press, 1998.

B. S. Dooley. *Stereo Digital Particle Image Velocimetry Investigation of a Free Surface Mixing Layer*. PhD thesis, California Institute of Technology, 2005.

C. A. Doswell. A review for forecasters on the application of hodograohs to forecasting severe thunderstorms. *National weather digest*, 16:2–16, 1991.

K. S. Edgett and M. C. Malin. Martian dust raising and surface albedo controls: Thin, dark (and sometimes bright) streaks and dust devils in MGS high-resolution images. In *XXXI Lunar and Planetary Science*, 2000.

M. D. Ellehoj, H. P. Gunnlaugsson, P. A. Taylor, H. Kahanpää, K. M. Bean, B. A. Cantor, B. T. Gheynani, L. Drube, D. Fisher, A.-M. Harri, C. Holstein-Rathlou, M. T. Lemmon, M. B. Madsen, M. C. Malin, J. Polkko, P. H. Smith, L. K. Tamppari, W. Weng, and J. Whiteway. Convective vortices and dust devils at the Phoenix Mars mission landing site. *J. Geophys. Res.*, 115(E00E16), 2010. doi:10.1029/2009JE003413.

A. Farahaninia. The effects of natural convection and wind on water vapour transport from a porous medium: Application to water transport on Mars. Master's thesis, University of Alberta, 2008.

J. H. Ferziger and M. Peric. *Computational Methods for Fluid Dynamics*. Springer-Verlag, Berlin, heidelberg, germany, 3 edition, 2002.

A. Fick. Über Diffusion. *Annalen der Physik und Chemie*, 94:59–86, 1855.

D. A. Fisher, D. P. Winebrenner, and H. Stern. Lineations on the White accumulation areas of the residual northern ice cap of Mars: Their relation to the accublation and ice flow hypothesis. *Icarus*, 159(1):39–52, 2002.

T. Fouchet, E. lellouch, N. I. Ignatiev, F. Forget, D. V. Titov, M. Tschimmel, F. Montmessin, V. Formisano, M. Giuranna, A. Maturilli, and T. Encrenaz. Martian water vapor: Mars express PFS/LW observations. In *The 7th internatinal conference on Mars*, number 3150 in 1, 2007.

W. A. Gallus, F. L. Haan, P. P. Sarkar, K. Le, and J. Wurman. Comparison of numerical model and laboratory simulator tornado wind fields with radar observations of the Spencer, South Dakota tornado. In *Symposium on the Challenges of Severe Convective Storms*, Atlanta, GA, USA, 2006. Amer. Meteor. Soc.

B. T. Gheynani and P. A. Taylor. Large eddy simulation of typical dust devil-like vortices in highly convective martian boundary layers at the phoenix lander site. *Plant. Space Sci.*, 2010. doi:10.1016/j.pss.2010.10.011.

E. R. Gilliland, R. Baddour, G. P. Perkinson, and K. Sladek. Diffusion on surfaces. *Ind. Eng. Chem. Fund.*, 13(3):95 – 99, 1974.

A. Grant. Dust devils in the sub-artic. *Weather*, 4:402 – 403, 1949.

L. Gu, C. K. Ho, O. Plumb, and S. W. Webb. Diffusion with condensation and evaporation in porous media. In *AIAA/ASME Joint Thermophysics and Heat Transfer Conference*, volume 2, pages 213 – 220. ASME, 1998.

F. L. Haan, W. A. Gallus, and P. P. Sarkar. Design, construction and performance of a large tornado simulator for wind engineering applications. *Engineering Structures*, 30:1146–1159, 2008.

R. M. Haberle, F. Montmessin, M. A. Kahre, and J. Schaeffer. The role of the north residual cap in the present Mars water cycle. In *The 7th internatinal conference on Mars*, number 3161 in 1, 2007.

G. D. Hess and K. T. Spillane. Characteristics of dust devils in Australia. *J. Appl. Met.*, 29:498 – 507, 1990.

P. A. C. Howells, R. Rotunno, and R. K. Smith. A comparative study of atmospheric and labourtory-analogue numerical tornado-vortex models. *Q. J. R. meteorol. Soc.*, 114:801–822, 1988.

C. Hsu. Laboratory modeling of the tornado suction mechanism. In *8th Conference on Severe Local Storms*, pages 199 –202. AMS, 1973.

M. K. Hubbert. Darcy law and the field equations of the flow of underground fluids. *Trans. Amer. Inst. Min. Mandal. Eng.*, 207:222–239, 1956.

T. L. Hudson, O. Aharonson, N. Schorghofer, C. B. Farmer, M. H. Hecht, and N. T. Bridges. Water vapour diffusion in Mars subsurface environments. *J. Geophys. Res. - Planets*, 112:E05016, 2007.

B. M. Jakosky, A. P. Zent, and R. W. Zurek. The Mars water cycle: Determining the role of exchange with the regolith. *Icarus*, 130(1):87–95, 1997.

D. B. Jaynes and A. Rogowski. Applicability of fick's law to gas diffusion. *Soil Sci. Soc. Am. J.*, 47:425–430, 1983.

D. J. Jerolmack, D. Mohrig, J. P. Grotzinger, D. A. Fike, and W. A. Watters. Spatial grain size sorting in eolian ripples and estimation of wind conditions on planetary surfaces: Application to Meridiani Planum, Mars. *J. Geophys. Res. - Planets*, 111 (E5):E12S02, 2006.

F. S. Johnson. Atmosphere of Mars. *Science*, 150(3702):1445–1448, 1965.

D. D. Joseph, D. A. Nield, and G. Papanicolaou. Nonlinear equation governing flow in a saturated porous medium. *Water Resour. Res.*, 18(4):1049–1052, 1982.

H. H. Kieffer, S. C. Chase, T. Z. Martin, E. D. Miner, and F. Donpalluconi. Martian north pole summer temperatures: dirty water ice. *Science*, 194:1341 – 1344, 1976.

M. Knudsen. Die gesetze der molecularströmung und der inner reibungsströmung der gase durch röhren. *Annalen der Physik und Chemie*, 28:75–130, 1909.

L. Kuai, F. L. Haan, W. A. Gallus, and P. P. Sarkar. Cfd simulations of the flow field of a laboratory-simulated tornado for parameter sensitivity studies and comparison with field measurements. *Wind and Structures*, 11(2):75–96, 2008.

B. E. Launder and D. Spalding. The numerical computation of turbulent flows. *Comput. Methods Appl. Mech. Eng.*, 3:269 – 289, 1974.

B. D. Lee and R. B. Wilhelmson. The numerical simulation of nonsupercell tornadogenesis. part ii: Evolution of a family of tornadoes along a weak outflow boundary. *American Meteorological Society*, 1997.

C. Leovy. Weather and climate on Mars. *Nature*, 412:245 – 249, 2001.

D. C. Lewellen and W. S. Lewellen. The influence of local swirl ratio on tornado intesification near the surface. *J. Atmos. Sci.*, 57:527 – 544, 2000.

W. S. Lewellen. A solution for three-dimensional vortex flows with strong circulation. *J. Fluid. Mech.*, 14:420 – 432, 1962.

W. S. Lewellen. *The Tornado: Its Structure, Dynamics, Prediction, and Hazards*, chapter Tornado Vortex Theory, pages 19–39. American Geophysical Union, Washington, D. C., USA, 1993.

W. S. Lewellen and Y. P. Sheng. Modeling tornado dynamics. Report 1585, Aeronaut. Rer. Assoc. of Princenton Inc., Springfield, Va, USA, 1980.

K. Lodders and J. B. Fegley. *The Planetary Scientist's Companion*. Oxford University Press, New York, 1998.

C. Ludwig. Diffusion zwischen ungleich erwärmten Orten gleich zusammen-gesetzter Lösungen. *Sitzber. Akad. Wiss.*, 20:539, 1856.

M. C. Malin. Density of Martian north polar layered deposits - implications for composition. *Geophys. Res. Lett.*, 13(5):444–447, 1986.

E. A. Mason and A. P. Malinauskas. *Gas Transport in Porous Media: The Dusty-Gas Model*. Elsevier, 1983.

E. A. Mason, A. P. Malinaukas, and R. B. E. III. Flow and diffusion of gases in porous media. *J. Chem. Phys.*, 46(8):3199–3216, 1967.

W. J. Massmann. A review of the molecular diffusivities of H_2O, CO_2, CH_4, CO, O_3, SO_2, NH_3, N_2O,NO, and NO_2 in air, O_2 and N_2 near STP. *Amospheric Enviroment*, 32(6):1111–1127, 1998.

W. J. Massmann and D. F. Farrier. Effects of atmospheric pressures on gas transport in the vadose zone. *Water Resour. Res.*, 28:777–791, 1992.

M. T. Mellon and B. M. Jakosky. High-resolution thermal inertia mapping from the Mars Global Surveyor Thermal Emission Spectrometer. *Icarus*, 148(2):437–455, 2000.

M. T. Mellon and B. M. Jakosky. Geographic variations in the thermal and diffusive stability of ground ice on Mars. *J. Geophys. Res.*, 98(E2):3345–3364, 1993.

S. M. Metzger, J. R. Johnson, J. R. Carr, T. J. Parker, and M. T. Lemmon. Dust devils vortices seen by the Mars Pathfinder Camera. *Geophys. Res. Lett.*, 26:2781 – 2784, 1999.

I. G. Mitrofanov, D. Animov, A. S. Kozyrev, M. L. L. A. B. Sanin, V. Tretyakov, A. Krylov, V. Shvetsov, W. V. Boynton, D. Hamara, C. Shinohara, and R. S. Saunders. Maps of subsurface Hydrogen from the High Energy Neutron Detector, Mars Odyssey. *Science*, 297(78):78 –81, 2002.

I. G. Mitrofanov, M. T. Zuber, M. L. Litvak, W. V. Boynton, D. E. Smith, D. Drake, D. Hamara, A. S. Kozyrev, A. B. Sanin, C. Shinohara, R. S. Saunders, and V. Tretyakov. Co_2 snow depth and subsurface water-ice abundance in the northern hemisphere of Mars. *Science*, 300:2081 –2084, 2003.

H. J. Moore and B. M. Jakosky. Viking landing sites, remote-sensing observations, and physical-properties of Martian surface materials. *Icarus*, 81(1):164 –184, 1989.

B. R. Morton. Vorticity and vortices. In *Proceedings of the Joint IUTAM/IUGG Symposium on Intense Atmospheric Vortices*, 1981.

J. R. Murphy and S. Nelli. Mars Pathfinder convective vortices: Frequency of occurence. *Geophys. Res. Lett.*, 29(23):2103, 2002.

D. A. Nield and A. Bejan. *Convection in Porous Media*. Springer, 2 edition, 1999.

D. S. Nolan. A new scaling for tornado-like vortices. *American Meteorological Society*, pages 2639 – 2645, 2005. Notes and Correspondence.

D. S. Nolan and B. F. Farrell. The structure and dynamics of tornado-like vortices. *J. Atmos. Sci.*, 56:2908 – 2936, 1999.

L. Prieto. A numerical model of local water vapour transport. Master's thesis, University of Alberta, 2006.

M. Raffel, C. E. Willert, S. T. Werely, and J. Kompenhans. *Particle Image Velocimetry: A Practical Guide*. Springer, 2 edition, 2007.

W. J. Rankine. *A Manual of Applied Mechanics*. Charles Griffin and Co., London, England, 1858.

W. Rodi and M. Mulas. *Engineering Turbulence Modelling and Experiments 6*. Elsevier, 1 edition, 2005.

N. Rott. On the viscous core of a line vortex. *Z. Agnew Math. Mech.*, 9:543 – 553, 1958.

R. Rotunno. Numerical simulation of a laboratory vortex. *J. Atmos. Sci.*, 34:1942 – 1956, 1977.

R. Rotunno. Vorticity dynamics of a convective swirling boundary layer. *J. Fluid Mech.*, 97:623 – 640, 1980.

H. Savijarvi. Mars boundary layer modeling: Diurnal moisture cycle and soil properties at the Viking lander 1 site. *Icarus*, 117:120–127, 1995.

A. H. Shapiro. Film notes for vorticity. *National Committee for Fluid Mechnics Films*, 1969.

P. C. Sinclair. General characteristics of dust devils. *J. Appl. Met.*, 8:32 – 45, 1969.

B. E. Sleep. Modeling transient organic vapor transport in porous media with the dusty gas model. *Adv. Water Resour.*, 22(3):247 – 256, 1998.

P. H. Smith, L. Tamppari, R. E. Arvidson, D. Bass, D. Blaney, W. Boynton, A. Carswell, D. Catling, B. Clark, T. Duck, E. DeJong, D. Fisher, W. Goetz, P. Gunnlaugsson, M. Hecht, V. Hipkin, J. Hoffman, S. Hviid, H. Keller, S. Kounaves, C. F. Lange, M. Lemmon, M. Madsen, M. Malin, W. Markiewicz, J. Marshall, C. McKay, M. Mellon, D. Michelangeli, D. Ming, R. Morris, N. Renno, W. T. Pike, U. Staufer, C. Stoker, P. Taylor, J. Whiteway, S. Young, and A. Zent. Introduction to special section on the Phoenix Mission: Landing Site Characterization Experiments, Mission Overviews, and Expected Science. *J. Geophys. Res.*, 113(E00A18), 2008. doi:10.1029/2008JE003083.

P. H. Smith, L. Tamppari, R. E. Arvidson, D. Bass, D. Blaney, W. Boynton, A. Carswell, D. Catling, B. Clark, T. Duck, E. DeJong, D. Fisher, W. Goetz, P. Gunnlaugsson, M. Hecht, V. Hipkin, J. Hoffman, S. Hviid, H. Keller, S. Kounaves, C. F. Lange, M. Lemmon, M. Madsen, W. Markiewicz, J. Marshall, C. McKay, M. Mellon, D. Ming, R. Morris, W. T. Pike, N. Renno, U. Staufer, C. Stoker, P. Taylor, J. Whiteway, and A. Zent. H_2O at the Phoenix Landing Site. *Science*, 325(5936):58–61, 2009. doi:10.1126/science.1172339.

J. T. Snow. A review of recent advances in tornado vortex dynamics. *Rev. Geophy. Space Phys.*, 20(4):953 – 964, 1982.

C. G. Speziale, S. Sarkar, and T. B. Gatski. Modelling the pressure-strain correlation o turbulence: An invariant dynamical system approach. *J. Fluid. Mech.*, 227:245 – 272, 1991.

R. Sullivan, D. Banfield, J. F. B. III, W.Calvin, D. Fike, M. Golombek, R. Greeley, J. Grotzinger, K. Herknhoff, M. Malin, D. Ming, L. A. Soderblom, S. W. Squyres, S. Thompson, W. A. Watters, C. M. Weitz, and A. Yen. Aeolian processes at the Mars Exploration Rover Meridiani Planum landing site. *Nature*, 436(7047):58–61, 2005.

P. A. Taylor, H. Kahanpää, W. Weng, A. Akingunola, C. Cook, M. Daly, C. Dickinson, A. Harri, D. Hill, V. Hipkin, J. Polkko, and J. Whiteway. On pressure measurement and seasonal pressure variations during the Phoenix mission. *J. Geophys. Res.*, 115 (E00E15), 2010. doi:10.1029/2009JE003422.

P. Thomas and P. J. Gierasch. Dust devils on Mars. *Science*, 230:175 – 177, 1985.

D. C. Thorstenson and D. Pollock. Gas transport in unsatured zones: Multicomponent systems and the adequacy of Fick's law. *Water Resour. Res.*, 25(3):477–507, 1989.

B. J. Travis, N. D. Rosenberg, and J. N. Cuzzi. On the role of widespread subsurface convection in bringing liquid water close to Mars' surface. *J. Geophys. Res.*, 108 (E4), 2003.

H. K. Versteeg and W. Malalasekera. *An Introduction to Computational Fluid Dynamics*. Pearson Education Hall, 1995.

N. B. Ward. The exploration of certain features of tornado dynamics using a laboratory model. *J. Atmos. Sci.*, 29:1194 – 1204, 1972.

T. Wilson and R. Rottuno. Numerical simulation of a laminar vortex flow. In *Proceedings of International Conference on Computational Methods and Experimental Measurements*, Washington, D. C., USA, 1982. ISCME.

A. P. Zent, M. H. Hecht, D. R. Cobos, S. E. Wood, T. L. Hudson, S. M. Milkovich, L. P. DeFlores, and M. T. Mellon. Initial results from the thermal and electrical

conductivity probe (TECP) on Phoenix. *J. Geophys. Res.*, 115(E00E14), 2010. doi:10.1029/2009JE003420.

Appendix A

Calculations for the Relevant Parts

From the numerical results, the modification of vortex generator consists of two main sections: 1) two layers of enclosure with a chamber in between and 2) two supporting frames for glass windows. Flow is translated vertically through the fan, travels radially outward through the horizontal duct. Curved fins are placed on the top of enclosure (lid) to create the vorticity. Flow with strong vorticity then travels downward through the vertical duct. The kinematic structure of dust devils is formed within the inflow region. Based on the above ideas, a modified vortex generator is designed. The structural drawings of the new vortex generator are attached in Appendix B. However, some relevant structures have to be calculated in advance for safety issues. After the construction, a stereo particle image velocimetry (SPIV) is used to study the characteristics of the vortex flow by measuring the flow field.

A.1 Windows

The material for the enclosure windows to allow for SPIV measurement was decided to be polycarbonate. Polycarbonate sheet offers high light transmittance rate of approximately 90%. The selected of the polycarbonate sheet has the thickness of 3 mm that can be easily fit around the cylinder frame and maintain optical clarity due to its flexibility. When the light travels through the polycarbonate sheets, the refraction may change its angle because the speed of light changes between two different media. The differential ratio is defined as refractive index, which is approximately 1.5 between

air and polycarbonate sheet. As a result, the light may be offset a certain distance. Figure A.1 indicates this phenomenon.

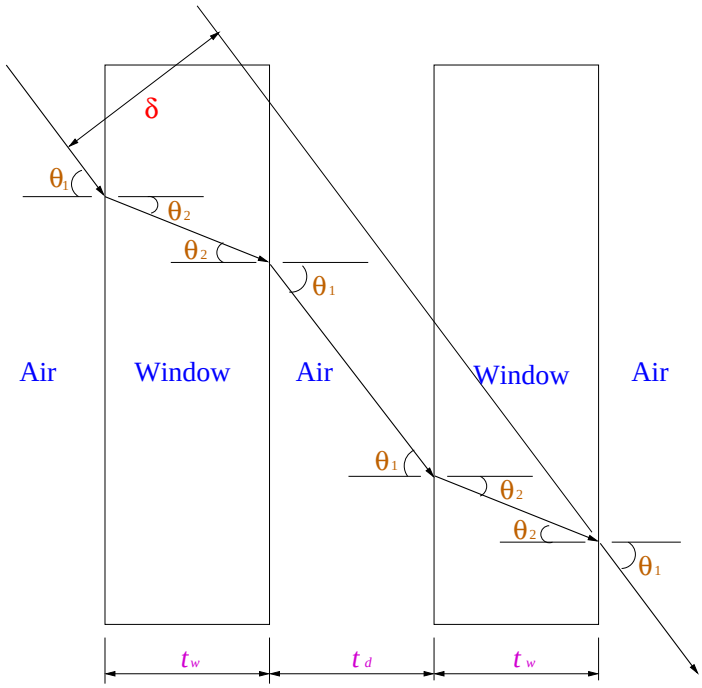

Figure A.1: Refraction of light through the glass.

The refraction angle θ_2 in the polycarbonate sheet can be calculated using:

$$n_{air} \sin\theta_1 = n_{window} \sin\theta_2 \tag{A.1}$$

where n_{air} and n_{window} are the refractive indices for air and polycarbonate sheets, respectively. The total offset distance δ can be then determined as:

$$\delta = 2 \times t_w(\tan\theta_1 - \tan\theta_2) \tag{A.2}$$

where t_w and t_d are the thickness of the polycarbonate sheet and the duct, respectively. Theoretically, the initial angle θ_1 of 0° is always desired. In practice, that perfect angle may be difficult to achieve, thus the refraction analysis is used to determine the effective refractive rate in the experiment. A maximum angle of θ_1 of 5° is assumed, because any angle greater than this value would be obvious during the alignment procedure of laser sheet. As a result, the maximum refractive angle is expected to be 3.33° through the polycarbonate sheets and the maximum offset distance is expected

to be 0.2mm. Moreover, the effect of refraction is negligible in this experiment. The light distortion due to the curvature of polycarbonate sheets is also neglected because the radii of the cylinder are very large comparing to their thickness.

A.2 Structural analysis

Safe environment for the experiment is required. A complete experimental set-up of vortex generator may be very heavy. Further, the vibration may cause the failure of the relevant structures in the vortex generator design. To prevent the danger in the design, the safety factors of hollow supporting bars and beams are evaluated.

- Hollow supporting bars

  To analyze the strength of hollow supporting bar, the problem can be simply stated in Figure A.2. In this design, hollow steel bars are selected and the properties are defined:

  1. Yield strength of structural steel: σ_{max}=250 MPa.
  2. Density of structural steel: D=7,850 kg m^{-3}.
  3. Outer radius of the hollow bar: R_o=10 mm.
  4. Inner radius of the hollow bar: R_i=7.5 mm.
  5. The lengths in Figure A.2: $L1$=150 mm, $L2$=150 mm, $L3$=265 mm and L_{bar}=1,130 mm.
  6. Estimated volume of the hollow bar: V_{bar} ≈155,312 mm^3.
  7. Weight of hollow support bar: W_{bar} ≈1.22 kg.

  – Failure by excessive elastic deflection:

  Moment of inertia can be calculated using

$$I = \frac{\pi}{4}(R_o^4 - R_i^4). \tag{A.3}$$

  Maximum moment allowed for elastic deflection is determined by

$$M_e = \frac{\sigma_{max}\ I}{c} \tag{A.4}$$

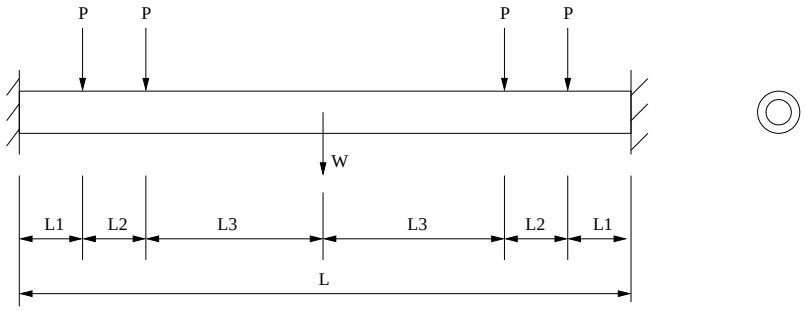

Figure A.2: A structure view of hollow supporting bar.

where c is equal to R_0 in this calculation. The results of moment of inertia and maximum moment are 5,368.9 mm^4 and 134,222.5 N mm, respectively. Assuming the weight of the apparatus is distributed into four points uniformly and the maximum moment occurs at the center point of the bar as shown in Figure A.3, maximum load allowed is determined by the following calculations.

$$\Sigma M = 0 \tag{A.5}$$

$$M_e = -265P - 415P + 565 \times (\frac{W}{2} + 2P) \tag{A.6}$$

$$M_e = 450P + 282.5W \tag{A.7}$$

$$P = \frac{134222.5 \text{ N mm} - 282.5 \text{ mm} \times 11.97 \text{ N}}{450 \text{ mm}} \tag{A.8}$$

$$P = 29.6 \text{ kg} \tag{A.9}$$

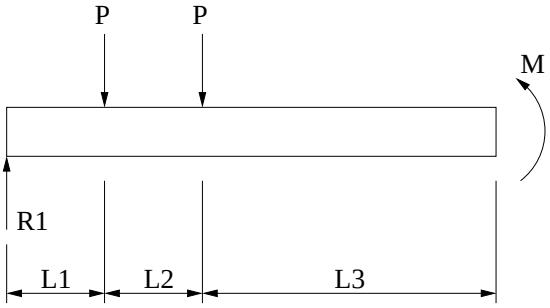

Figure A.3: A schematic of force and momentum analysis for hollow supporting bar.

Two hollow steel bars are used to hold the vortex generator. Maximum weight of the vortex generator allowed is found to be 236.8 kg before the

failure by excessive elastic deflection. Total estimated weight of vortex generator is less than 100 kg. Hence, the safety factor (SF) is greater than 2.36.

– Failure by fracture

Maximum moment allowed for fracture is determined by

$$M_p = 2[\sigma_{max}(\frac{\pi R_o^2}{2})(\frac{4R_o}{3\pi})] - 2[\sigma_{max}(\frac{\pi R_i^2}{2})(\frac{4R_i}{3\pi})]. \quad \text{(A.10)}$$

Similarly, the maximum load allowed and maximum weight of vortex generator allowed can be determined to be 42.9 kg and 343.2 kg, respectively. Consequently, the safety factor for fracture is 3.43. The structure analysis of the hollow bar shows that the failure by excessive elastic deflection allows weight less than that for the failure by fracture. This agrees with the material behavior of structure steel.

- Hollow supporting beams

To analyze the strength of hollow supporting beam with the circular holes, the problem can be simply stated in Figure A.4. Force acting on the holes within the small width of hollow square beams may cause the structure failure. The properties of hollow supporting beam are defined by the following:

1. Hole radius: R_h=10 mm.
2. Dimensions: t_1=32mm and t_2=38.1 mm.
3. Total length of beam: L=1,000 mm.
4. Estimated volume of the hollow beam: V_{beam} ≈427,610 mm^3.
5. Estimated weight of the hollow beam: W_{beam} ≈3.36 kg.

From the structure view point the minimum moment of inertia is found to be 3,554.74 mm^4. Maximum moment allowed is estimated to be 98,197.2 N mm. It should be noted that c is 9.05 mm in Equation (A.4). Generally, the maximum moment occurs at the center of the beam, as shown in Figure A.5. Maximum load allowed and safety factor are calculated to be 36.7 kg and 1.47, respectively.

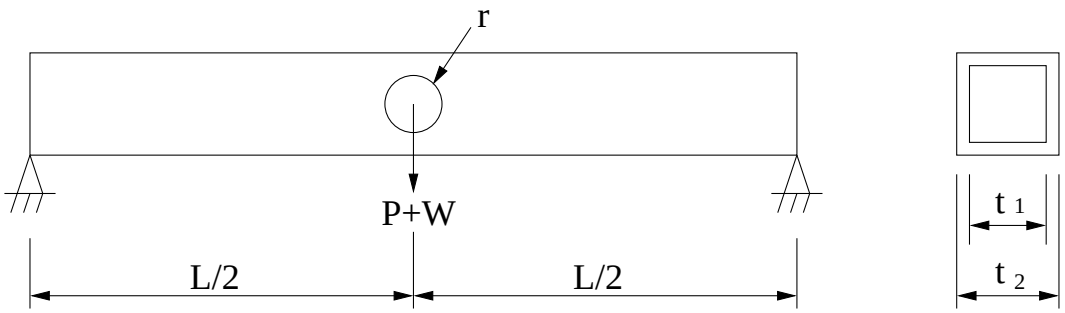

Figure A.4: A structure view of hollow supporting beam.

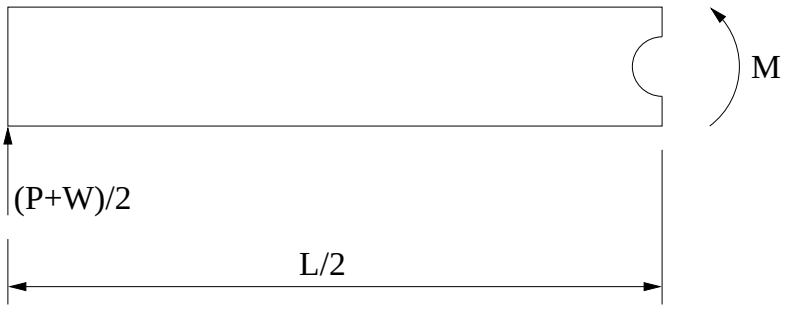

Figure A.5: A schematic of force and momentum analysis for hollow supporting beam.

Appendix B

Design Drawings for Vortex Generator

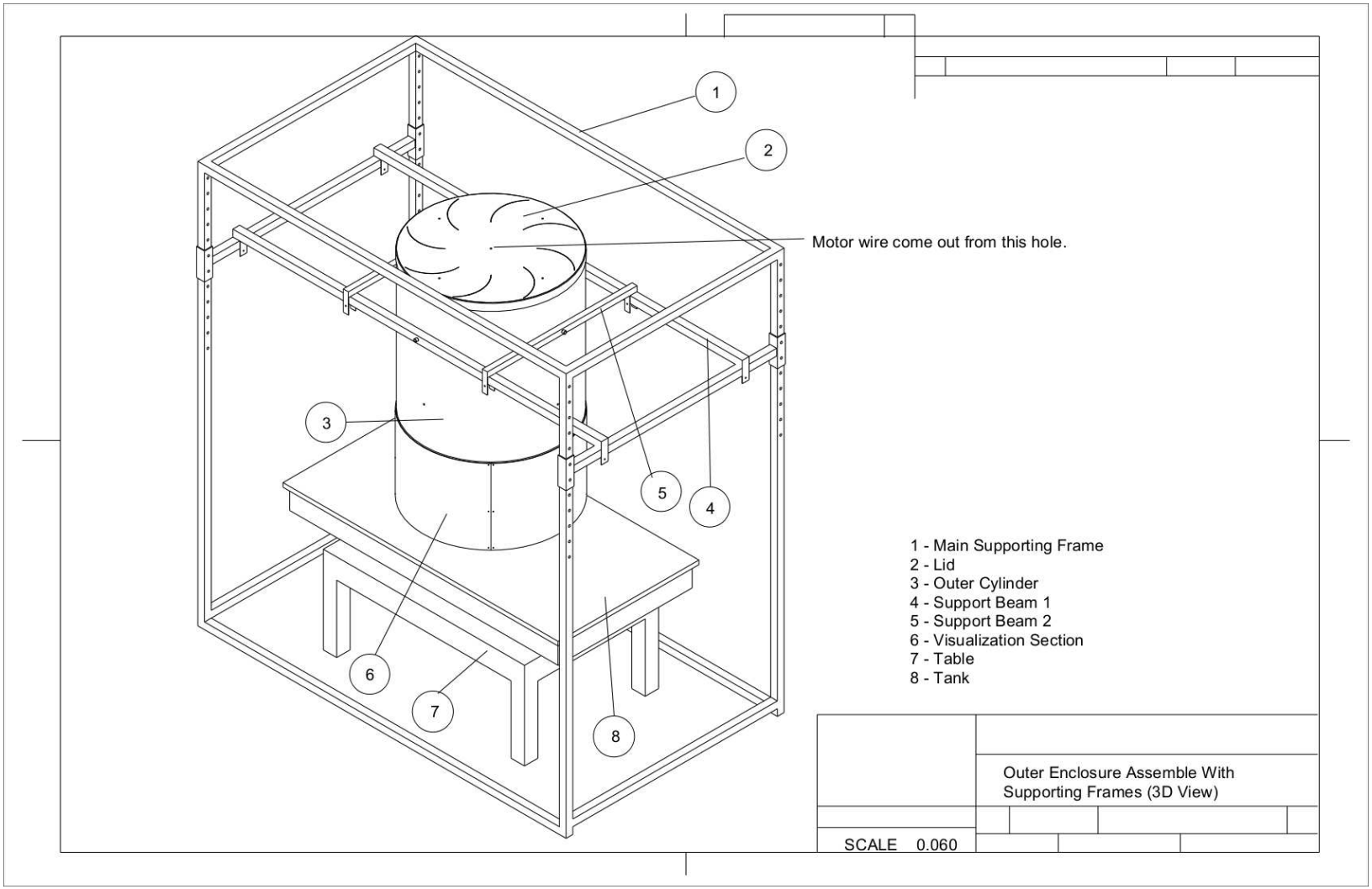
1
2
Motor wire come out from this hole.
3
5
4
6
7
8
1 - Main Supporting Frame
2 - Lid
3 - Outer Cylinder
4 - Support Beam 1
5 - Support Beam 2
6 - Visualization Section
7 - Table
8 - Tank
Outer Enclosure Assemble With
Supporting Frames (3D View)
SCALE 0.060

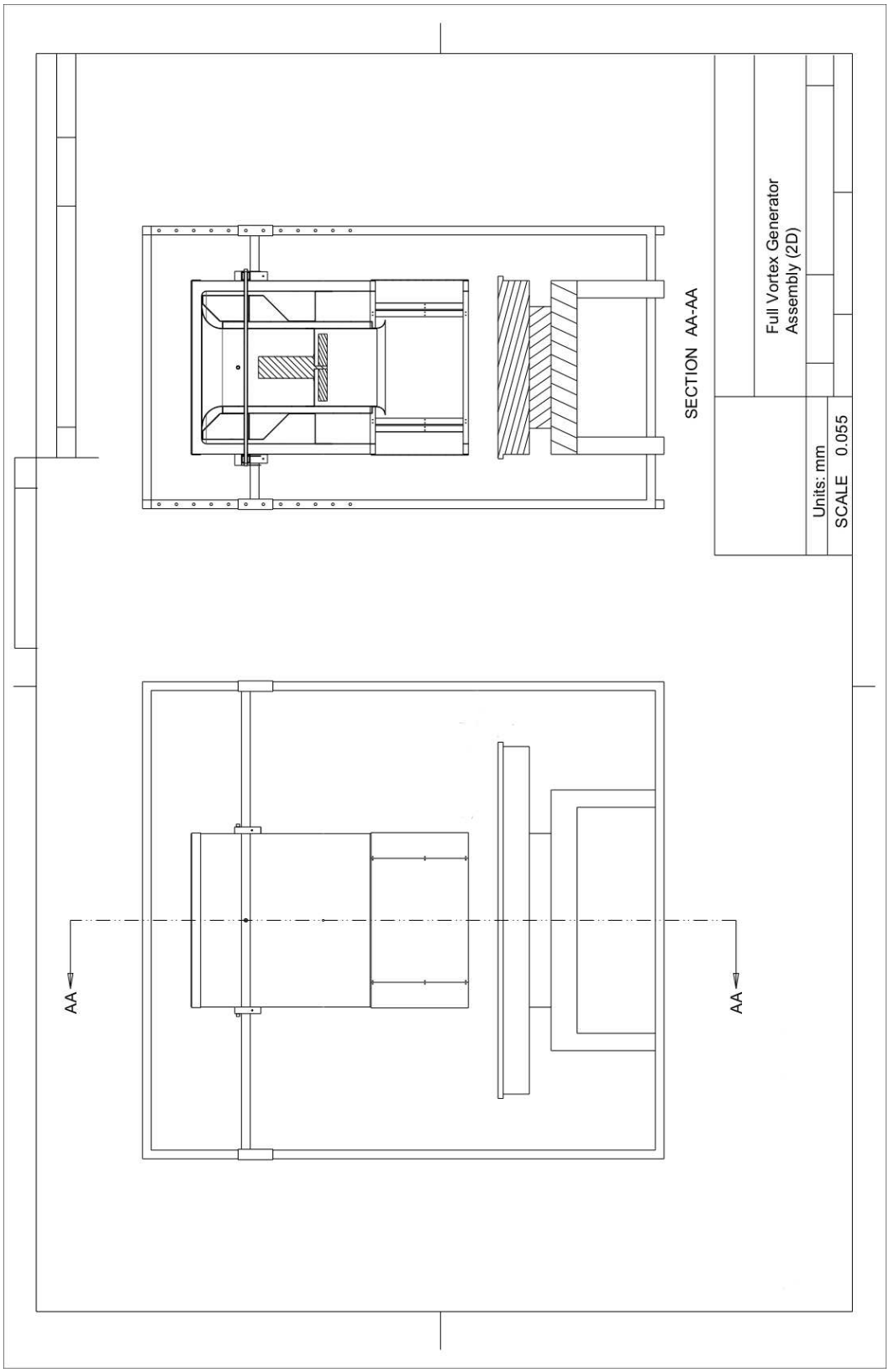
SECTION AA-AA
Full Vortex Generator
Assembly (2D)
Units: mm
SCALE 0.055
AA
AA

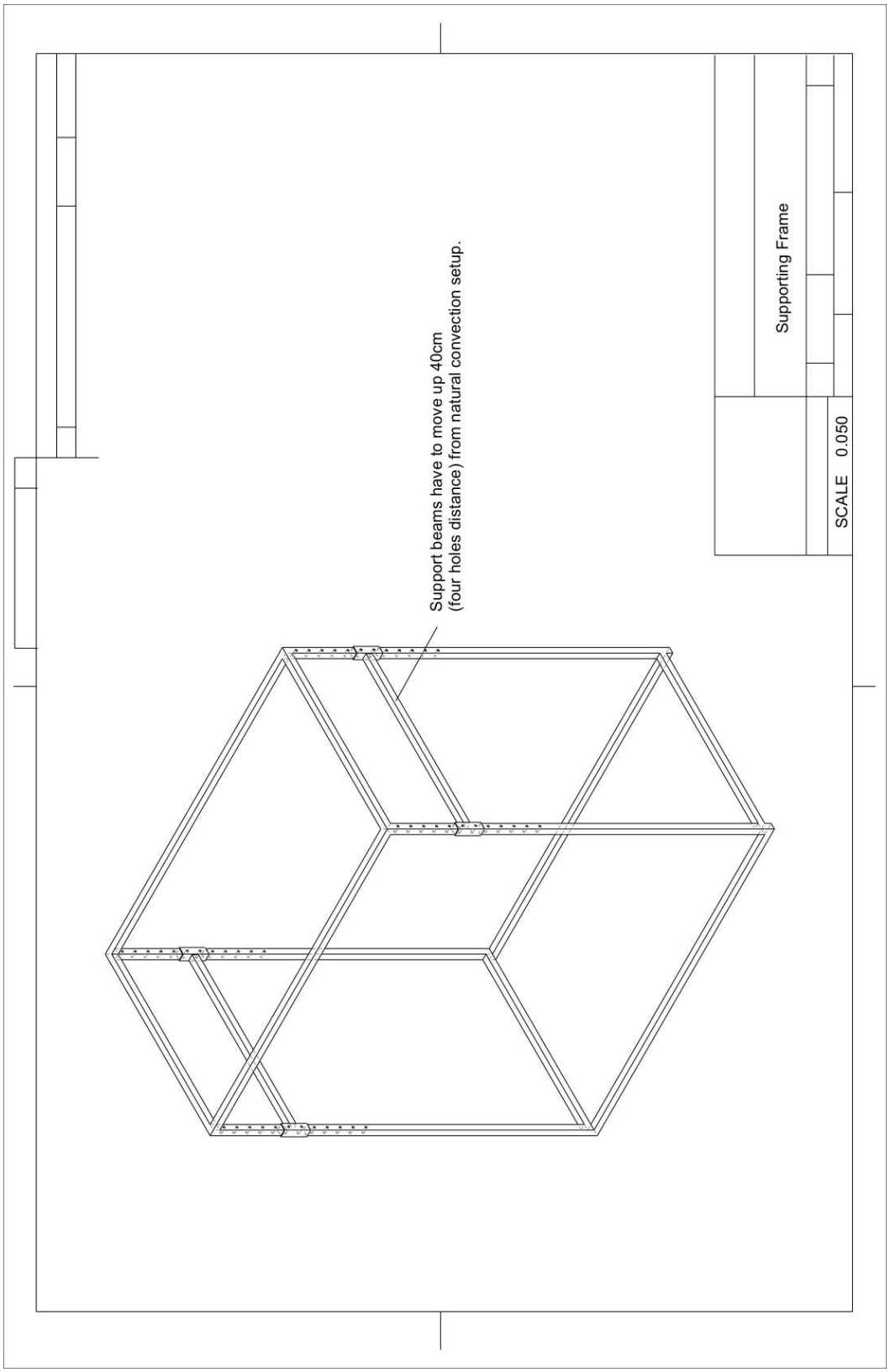
Supporting Frame
SCALE 0.050
Support beams have to move up 40cm
(four holes distance) from natural convection setup.

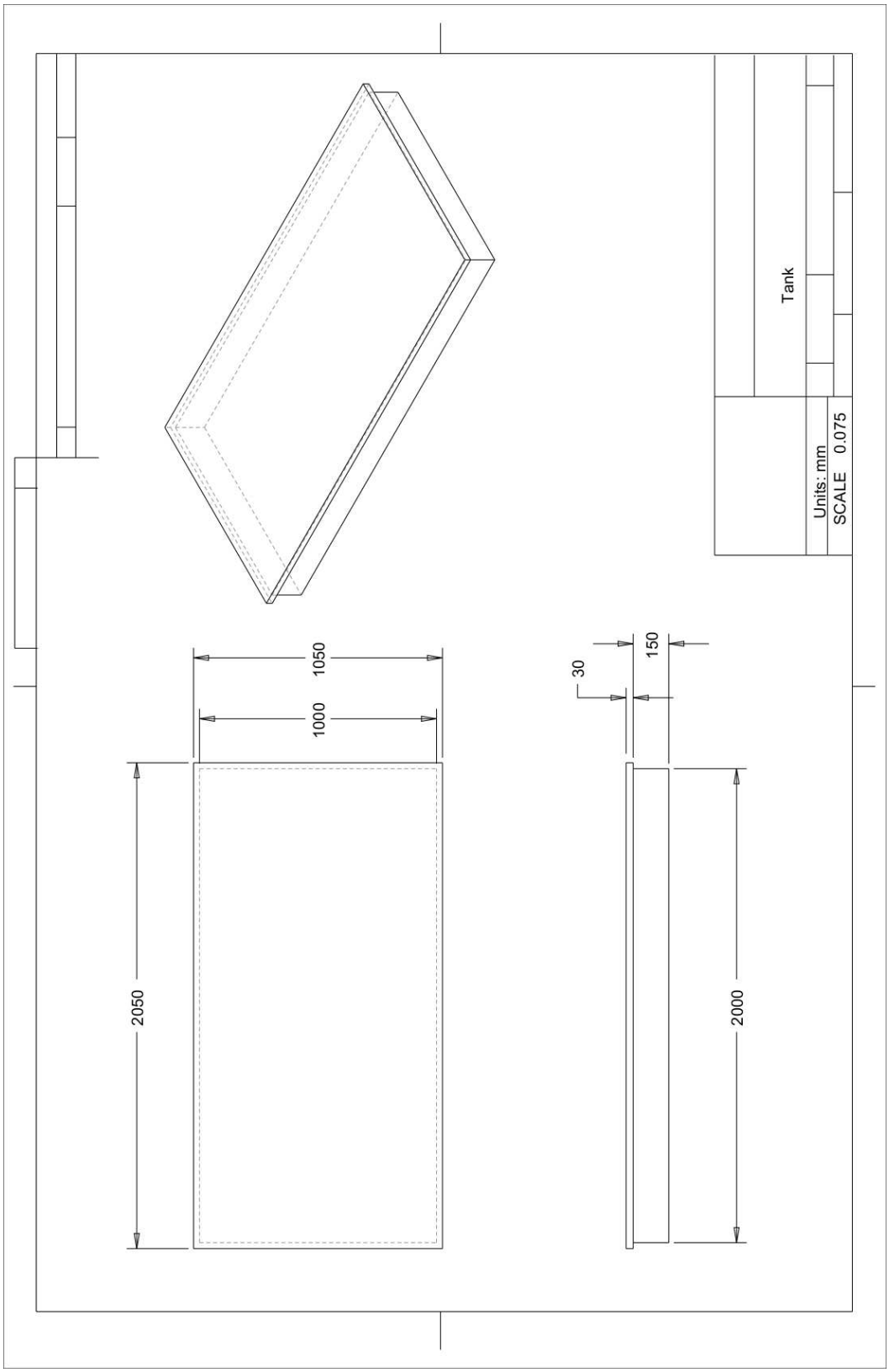
Tank
Units: mm
SCALE 0.075
1050
1000
2050
30
150
2000

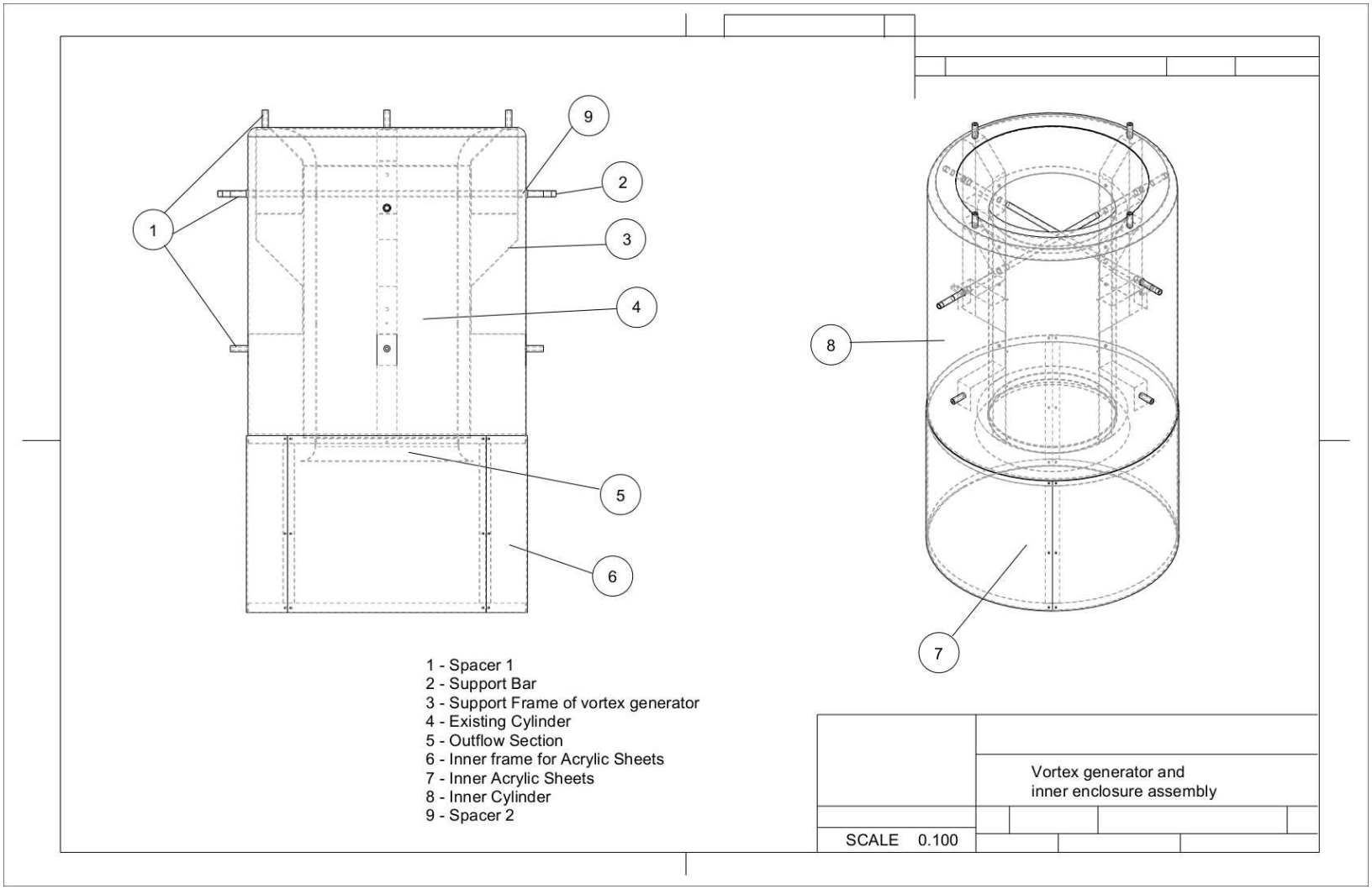
9
2
1
3
4
8
5
6
7
1 - Spacer 1
2 - Support Bar
3 - Support Frame of vortex generator
4 - Existing Cylinder
5 - Outflow Section
6 - Inner frame for Acrylic Sheets
7 - Inner Acrylic Sheets
8 - Inner Cylinder
9 - Spacer 2
Vortex generator and
inner enclosure assembly
SCALE 0.100

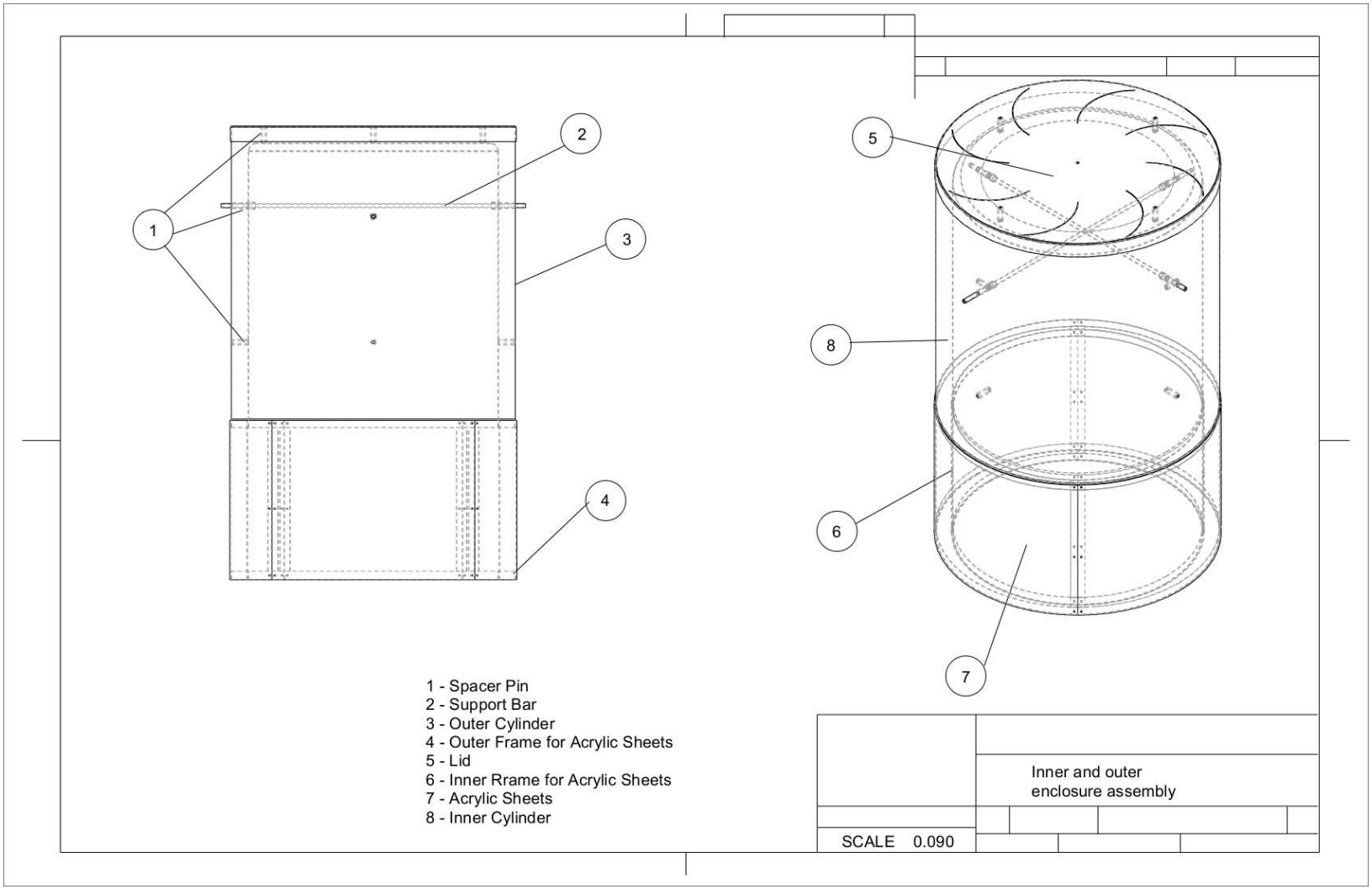
1
2
3
4
5
6
7
8
1 - Spacer Pin
2 - Support Bar
3 - Outer Cylinder
4 - Outer Frame for Acrylic Sheets
5 - Lid
6 - Inner Rrame for Acrylic Sheets
7 - Acrylic Sheets
8 - Inner Cylinder
Inner and outer
enclosure assembly
SCALE 0.090

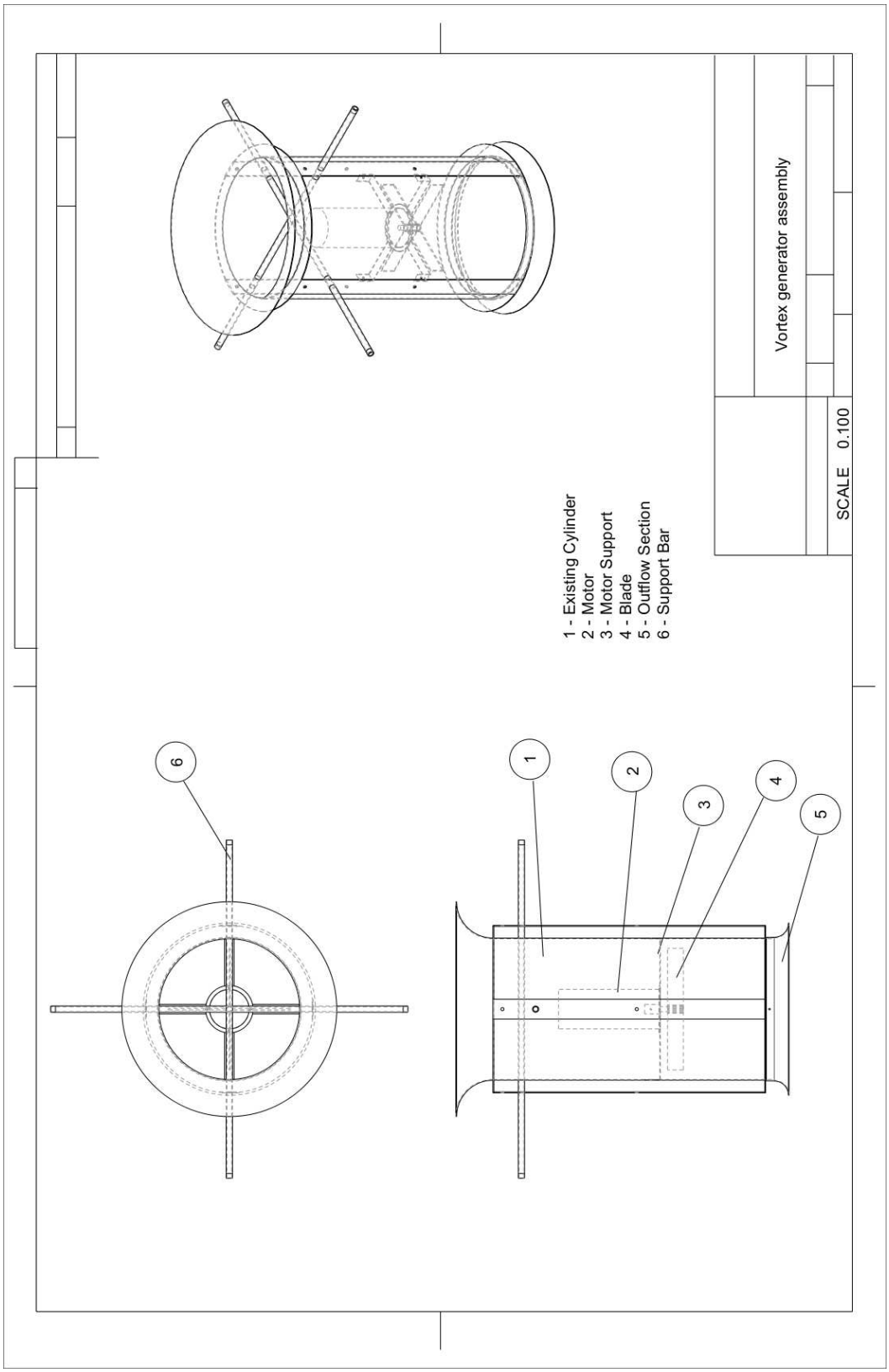
Vortex generator assembly
SCALE 0.100
1 - Existing Cylinder
2 - Motor
3 - Motor Support
4 - Blade
5 - Outflow Section
6 - Support Bar
1
2
3
4
5
6

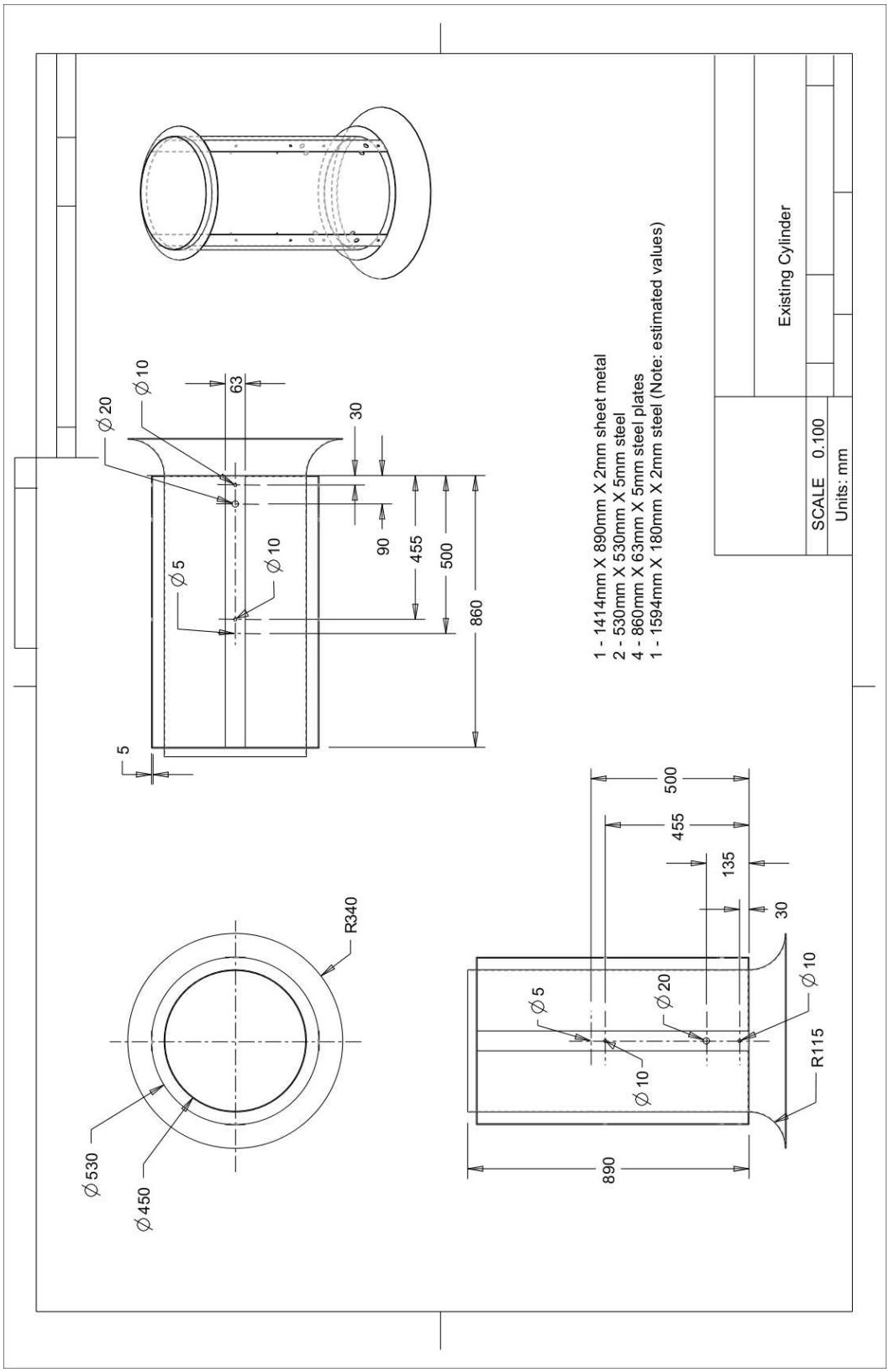
Existing Cylinder
SCALE 0.100
Units: mm
1 - 1414mm X 890mm X 2mm sheet metal
2 - 530mm X 530mm X 5mm steel
4 - 860mm X 63mm X 5mm steel plates
1 - 1594mm X 180mm X 2mm steel (Note: estimated values)
Ø 20
Ø 10
63
30
90
455
500
860
Ø 5
Ø 10
5
R340
Ø 530
Ø 450
500
455
135
30
Ø 5
Ø 20
Ø 10
Ø 10
R115
890

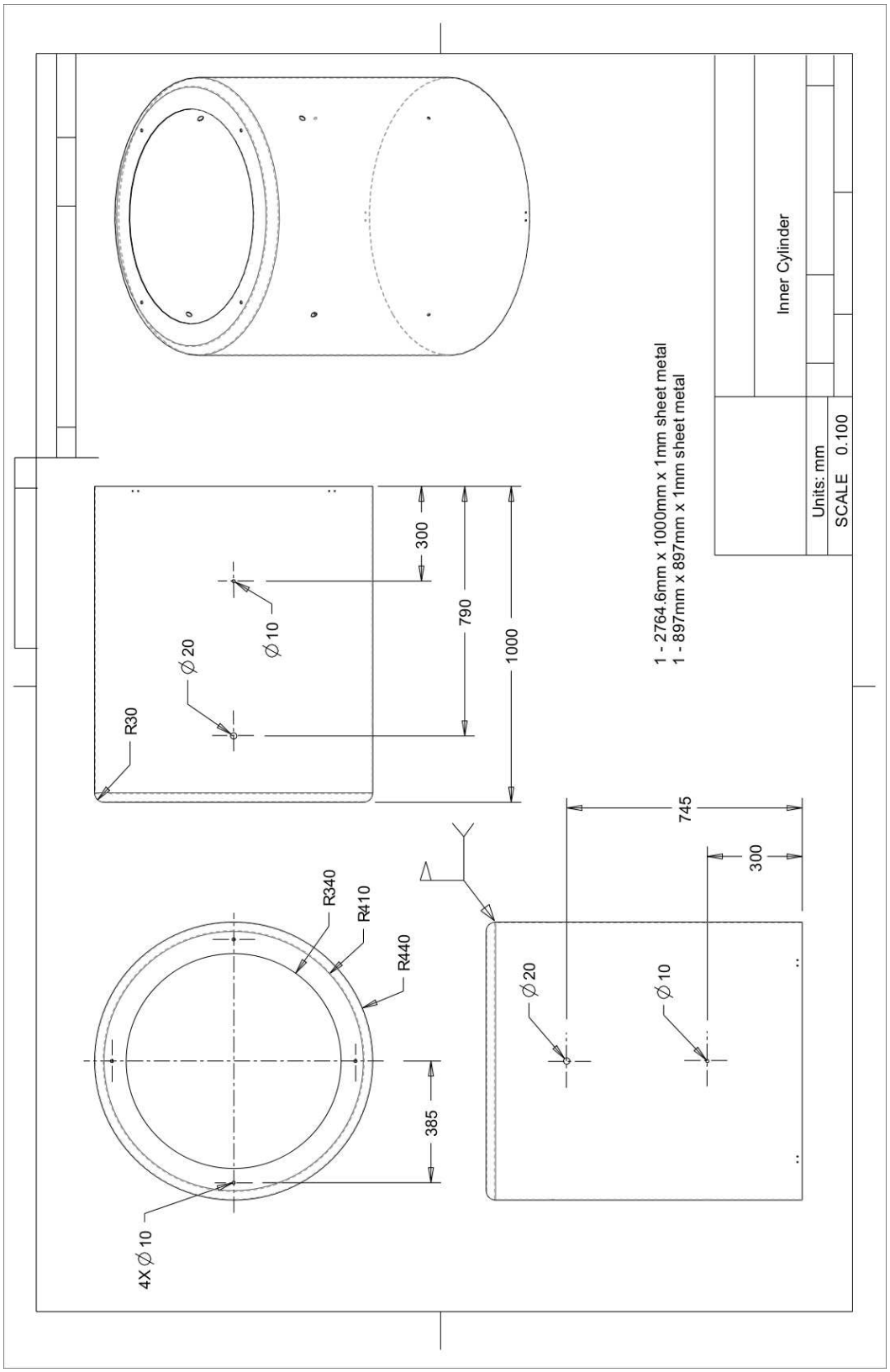
Inner Cylinder
Units: mm
SCALE 0.100
1 - 2764.6mm x 1000mm x 1mm sheet metal
1 - 897mm x 897mm x 1mm sheet metal
300
790
1000
R30
Ø20
Ø10
745
300
Ø20
Ø10
R340
R410
R440
385
4X Ø10

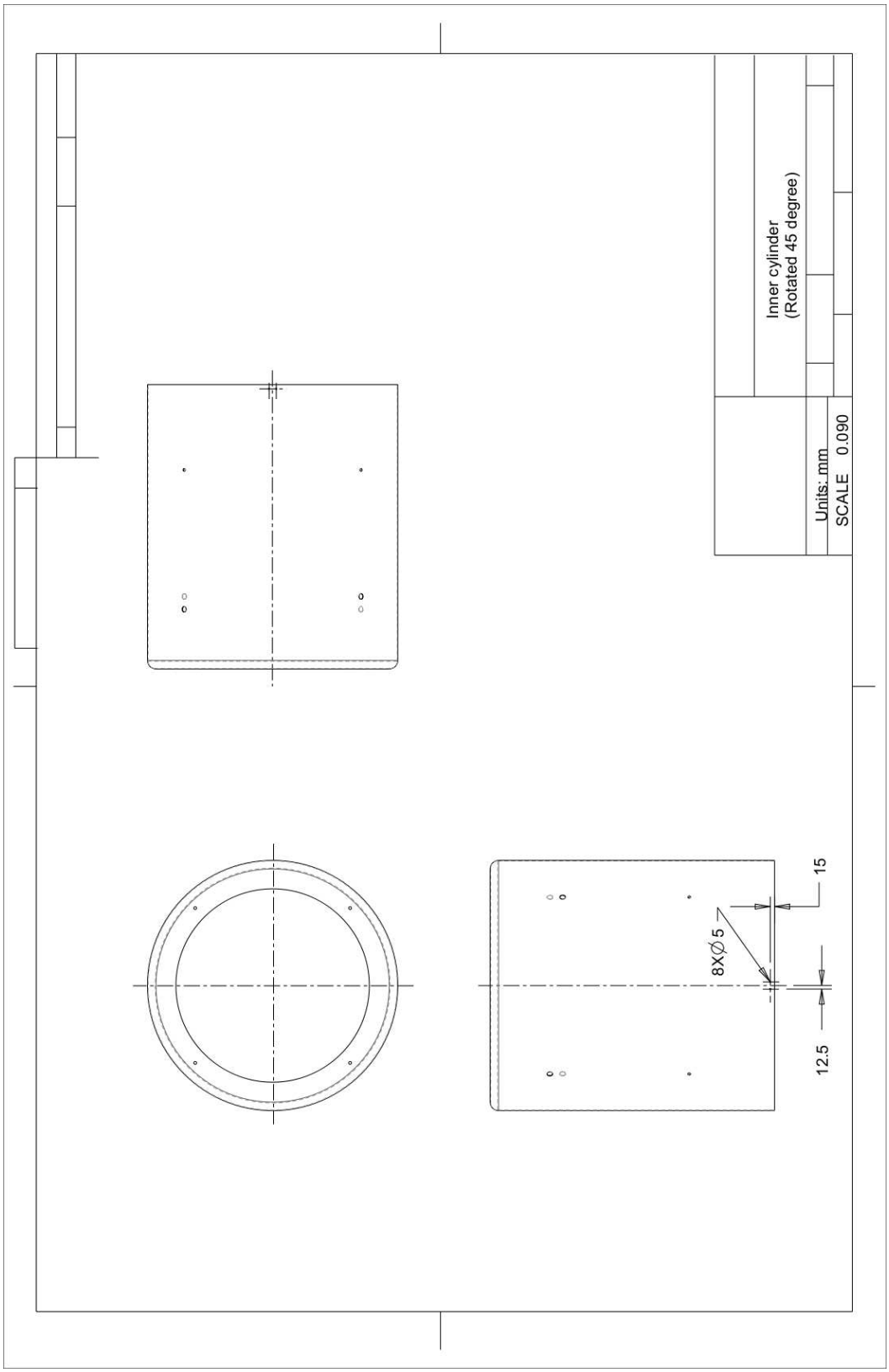
Inner cylinder
(Rotated 45 degree)
Units: mm
SCALE 0.090
8XØ5
15
12.5

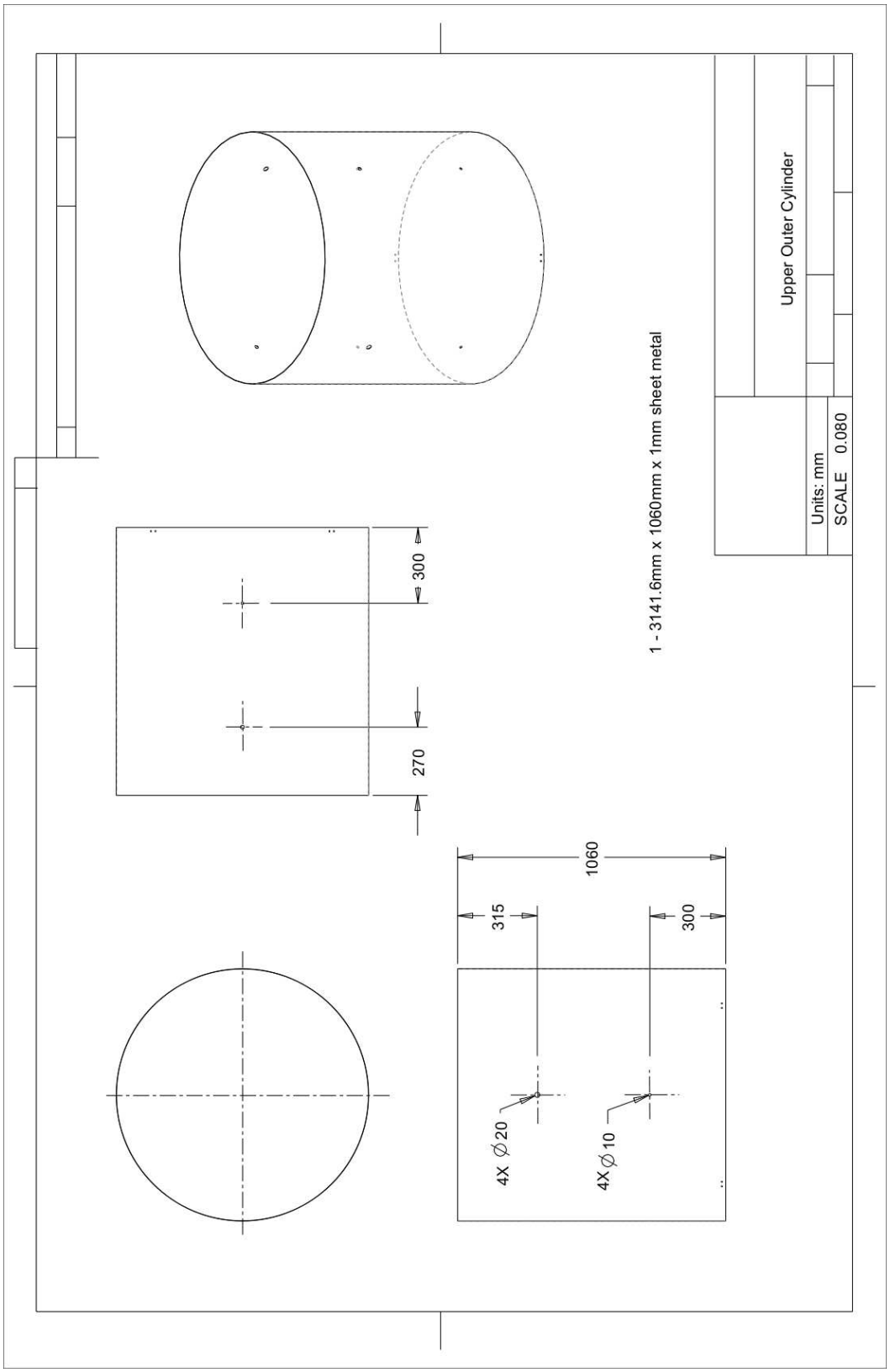
Upper Outer Cylinder
Units: mm
SCALE 0.080
1 - 3141.6mm x 1060mm x 1mm sheet metal
300
270
1060
315
300
4X ∅20
4X ∅10

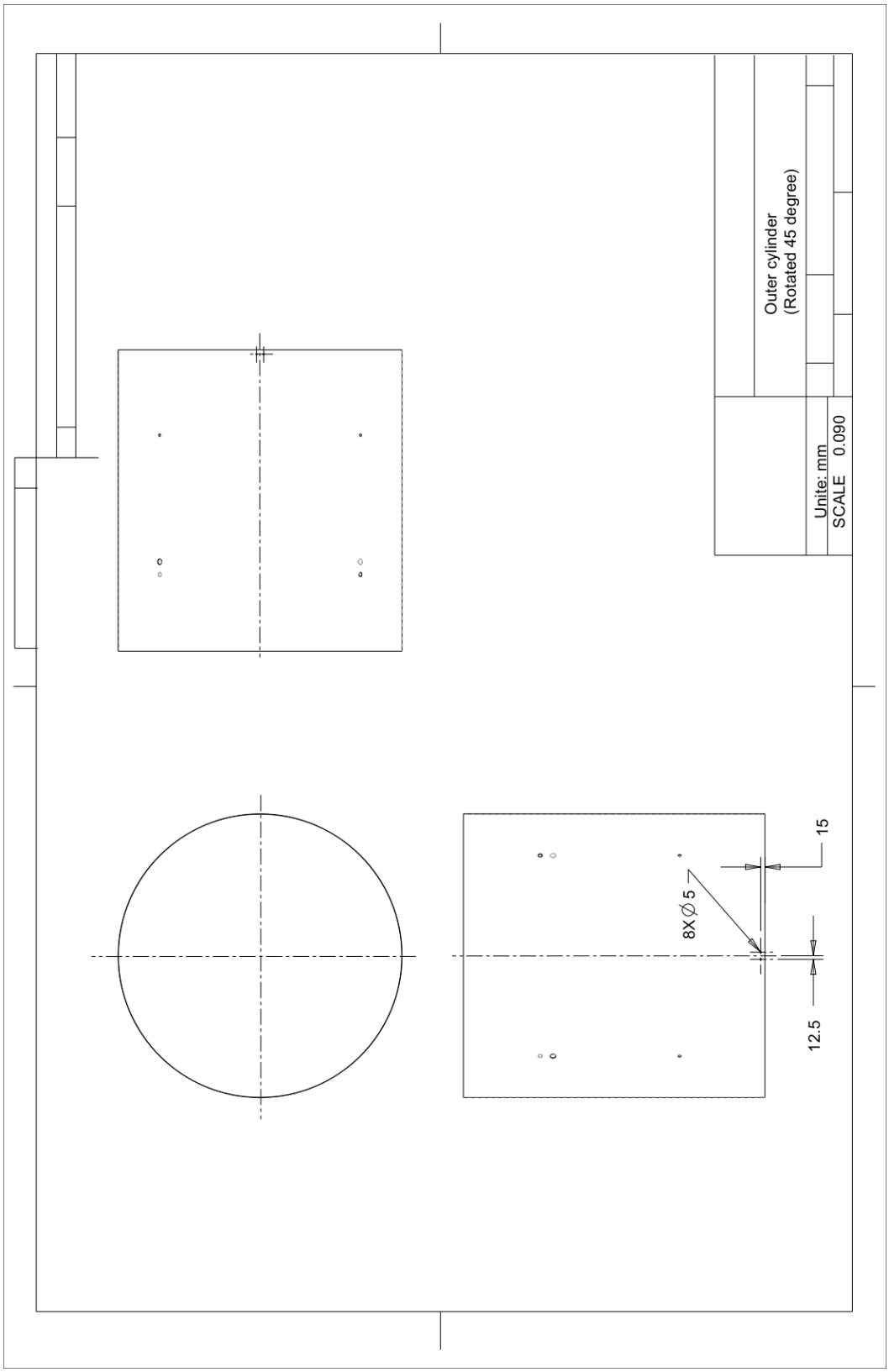
Outer cylinder
(Rotated 45 degree)
Unite: mm
SCALE 0.090
8X ∅5
15
12.5

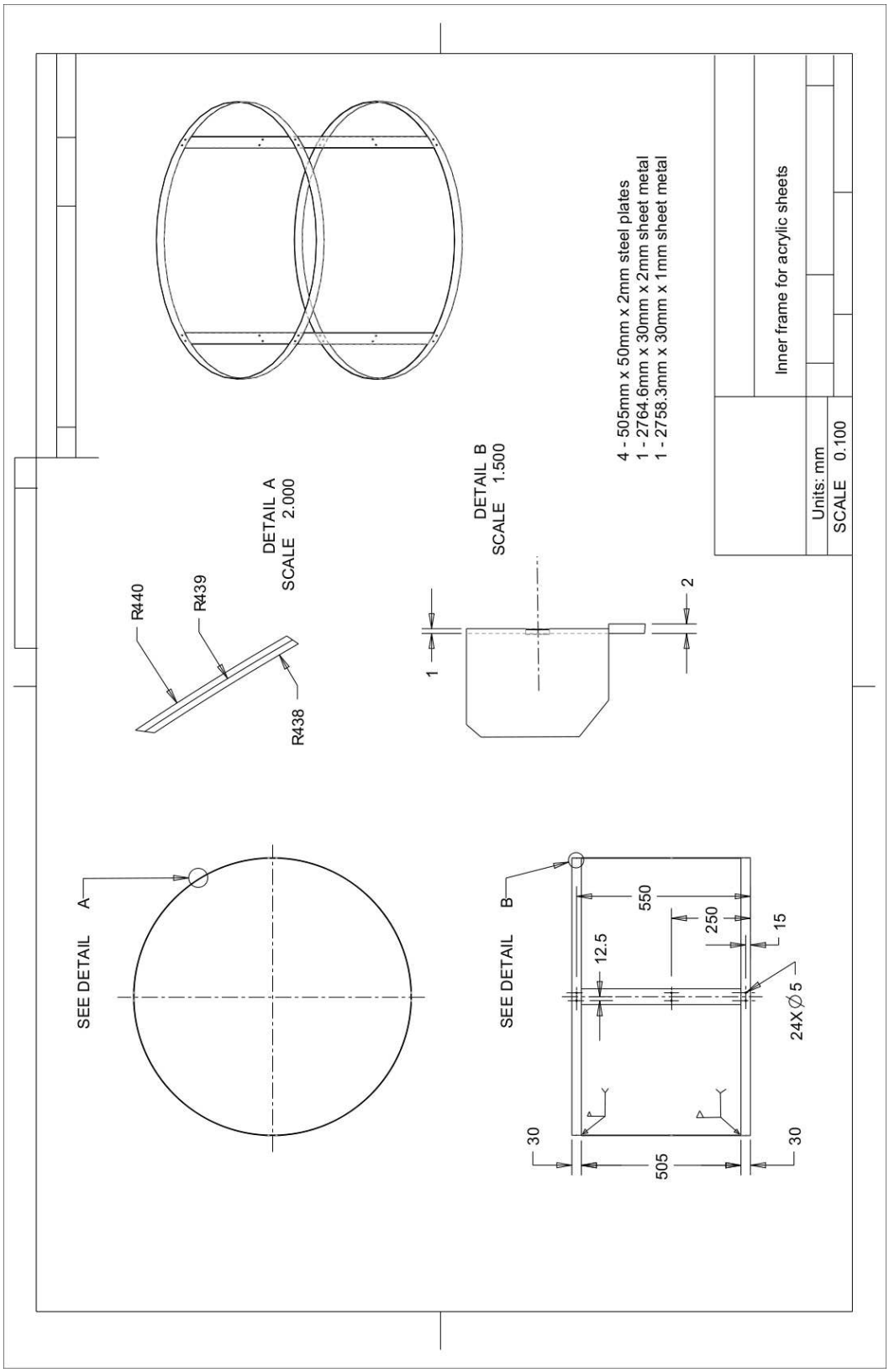
Inner frame for acrylic sheets
Units: mm
SCALE 0.100
4 - 505mm x 50mm x 2mm steel plates
1 - 2764.6mm x 30mm x 2mm sheet metal
1 - 2758.3mm x 30mm x 1mm sheet metal
DETAIL A
SCALE 2.000
R440
R439
R438
DETAIL B
SCALE 1.500
1
2
SEE DETAIL A
SEE DETAIL B
550
250
15
12.5
24X ∅5
30
505
30

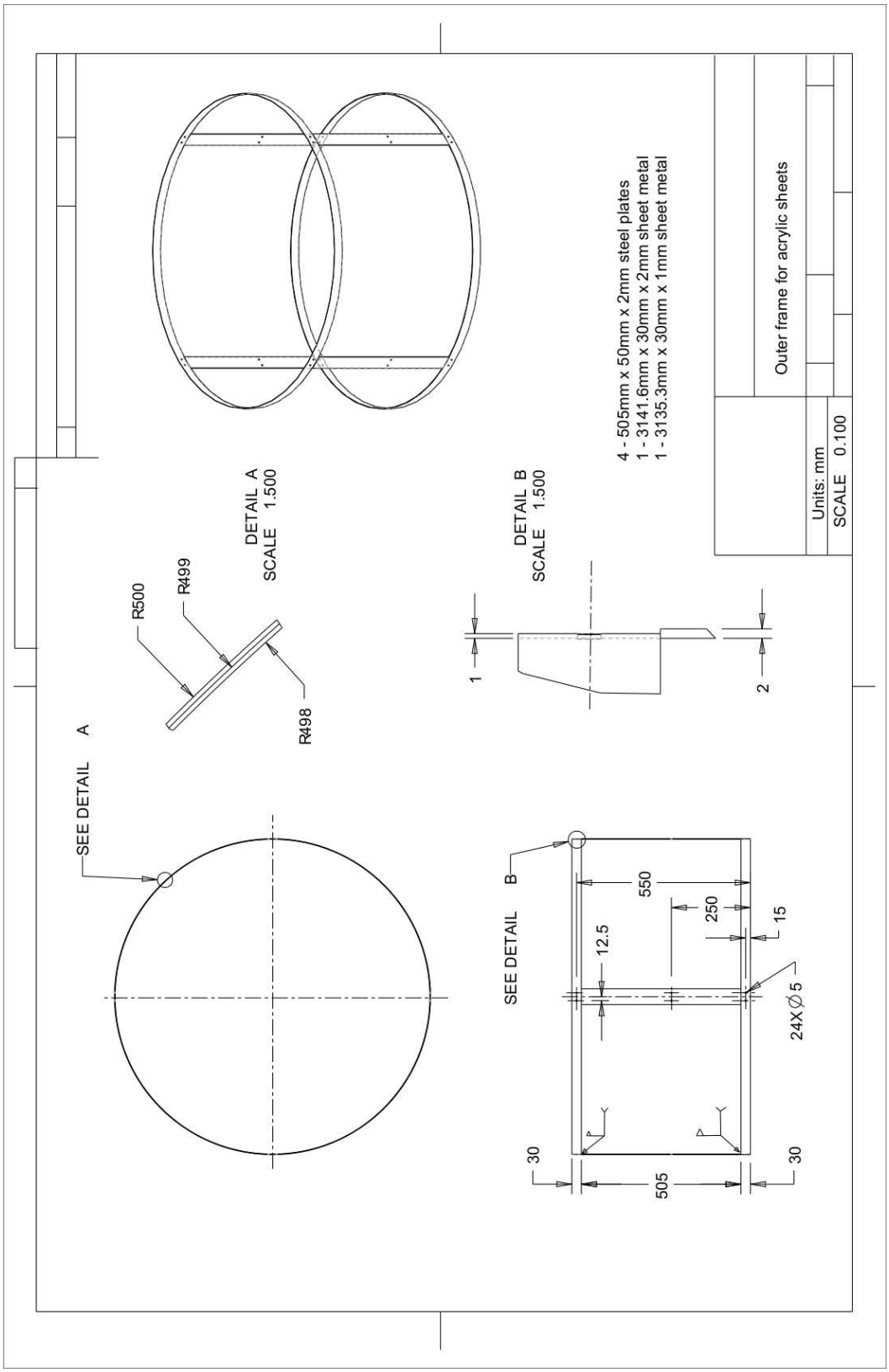
Outer frame for acrylic sheets
Units: mm
SCALE 0.100
4 - 505mm x 50mm x 2mm steel plates
1 - 3141.6mm x 30mm x 2mm sheet metal
1 - 3135.3mm x 30mm x 1mm sheet metal
DETAIL A
SCALE 1.500
R500
R499
R498
DETAIL B
SCALE 1.500
1
2
SEE DETAIL A
SEE DETAIL B
550
250
15
12.5
24X ∅5
30
505
30

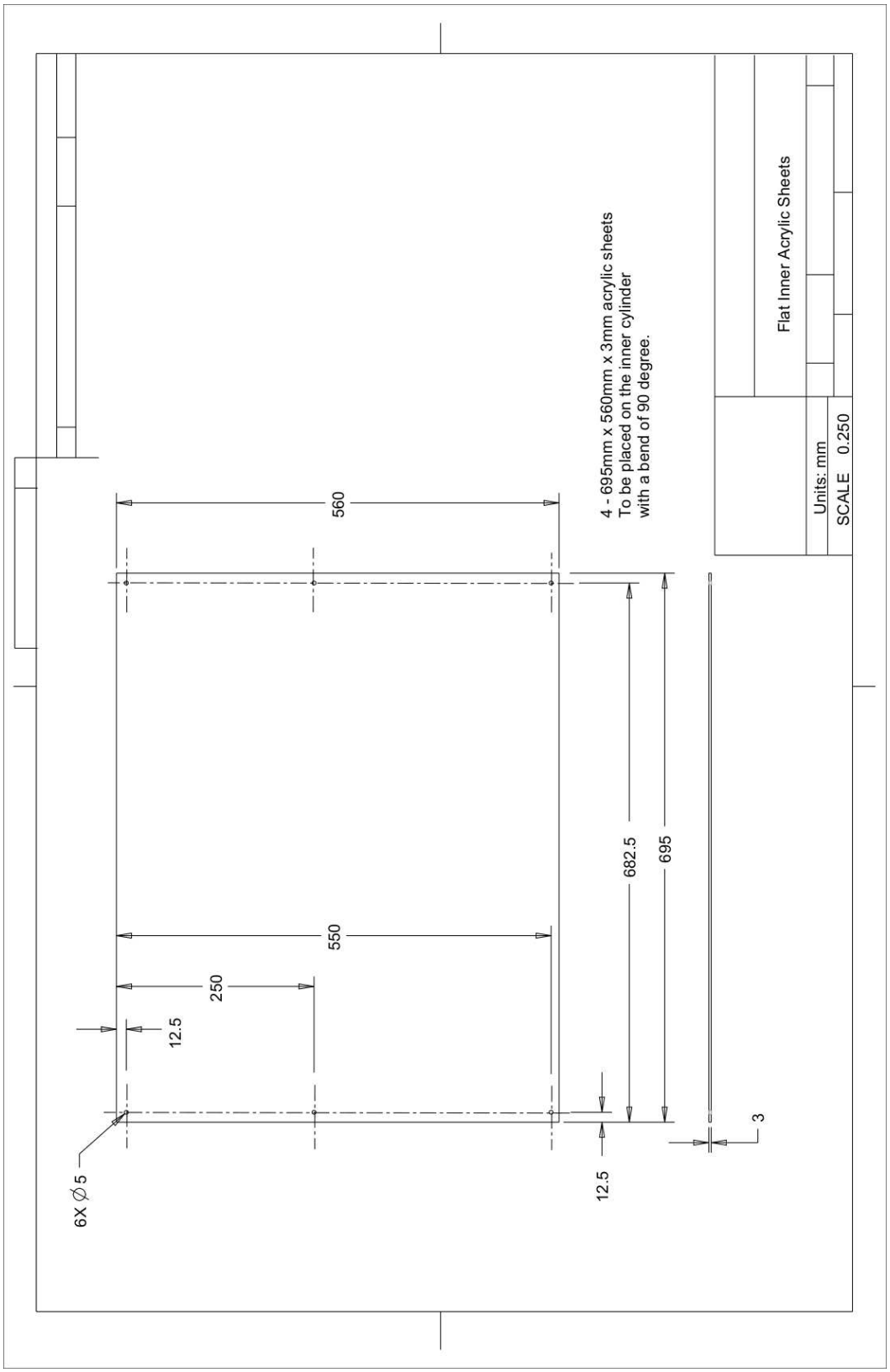
Flat Inner Acrylic Sheets
Units: mm
SCALE 0.250
4 - 695mm x 560mm x 3mm acrylic sheets
To be placed on the inner cylinder
with a bend of 90 degree.
560
550
250
12.5
682.5
695
12.5
3
6X ∅5

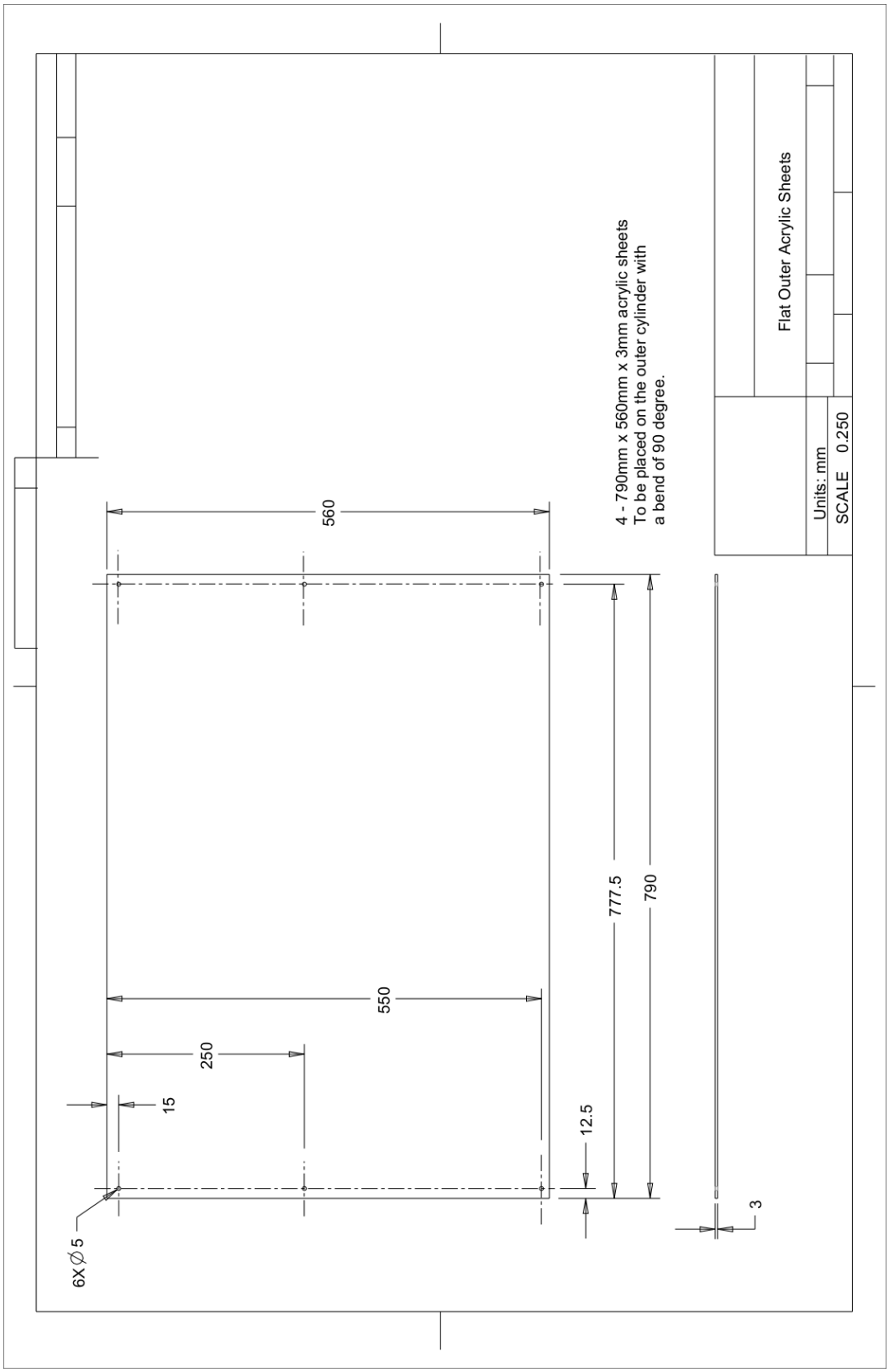
Flat Outer Acrylic Sheets
Units: mm
SCALE 0.250
4 - 790mm x 560mm x 3mm acrylic sheets
To be placed on the outer cylinder with
a bend of 90 degree.
560
550
250
15
6X ∅5
12.5
777.5
790
3

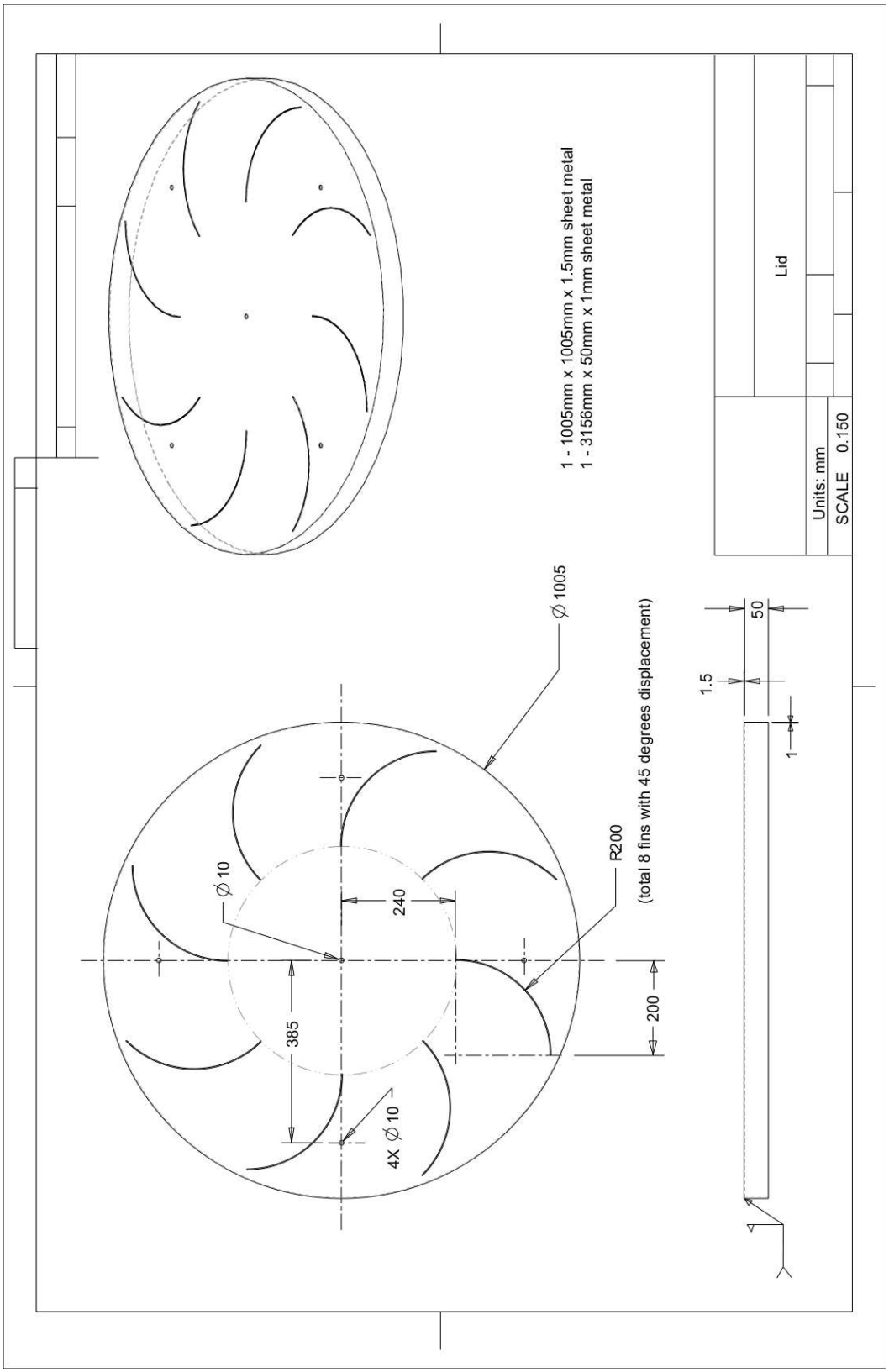
Lid
Units: mm
SCALE 0.150
1 - 1005mm x 1005mm x 1.5mm sheet metal
1 - 3156mm x 50mm x 1mm sheet metal
∅ 1005
R200
(total 8 fins with 45 degrees displacement)
∅ 10
240
385
200
4X ∅ 10
1.5
50
1

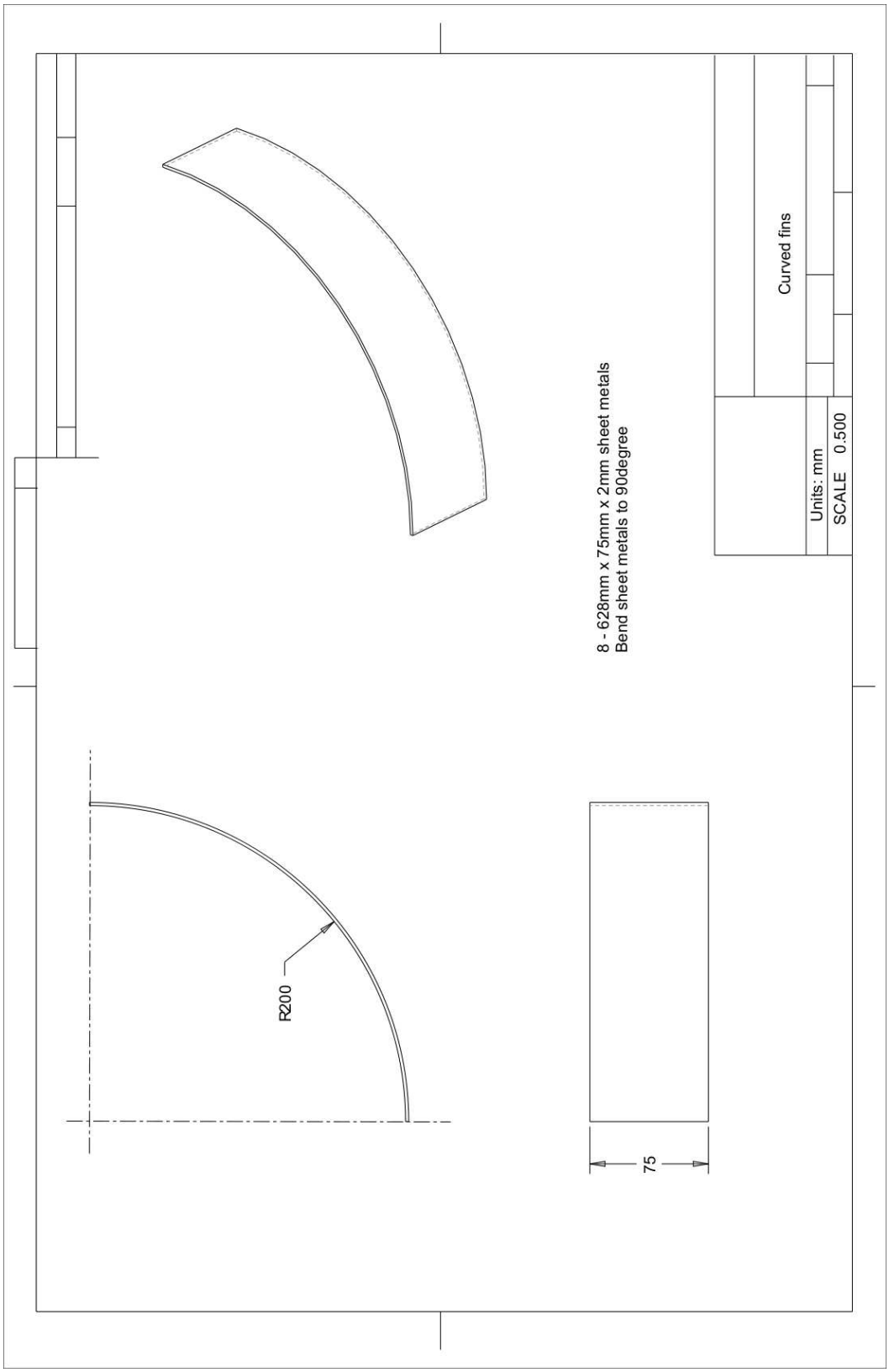
Curved fins
Units: mm
SCALE 0.500
8 - 628mm x 75mm x 2mm sheet metals
Bend sheet metals to 90degree
R200
75

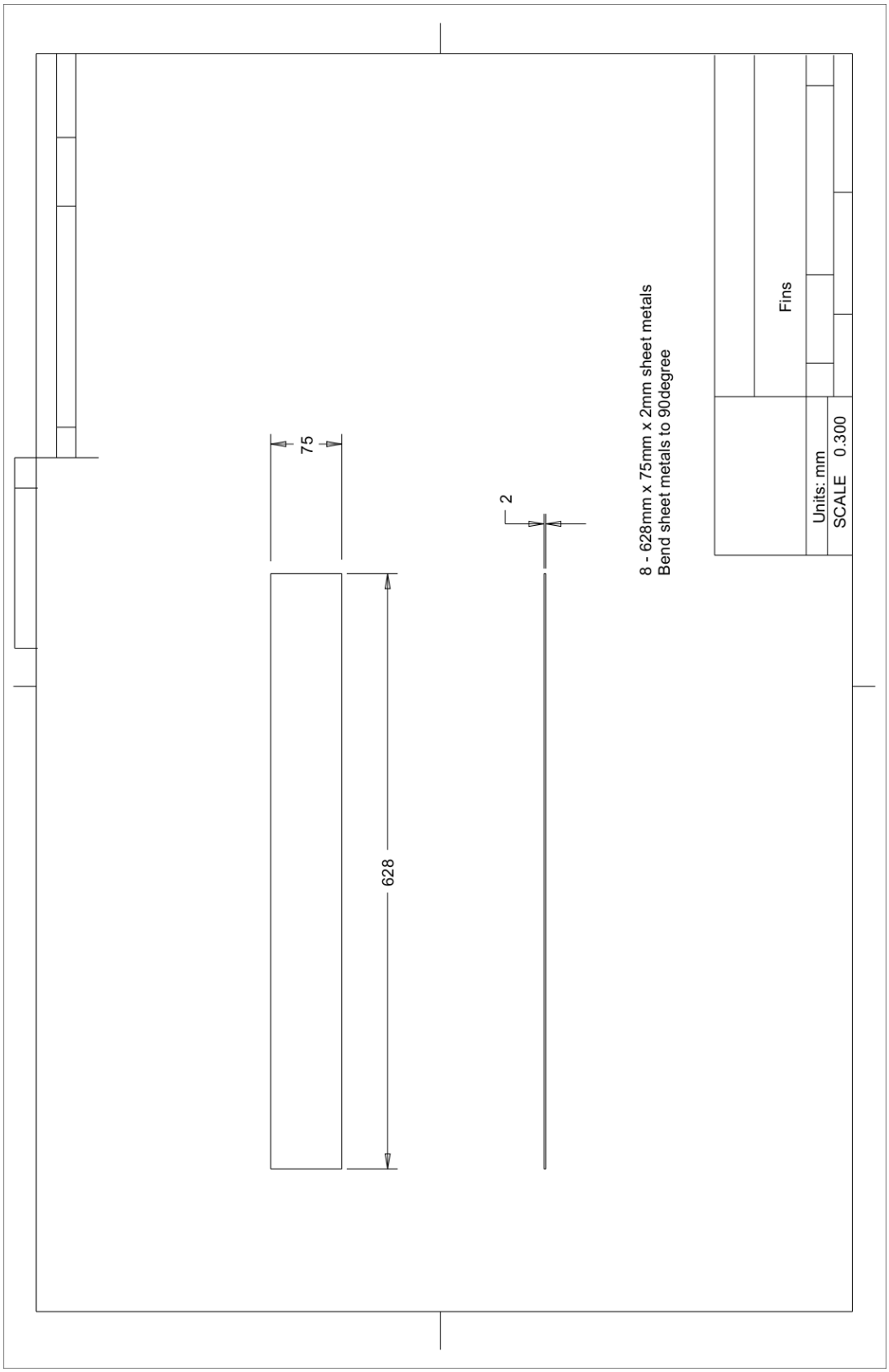
75
2
628
8 - 628mm x 75mm x 2mm sheet metals
Bend sheet metals to 90degree
Fins
Units: mm
SCALE 0.300

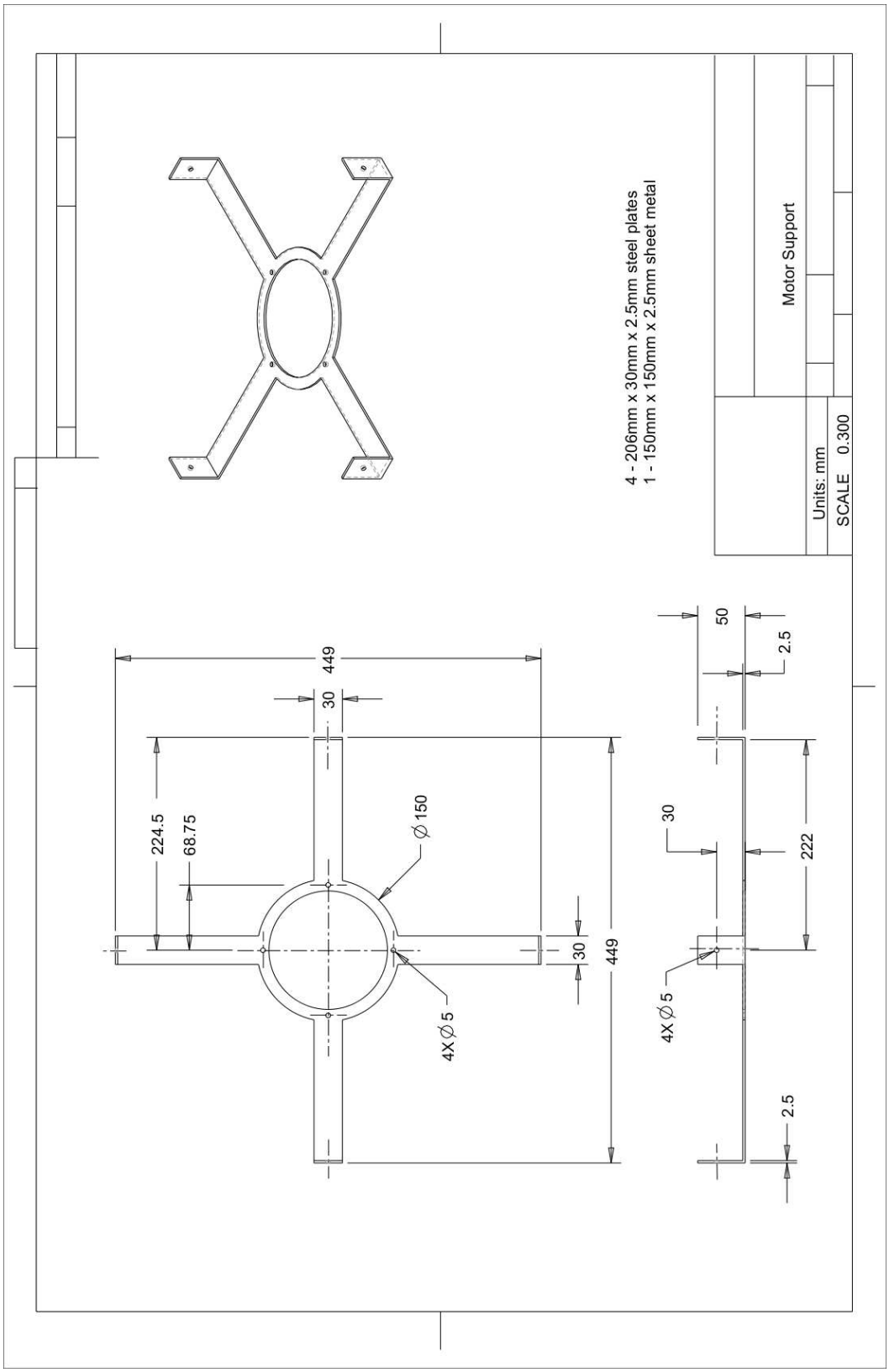
4 - 206mm x 30mm x 2.5mm steel plates
1 - 150mm x 150mm x 2.5mm sheet metal
Motor Support
Units: mm
SCALE 0.300
449
30
224.5
68.75
Ø150
4XØ5
30
449
50
2.5
30
222
4XØ5
2.5

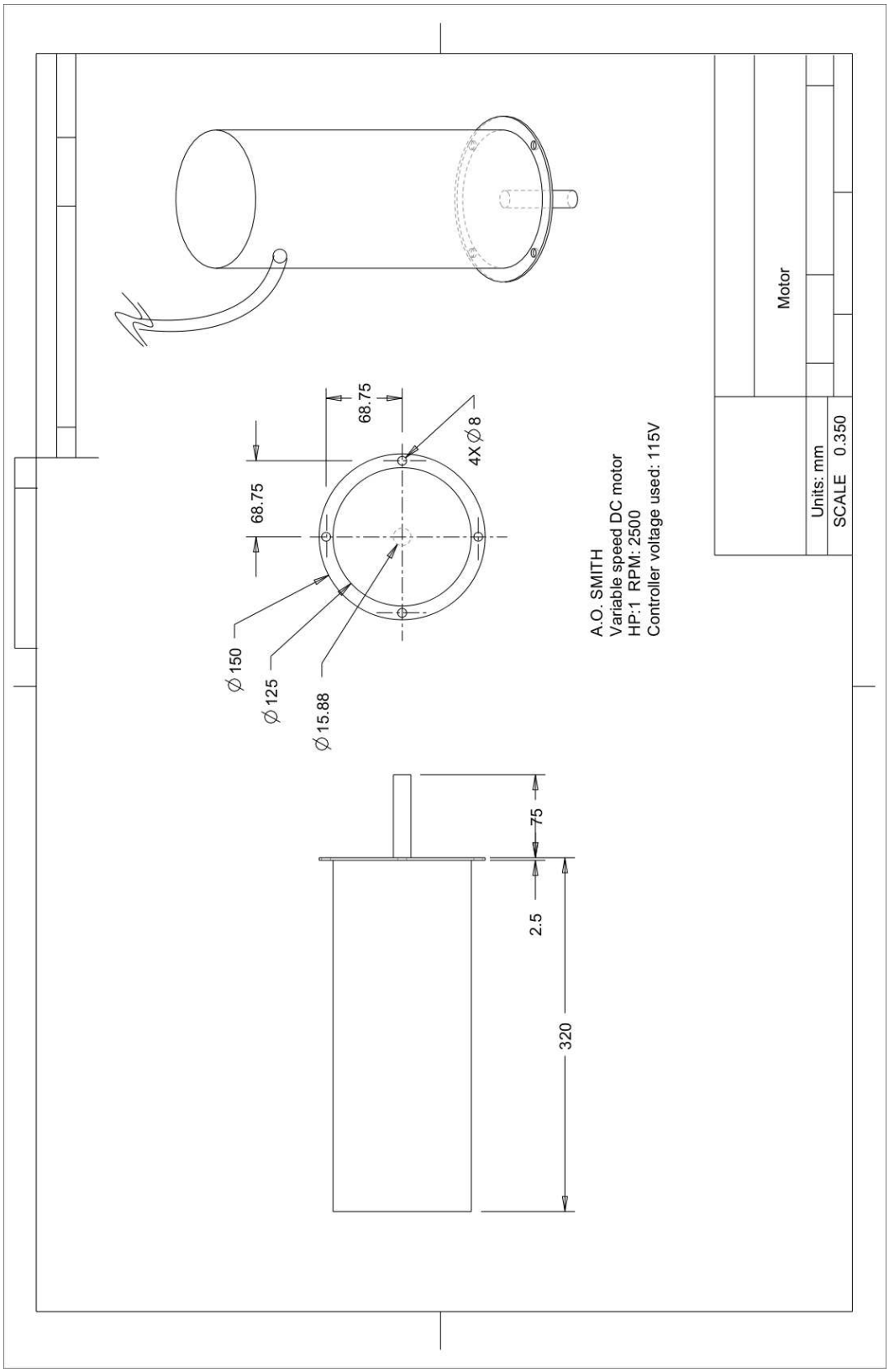
Motor
Units: mm
SCALE 0.350
A.O. SMITH
Variable speed DC motor
HP:1 RPM: 2500
Controller voltage used: 115V
68.75
68.75
4X ∅8
∅150
∅125
∅15.88
75
2.5
320

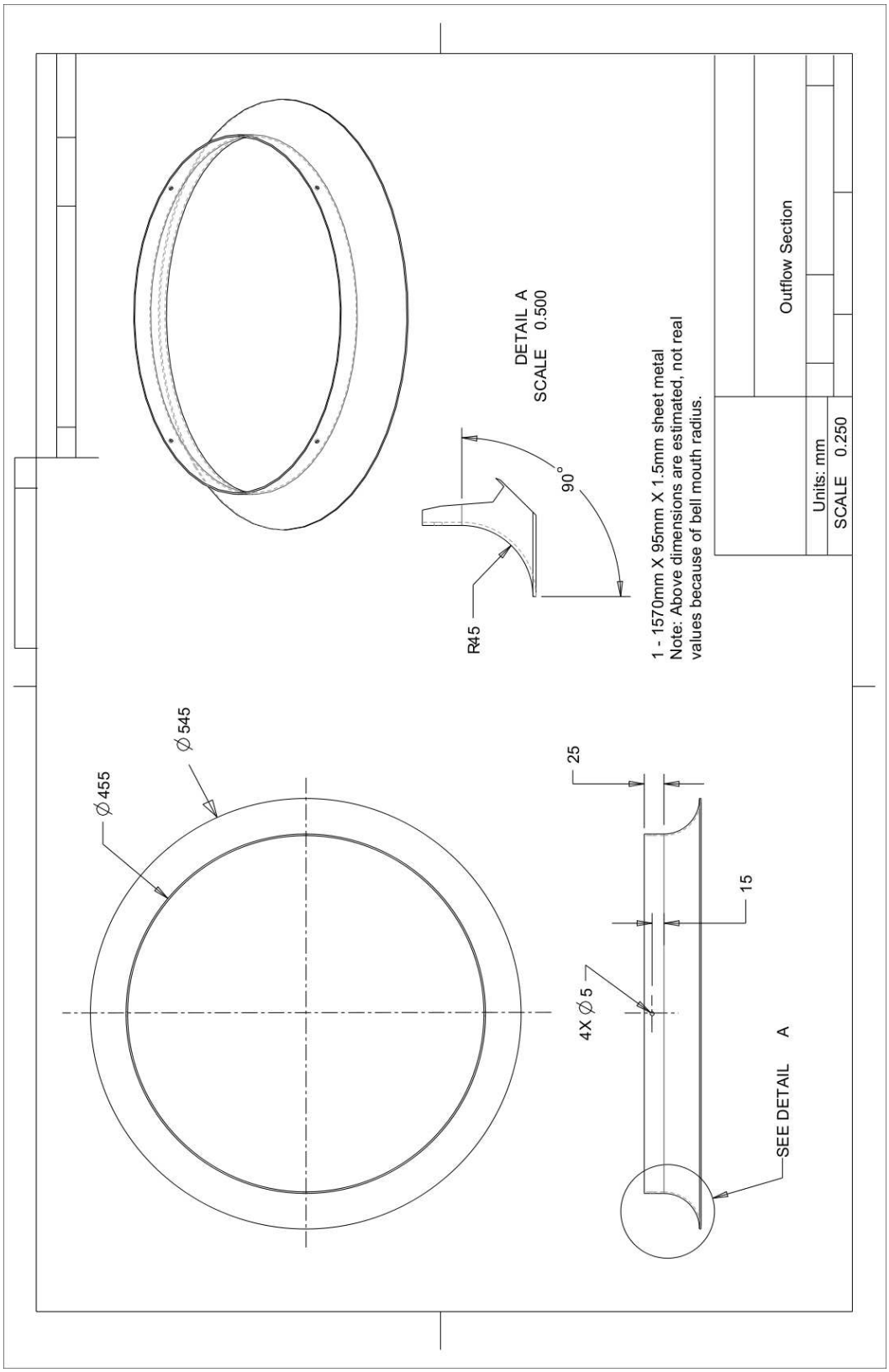
Outflow Section
Units: mm
SCALE 0.250
DETAIL A
SCALE 0.500
90°
R45
1 - 1570mm X 95mm X 1.5mm sheet metal
Note: Above dimensions are estimated, not real
values because of bell mouth radius.
Ø545
Ø455
25
15
4X Ø5
SEE DETAIL A

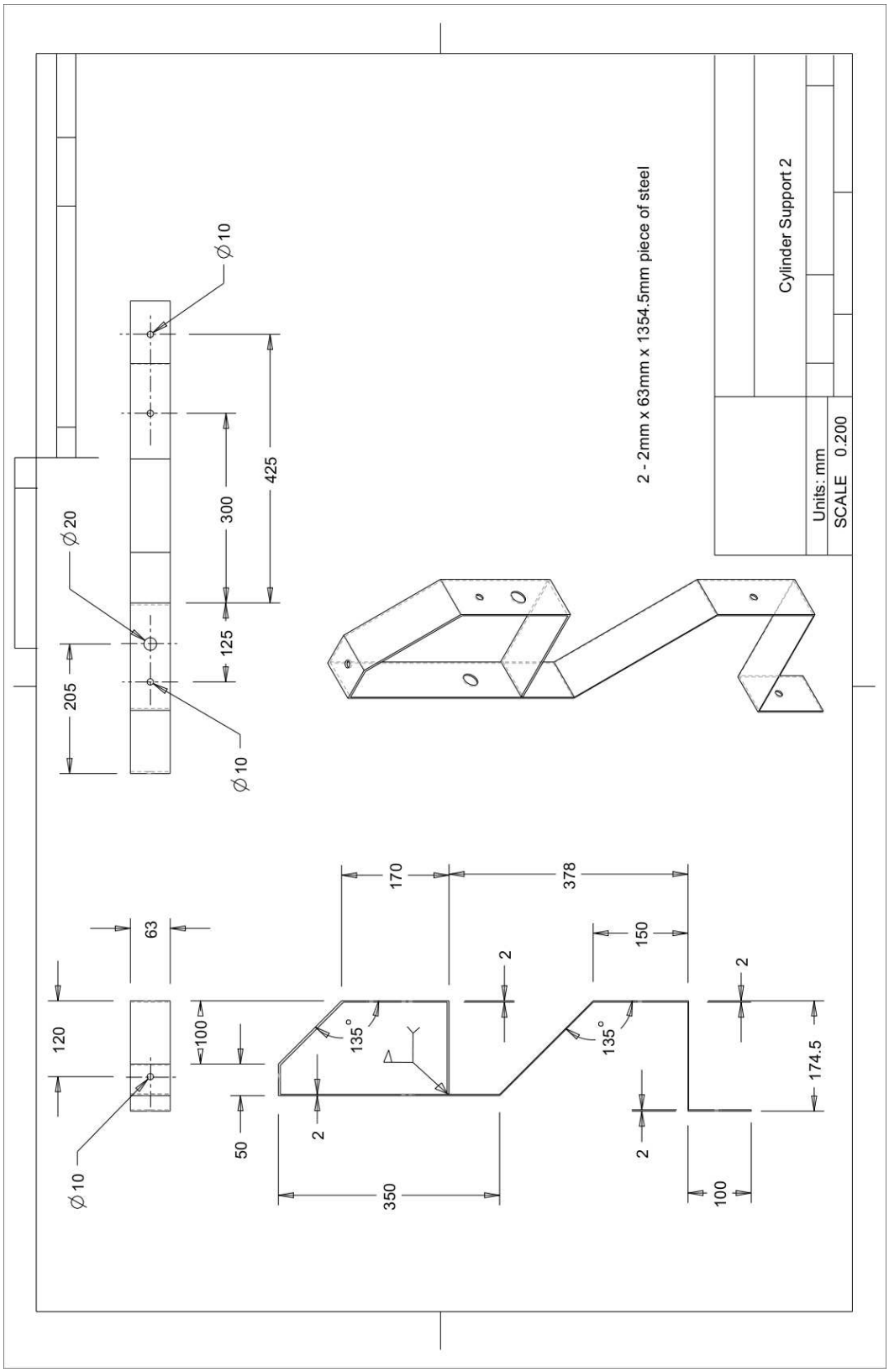
Cylinder Support 2
Units: mm
SCALE 0.200
2 - 2mm x 63mm x 1354.5mm piece of steel
Ø10
Ø20
Ø10
Ø10
425
300
125
205
63
120
100
50
170
378
150
2
2
2
2
135°
135°
174.5
350
100

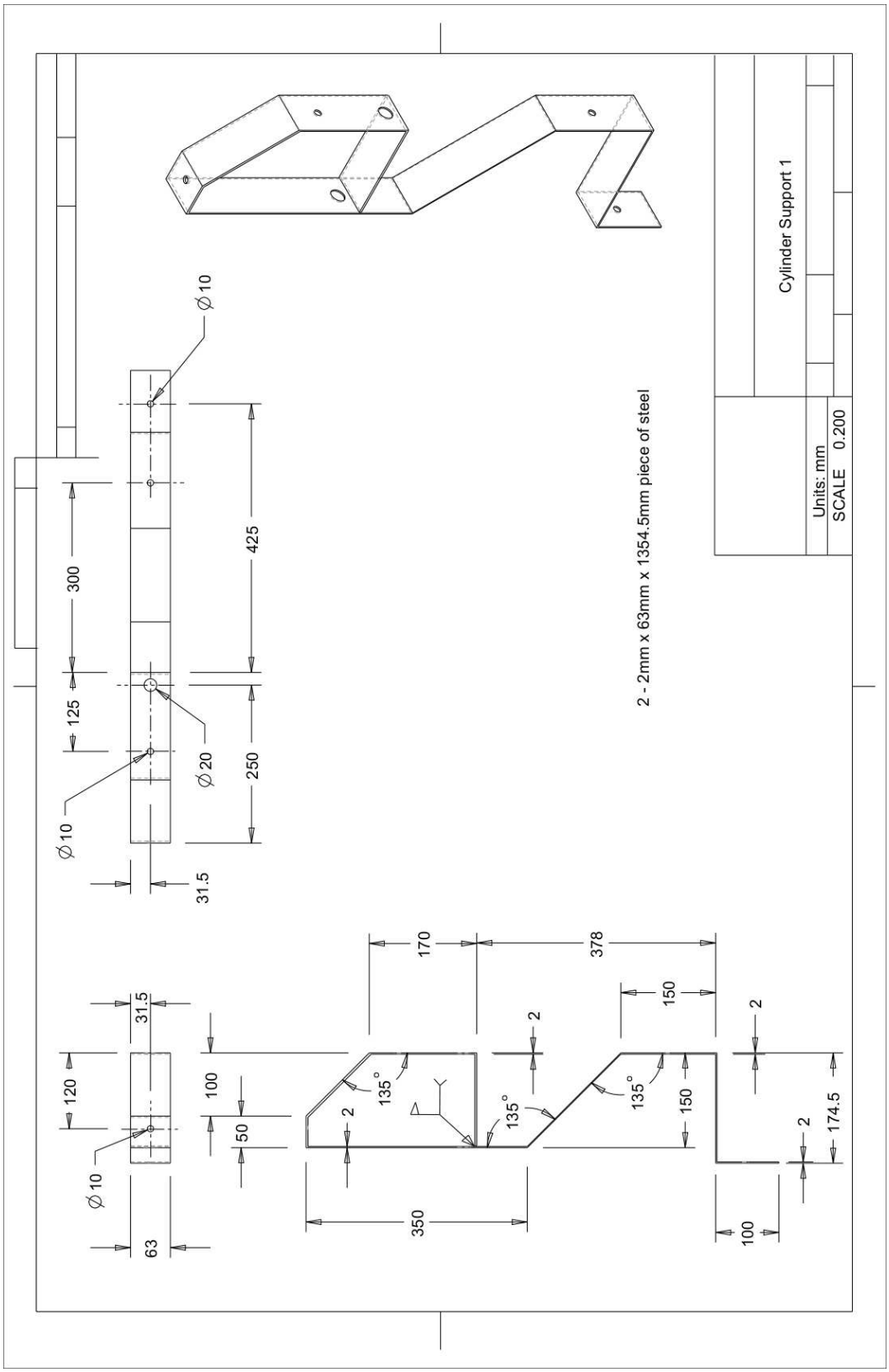
Cylinder Support 1
Units: mm
SCALE 0.200
2 - 2mm x 63mm x 1354.5mm piece of steel
Ø10
Ø20
300
125
425
250
31.5
120
63
100
50
170
378
150
135°
2
174.5
350

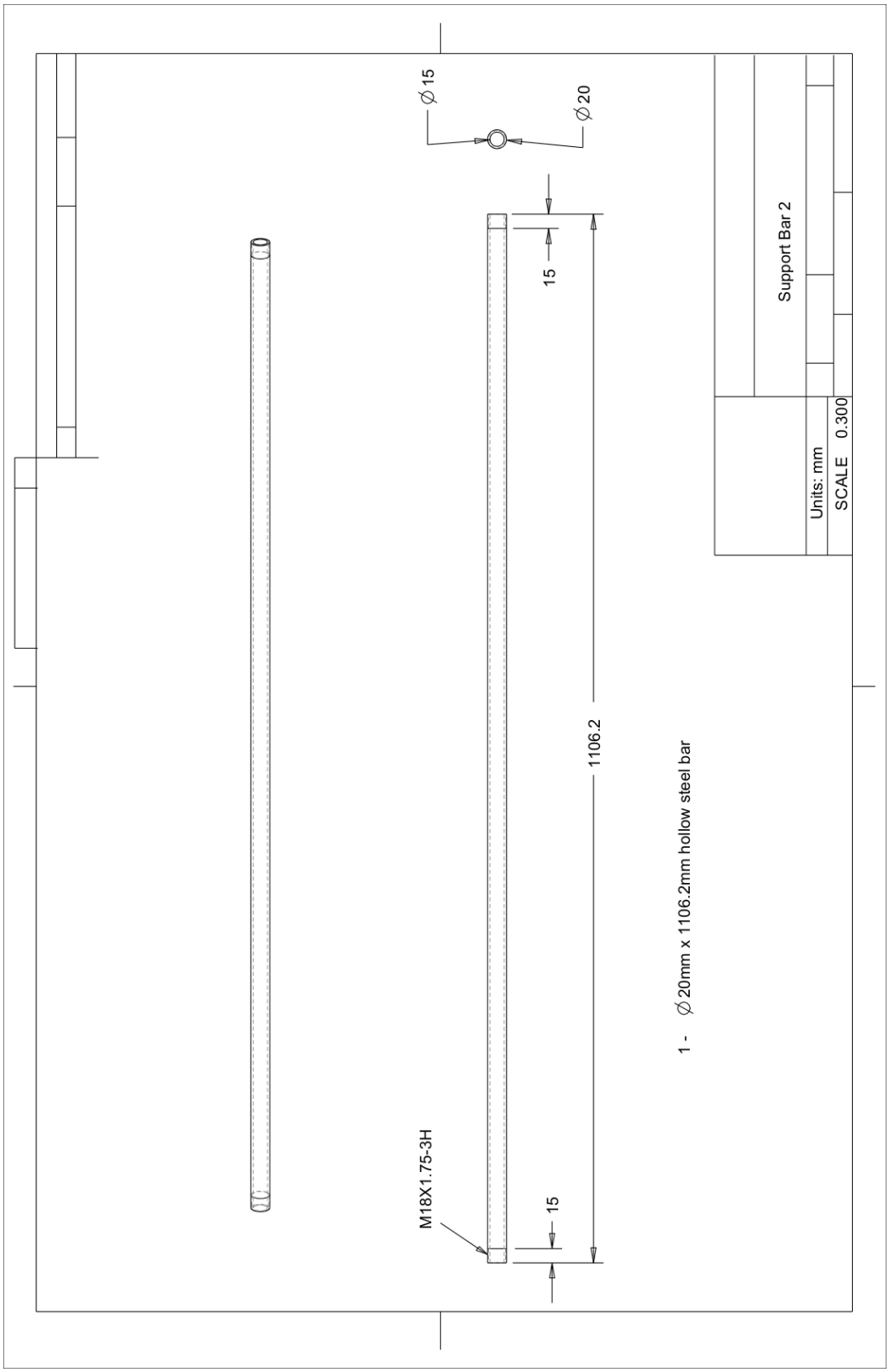
Support Bar 2
Units: mm
SCALE 0.300
∅15
∅20
15
1106.2
15
M18X1.75-3H
1 - ∅20mm x 1106.2mm hollow steel bar

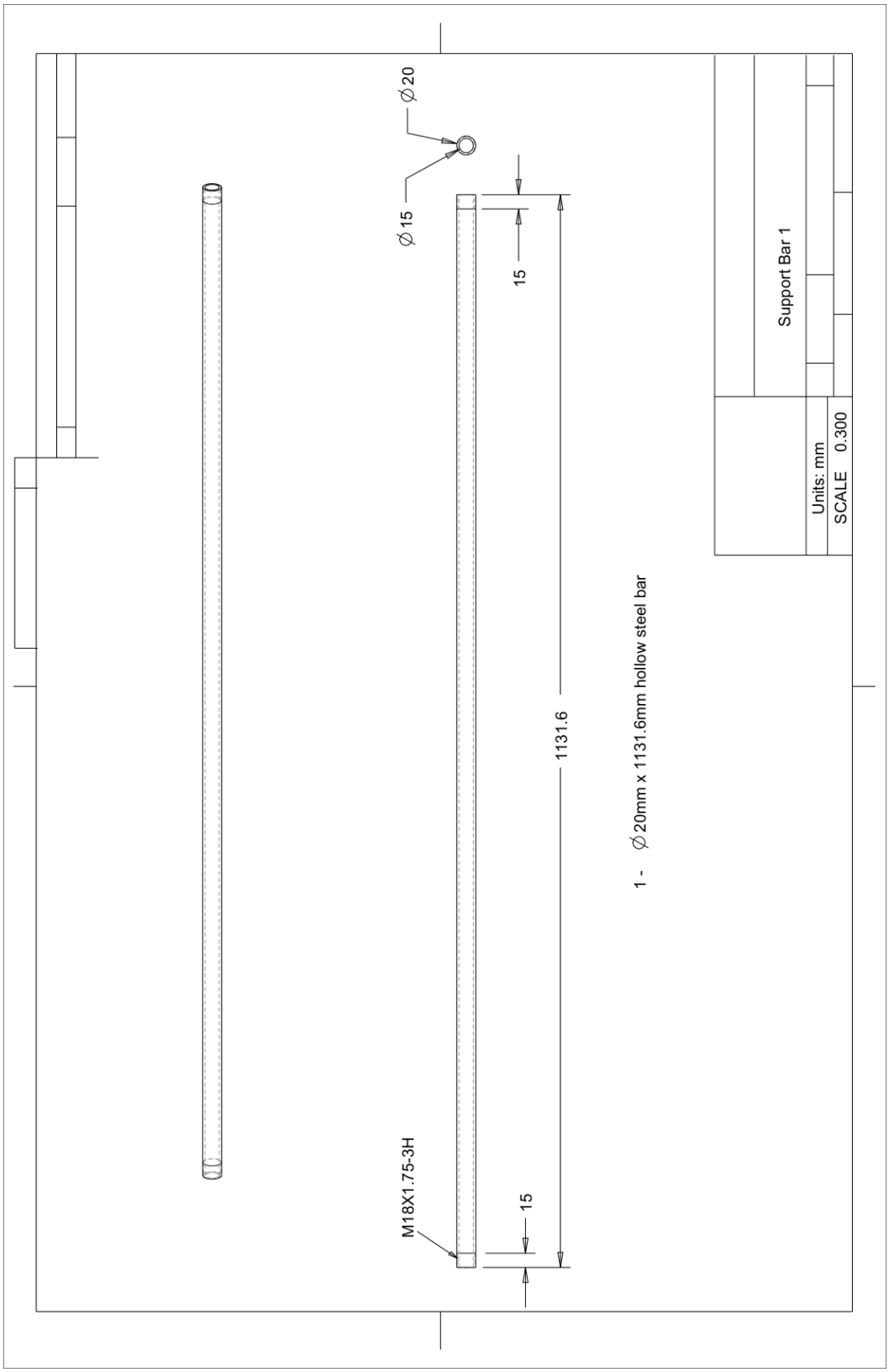
Support Bar 1
Units: mm
SCALE 0.300
∅20
∅15
15
1131.6
15
M18X1.75-3H
1 - ∅20mm x 1131.6mm hollow steel bar

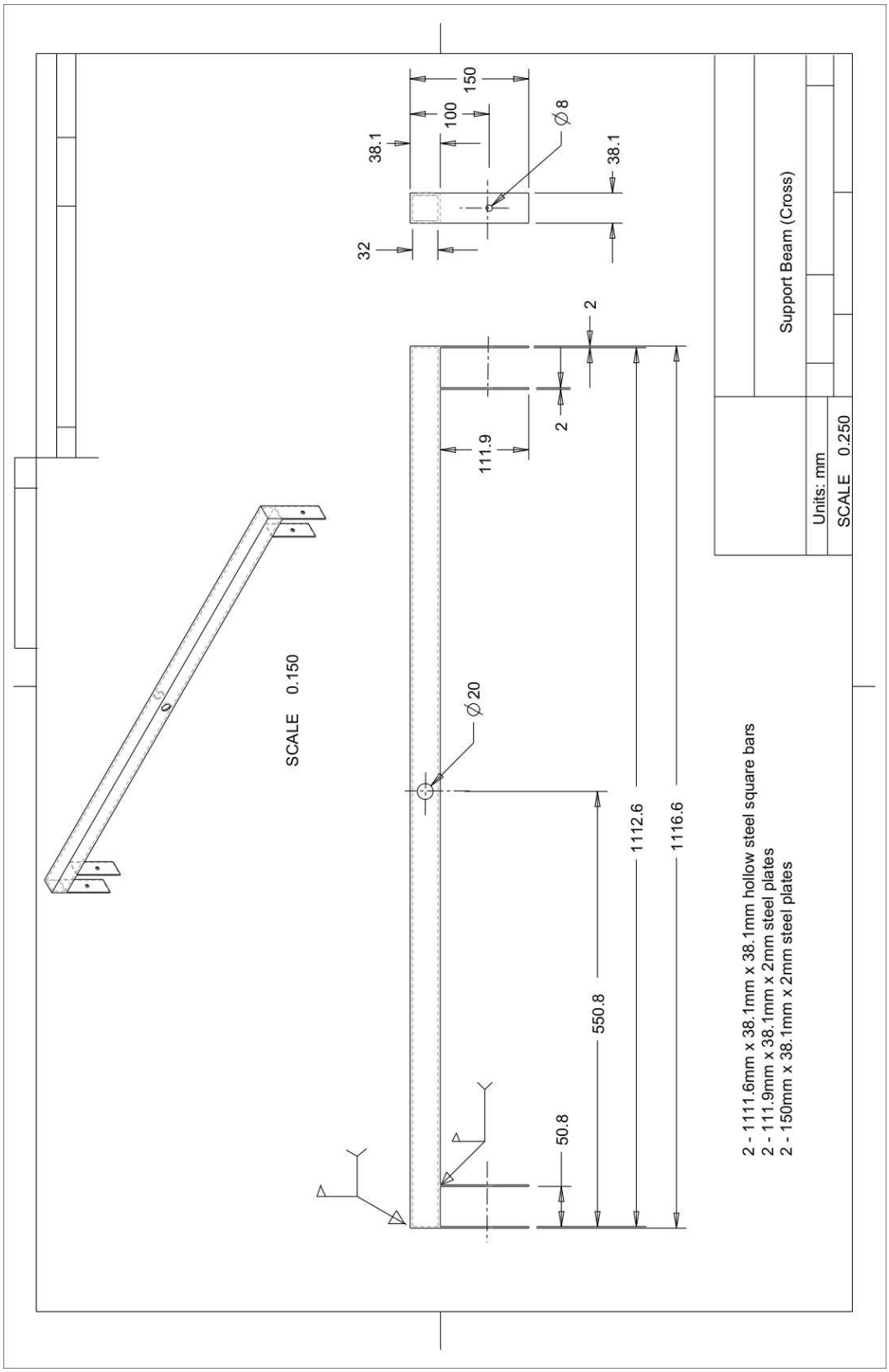
Support Beam (Cross)
Units: mm
SCALE 0.250
SCALE 0.150
2 - 1111.6mm x 38.1mm x 38.1mm hollow steel square bars
2 - 111.9mm x 38.1mm x 2mm steel plates
2 - 150mm x 38.1mm x 2mm steel plates
150
100
38.1
38.1
32
Ø8
2
2
111.9
Ø20
1112.6
1116.6
550.8
50.8

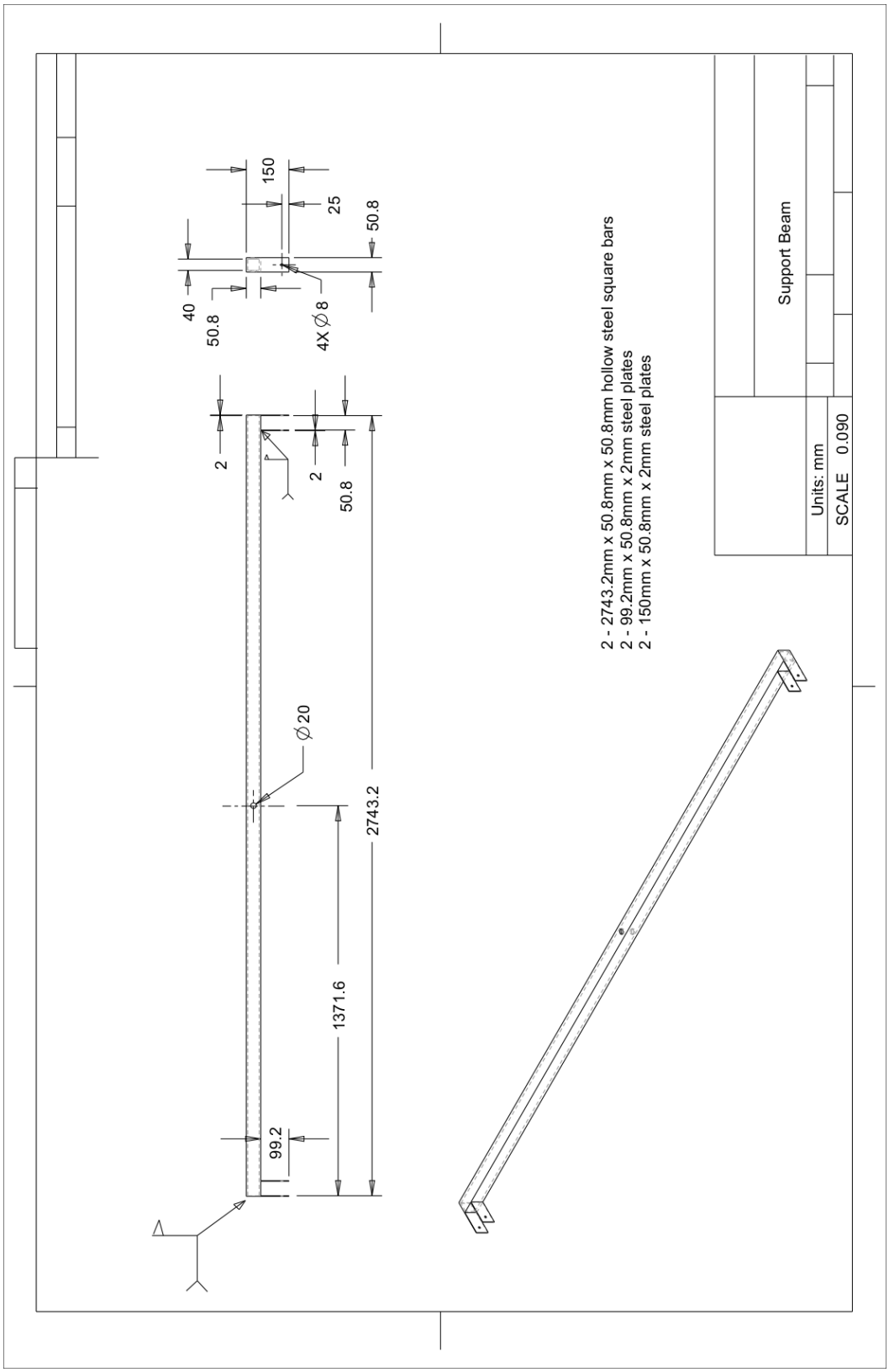
Support Beam
Units: mm
SCALE 0.090
2 - 2743.2mm x 50.8mm x 50.8mm hollow steel square bars
2 - 99.2mm x 50.8mm x 2mm steel plates
2 - 150mm x 50.8mm x 2mm steel plates
150
25
50.8
40
50.8
4X ∅ 8
2
2
50.8
∅ 20
2743.2
1371.6
99.2

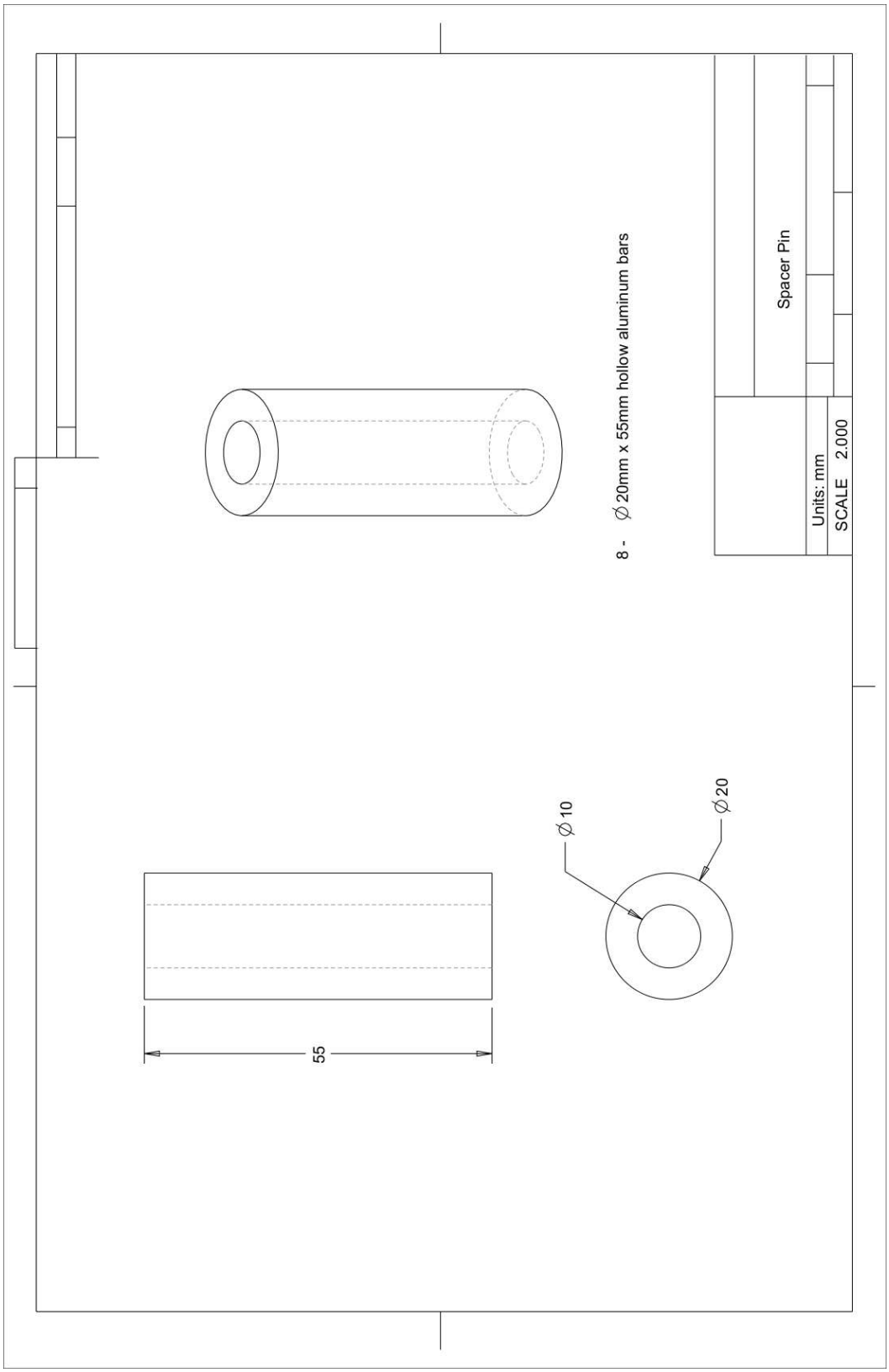
Spacer Pin
Units: mm
SCALE 2.000
8 - ∅20mm x 55mm hollow aluminum bars
∅10
∅20
55

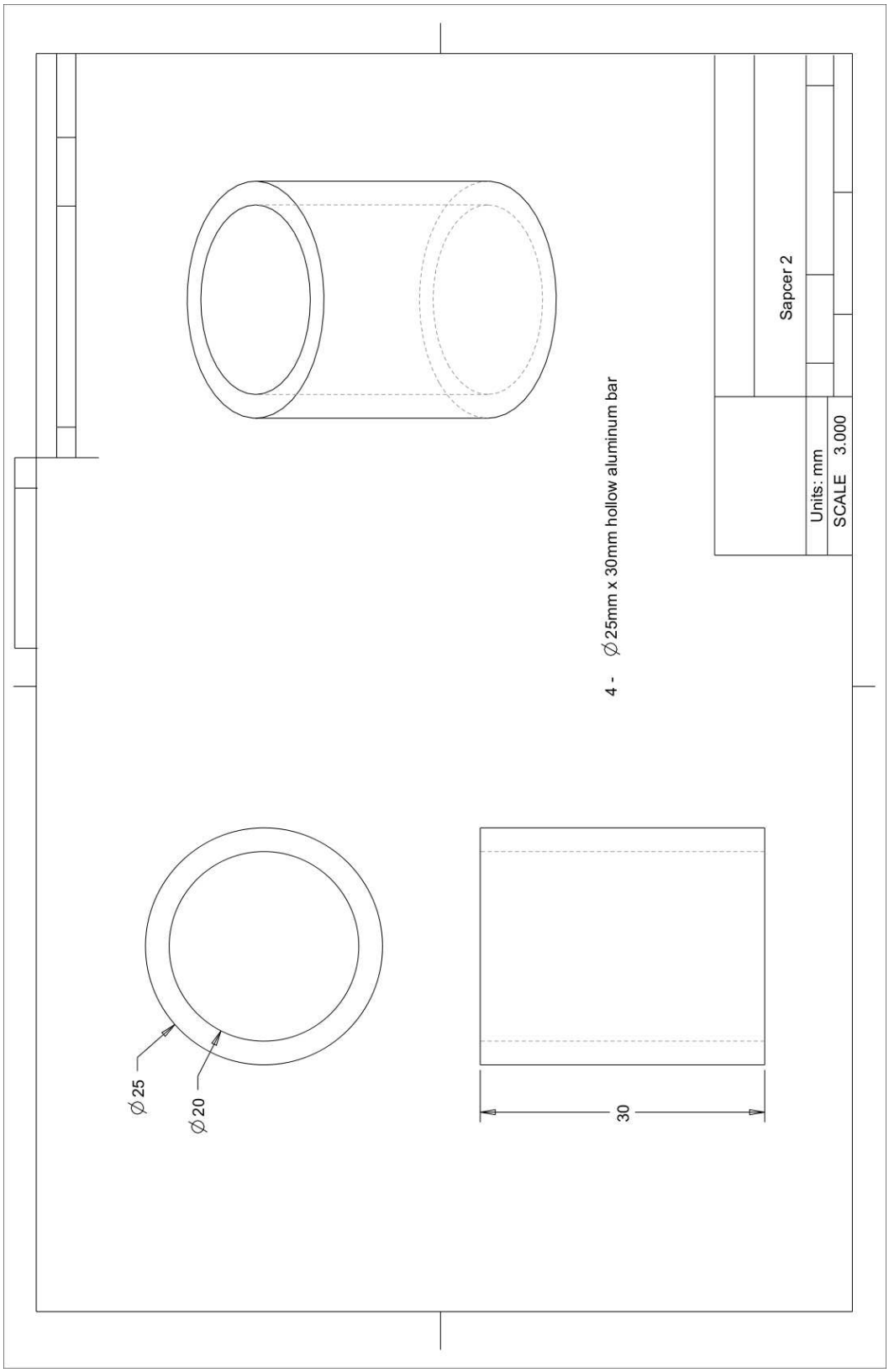
Sapcer 2
Units: mm
SCALE 3.000
4 - ∅25mm x 30mm hollow aluminum bar
∅25
∅20
30

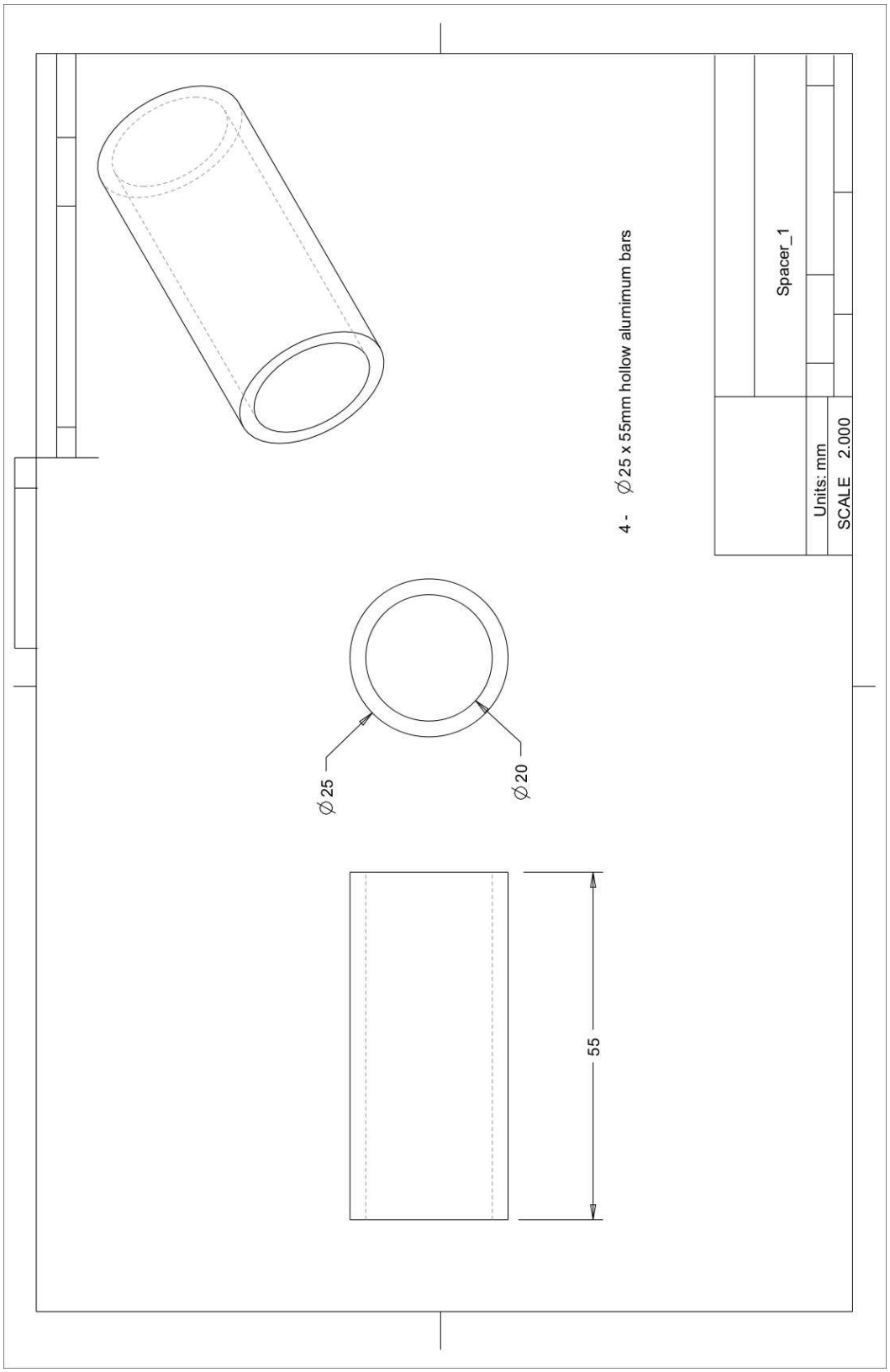
4 - ∅25 x 55mm hollow alumimum bars
Spacer_1
Units: mm
SCALE 2.000
∅25
∅20
55